

Using Seismic Methods to Constrain Mantle Convection Processes

by

Mei Xue

B.Eng (University of Petroleum – East China) 1996

M.Eng (University of Petroleum – Beijing) 1999

A dissertation submitted in partial satisfaction
of the requirements for the degree of

Doctor of Philosophy

in

Earth and Planetary Science

in the

Graduate Division
of the
University of California, Berkeley

Committee in charge:

Professor Richard M Allen, Chair
Professor Douglas S Dreger
Professor David R Brillinger

Spring 2008

The dissertation of Mei Xue is approved:

Chair _____ Date _____

_____ Date _____

_____ Date _____

University of California, Berkeley

Spring 2008

Using Seismic Methods to Constrain Mantle Convection Processes

Copyright © 2008

by

Mei Xue

Abstract

Using Seismic Methods to Constrain Mantle Convection Processes

by

Mei Xue

Doctor of Philosophy in Earth and Planetary Science

University of California, Berkeley

Professor Richard M Allen, Thesis Committee Chair

We use seismic anisotropy and traveltimes tomography to investigate mantle convection processes with a focus on upwelling at Iceland, Newberry, and Yellowstone, and subduction in Cascadia. Beneath Iceland the observed seismic anisotropy pattern as revealed by SKS splitting analysis shows the outward horizontal flow of upwelling material first toward and then down the North Atlantic Ridge. In contrast, beneath the Newberry hotspot track, SKS splits are not parallel to the track instead showing the average fast directions of ENE-WSW to the northwest and of more E-W to the east. This suggests that the age-progressive volcanism along the Newberry track is unlikely a direct product of asthenospheric flow along the track and is most likely the product of lithosphere-controlled processes. West of the Newberry track is the Juan de Fuca subduction system. We image the subducted slab in the mantle east of the Cascades beneath Oregon to a depth of 400 km but no deeper. We propose that the absence of the slab below 400 km today is due to the arrival of the Yellowstone plume head around 17 Ma which destroyed the Juan de Fuca slab at depths greater than the thickness of the continental lithosphere. A low-velocity layer also imaged beneath the slab is perhaps

remnant plume material that has been pulled down by the subduction. This tectonic model is supported by our recent high resolution velocity models for the entire western USA. The models show that the mantle structure beneath the western USA is very heterogeneous but has a strong correspondence with the complicated tectonics of the region. The observation of the Juan de Fuca subduction system confirms it stops at ~ 400 km, and is disrupted in Oregon, likely due to interaction with the Yellowstone plume head. Beneath Yellowstone, we do not detect a low velocity conduit reaching greater than 500 km depth which implies that either (1) any plume was short-lived; or (2) the conduit is beyond our resolution; or (3) there was no deep mantle plume. We prefer the short-lived plume model as it best explains many of the imaged features the Pacific Northwest.

Professor Richard M Allen

Dissertation Committee Chair

Contents

List of Figures	v
List of Tables	vi
Acknowledgements	vii
1 Introduction	1
2 Asthenospheric channeling of the Icelandic upwelling	8
2.1 Introduction	9
2.2 Data and method	12
2.3 Splitting results	14
2.4 Interpretation of shear-wave splits	16
2.4.1 Source depth of the anisotropic signal	16
2.4.2 Single layer of anisotropy	18
2.4.3 Relating flow to the fast splitting direction	19
2.4.3.1 The influence of water on the fast splitting direction	20
2.4.3.2 The influence of melt on the fast splitting direction	23
2.4.4 Comparison of splits with conceptual mantle flow geometries	25
2.5 Ridge-channeled flow	28
2.6 Conclusion	32
3 Origin of the Newberry Hotspot Track	45
3.1 Introduction	46
3.2 Tectonic models proposed	48
3.3 Shear-wave splits	49
3.4 Discussion	52
3.5 Conclusion	56
4 The Fate of the Juan de Fuca Plate	63
4.1 Introduction	64
4.2 Data and method	68
4.3 Tomographic results and resolution tests	70
4.4 Discussion	74
4.5 Conclusion	81
5 Western USA Mantle Structure and its Implications for Mantle Convection Processes	89
5.1 Introduction	91
5.2 Data and method	96
5.2.1 Station distribution	96
5.2.2 Event distribution	98
5.2.3 Method	99
5.2.4 Event correction and station correction	100

	iv
5.3 Checker-board resolution tests	102
5.4 Tomographic results and interpretation	104
5.4.1 The Juan de Fuca subduction system	105
5.4.2 The Yellowstone upwelling and the East Snake River Plain	108
5.4.3 The Newberry track/High Lava Plains	111
5.4.4 High velocities beneath eastern Washington, northeastern Oregon and northern Idaho	112
5.4.5 High velocities beneath southern Sierra Nevada and Transverse Ranges	113
5.4.6 The Coast Ranges	115
5.4.7 Low velocities above the Juan de Fuca slab	116
5.4.8 The “slab gap” south of the Mendocino Triple Junction	117
5.4.9 Velocity contrast across the San Andreas Fault	117
5.4.10 The volcanic arcs and the Central Valley	118
5.4.11 The Salton Trough	118
5.4.12 The slow Basin and Range and the high velocity anomaly in central Nevada	119
5.4.13 The Colorado Plateau and the Rocky Mountain	120
5.5 Implications for mantle convection processes: The origin on Yellowstone and the fate of the Juan de Fuca slab	121
5.6 Conclusion	124
6 Conclusions	150
Bibliography	153

List of Figures

2.1 Seismic stations used in this study	38
2.2 Distribution of the 28 events used in this study	39
2.3 Splitting results across Iceland	40
2.4 Fast splitting directions ϕ as a function of event back-azimuth for station HOT27 (a) and HOT12 (b)	41
2.5 Splitting parameters (a) ϕ and (b) δt as a function of event back-azimuth for station HOT17	42
2.6 Conceptual mantle flow geometries beneath Iceland	43
2.7 Map placing asthenospheric anisotropy observations in the context of the proposed ridge-channeled flow model	44
3.1 Tectonic map for the study region	59
3.2 Splitting results across Oregon	60
3.3 Splitting parameters (a) the fast splitting direction and (b) the splitting time as a function of event back-azimuth for station OT09	61
3.4 Oregon splits shown in regional context	62
4.1 Tectonic map for the study region	85
4.2 Vertical slices through the (a) V_s and (b) V_p models along the OATS line indicated in Fig. 4.1	86
4.3 Resolution tests for the V_s velocity model	87
4.4 Proposed tectonic model for the interaction between the subducting Juan de Fuca Plate (blue) and the Yellowstone plume head (pink)	88
5.1 Tectonic map for the study region	131
5.2 The seismic stations used in this study with a total number of 809	132
5.3 Distribution of (a) 88 events and 23233 rays used in the DNA07-S model inversion and (b) 58 events and 15141 rays used in the DNA07-P model	133
5.4 Station corrections for (a) the DNA07-S model and (b) DNA07-P model	134
5.5 Checker-board test for cell size of 250 km for the DNA07-S model	135
5.6 Checker-board test for a cell size of 250 km for the DNA07-P mode	136
5.7 Checker-board test for a cell size of 500 km for the DNA07-S model	137
5.8 Checker-board test for cell size of 500 km for the DNA07-P model	138
5.9 Depth slices through the DNA07-S model (left column) and DNA07-P model (right column) from 100 km to 800 km depth with an interval of 100 km	139
5.10 (a) Locations of the cross-sections of vertical slices shown in Fig. 5.10b and Fig. 5.11. (b) Vertical slices through the DNA07-S (left column) and DNA07-P (right column) models	141
5.11 Checker-board test for cell size of 200 km for (a) the DNA07-S and (b) -P models	144
5.12 Resolution tests on the observed slab feature for (a) the DNA07-S and (b) - P models	146
5.13 Vertical slices through the DNA07 models	147
5.14 A synthetic test for a mantle plume located beneath the Yellowstone caldera	148
5.15 Vertical slices through the Transverse Ranges anomaly	149

List of Tables

2.1 Earthquakes used in study	36
2.2 Shear-wave splitting parameters for HOTSPOT and SIL stations	37

Acknowledgements

First of all, I want to express my deepest gratitude to my advisor, Prof. Richard M Allen. Without his supervision and encouragements, I would not have been able to go this far. His knowledge, patience, kindness and support have always been great help for me in learning seismology and moving forward. I am also grateful to Prof. Douglas S Dreger. As the advisor of my second project, he is patient, kind, and supportive. Unfortunately, I stopped working on it due to time issue. I hope in the future I can work with him to make it up. I learned about seismic sources from his group meeting. I also learned and enjoyed from three classes he taught. I also want thank my other committee members, Prof. Barbara Romanowicz, Prof. Michael Manger, and Prof. David Brillinger. In my oral exam, the angel smiles on their faces really helped. I also attended Prof. Romanowicz's group meeting and gained a lot there. Prof. David Brillinger gave me helpful suggestions on finishing my dissertation as well as on my future career.

I am grateful to my friends and colleagues in BSL for creating a nice environment for me to study and work in, especially Ahyi Kim and Aimin Cao. Charley Paffenbarger and Bob Uhrhammer provided invaluable assistance in my research. I also want to thank the people in the Geology and Geophysics Department of UW-Madison, especially Andrew Lockman and his family. I studied there for 2.5 years and I really enjoyed the experience. A special thanks to my old friend Li Li at Houston for sharing many moments of our lives. Last, but certainly not least, I want to thank my parents, sisters, and brothers for their support during all these years. Finally, I am indebted to my husband Qingzhong Gao. Without his support and sacrifice, I could not have come to USA at the first place. Their endless love and support helped me through some difficult times while I studied in USA.

Chapter 1

Introduction

Subduction and upwelling are the two primary mantle convection processes and may play important roles in global tectonics. Some of the fundamental questions still to be explored are whether there are deep mantle plumes [DePaolo and Manga, 2003; Foulger and Natland, 2003] and how deep can subducted plates penetrate? Here we investigate mantle convection processes with focuses on mantle upwelling and subduction at regions of diverse tectonic environments: The Icelandic Upwelling, the Newberry hotspot track, the Juan de Fuca subduction zone and the Yellowstone Upwelling. Fundamental questions regarding these regions are: (1) how does the Icelandic Upwelling material disperse when it arrives the base of the lithosphere? (2) what is the causal mechanism of the Newberry hotspot track? (3) how far does the Juan de Fuca slab extend down into the mantle and (4) does the slab break up and disintegrate due to its young age or the passage of the proposed Yellowstone Plume? Progress in answering these questions is currently hampered by: 1) the limited data, 2) the limitation of using a single analysis technique and 3) the difficulty in comparing results from different studies. This dissertation aims to resolve these at least some of these problems by applying integrated seismological techniques on combined dataset from different seismic networks and integrating our results with other geophysical, geochemical and geologic studies. Specifically, we use shear-wave splitting and travelttime tomography to explore the seismic structure beneath

these regions and understand the mantle convection/geological processes responsible for tectonics today.

Located on the North Atlantic Ridge, Iceland is an ideal place to study the interactions between hotspot upwelling and mid-ocean ridge processes. The existence and spatial influence of the Icelandic upwelling has been confirmed by seismic tomography studies and surface observations, e.g. the broad high topography and the thick crust of Iceland [Bell and Buck, 1992; Wolfe, et al., 1997; Searle, et al., 1998; Allen, et al., 1999; Darbyshire, et al., 2000; Foulger, et al., 2001; Allen, et al., 2002a; Allen, et al., 2002b]. Geochemical signatures show that both the Reykjanes Ridge to the north and the Kolbeinsey Ridge to the south are affected by the Iceland upwelling [Schilling, 1973; Poreda, et al., 1986; Schilling, et al., 1999]. Estimates of upwelling flux and crustal generation rates imply that the bulk of upwelling material flows away from the region without participating in melting processes beneath Iceland [Allen, et al., 2002a]. A key question is how does this upwelling material interact with the North Atlantic Ridge and disperse in the North Atlantic asthenosphere? Two geometries have been suggested: radial flow and ridge-channeled flow. In radial flow, material spreads out in all directions away from the upwelling axis [Ito, et al., 1996; White and Lovell, 1997; Ito, 2001], whereas in channeled flow, upwelling material feeds asthenospheric channels below the spreading axis [Vogt, 1976; Schilling, 1985; White, et al., 1995; Yale and Morgan, 1998; Albers and Christensen, 2001]. Both of these two geometries can generate the observed V-shaped pattern of bathymetry.

On the other side of the North American plate, the Newberry Hotspot Track is located on the west margin of the North American plate showing a monotonic age progression from east to west ending at the Newberry Caldera [Jordan, *et al.*, 2004]. While the Newberry Hotspot Track is associated with bimodal age-progressive volcanism, high topography and high heat flow [Christiansen and McKee, 1978; Humphreys and Dueker, 1994a; Jordan, *et al.*, 2004], it cannot be the direct product of a stationary deep mantle plume or any other stationary source, as the hotspot path is northwesterly at $\sim 120^\circ$ to plate motion. Four end-member tectonic models have been proposed for the formation of the Newberry Hotspot Track: (1) subduction counterflow, where counterflow associated with the subduction of the Juan de Fuca plate beneath North America draws material westward across the base of the continental lithosphere [Draper, 1991; Humphreys, *et al.*, 2000; Jordan, *et al.*, 2004; Jordan, 2005]; (2) gravitational flow along lithospheric topography [Humphreys, *et al.*, 2000; Jordan, *et al.*, 2004; Jordan, 2005]; (3) lithospheric faulting, i.e. progressive faulting in the lithosphere, initiating near the McDermitt caldera [Smith, 1977; Pierce, *et al.*, 2000; Rocchi, *et al.*, 2003]; (4) the extension of the Basin and Range [Christiansen and McKee, 1978; Christiansen, *et al.*, 2002].

West of the Newberry track in the Pacific Northwest, the Juan de Fuca plate is currently subducting beneath the northwestern United States and southwestern Canada. A considerable amount of geophysical data illuminates the subducting Juan de Fuca plate west of the Cascades (e.g., [Trehu, *et al.*, 1995; Flueh, *et al.*, 1998; Bostock, *et al.*, 2002]). However, previous tomographic studies suggest that the slab is not ubiquitous at greater

depths east of the Cascades. Although the slab has been imaged to depths of ~300 to 400 km beneath Washington, there is little evidence for the presence of a slab in the mantle east of the Cascades beneath Oregon [*Michaelson and Weaver, 1986; Rasmussen and Humphreys, 1988; Harris, et al., 1991; Bostock, et al., 2002*]. The apparent absence of the slab east of the Cascades has been interpreted as suggesting that (1) the slab has a small velocity contrast making the slab indistinct from the surrounding mantle [*Michaelson and Weaver, 1986*], (2) the slab has a vertical geometry [*Rasmussen and Humphreys, 1988*] or has broken off with a steep dip [*Michaelson and Weaver, 1986; Rasmussen and Humphreys, 1988*], or (3) a loss of seismic resolution prevents imaging of the slab [*Rasmussen and Humphreys, 1988*].

Western USA is on the west margin of the North American plate and is a region that has complicated and active tectonics. The Juan de Fuca plate, the Pacific plate, and the North American plate meet in this region and form the Mendocino triple junction just offshore northern California. In addition to these primary tectonic objects, the most prominent features are the voluminous volcanism that initiated around 16Ma to 17Ma: the Yellowstone Hotspot Track, the Columbia River Basalts, and the Newberry Hotspot Track. Other prominent geologic provinces in western USA are the Coast Ranges, the Cascades, the Sierra Nevada, the Central Valley, the Transverse Ranges, the Salton Trough, the Basin and Range, the Colorado Plateau, and the Rocky Mountain front [*Harden, 1998*]. The main tectonic debate in this region whether there is a deep mantle plume. It has been proposed that a mantle plume impacted the North American lithosphere around 17 Ma, yet evidence for an upwelling conduit in the lower mantle

beneath Yellowstone today remains unclear (e.g., [Humphreys, *et al.*, 2000; Jordan, *et al.*, 2004; Yuan and Dueker, 2005; Waite, *et al.*, 2006]). Given the proximity of the slab and the proposed Yellowstone Plume, this is an ideal place to study the interaction between subduction and upwelling processes (e.g., [Geist and Richards, 1993; Pierce, *et al.*, 2000]). The complicated tectonics results in an extremely heterogeneous mantle structure and a complete high resolution image of western USA was not achievable until the deployment of the Transportable Array.

In chapter 2, we study the dispersion pattern of the Icelandic upwelling material using seismic anisotropy which provides information about mantle strain and therefore have the potential to elucidate mantle flow geometries in the region. We present new SKS and SKKS splitting data from the HOTSPOT and SIL networks following the method of Silver and Chan (1988; 1991). Our observed anisotropy pattern beneath Iceland reveals the horizontal flow of upwelling material toward and then down the North Atlantic Ridge. Material initially flows from the axis of upwelling beneath southeast Iceland to the northwest in what might be considered as ridge perpendicular flow from an off-ridge hotspot toward the ridge. Material then flows to the north and southwest down the Kolbeinsey and Reykjanes ridges respectively. These observations are consistent with the observed generation of V-shaped ridges along the Reykjanes and Kolbeinsey ridges due to channeling of upwelling material down the ridges.

In chapter 3, we investigate the causal mechanism of the Newberry hotspot track using shear-wave splitting method. If the Newberry track is a product of asthenospheric

processes such as subduction counterflow or gravitational flow as has been proposed, then asthenospheric flow is expected along the length of the hotspot track. Alternatively, if lithospheric processes such as faulting and/or Basin and Range extension are responsible for the hotspot track, asthenospheric flow along the hotspot is not required. We use data collected from the Oregon Array for Teleseismic Study (OATS) that was deployed along the Newberry track in May 2003 and operated until May 2006 to measure the SKS splitting [*Silver and Chan, 1988; Silver and Chan, 1991*]. The observed fast directions are not parallel to the Newberry track, meaning that it is unlikely that asthenospheric flow is responsible for the age-progression volcanism. Instead, we suggest the Newberry track is the product of a lithosphere-controlled process.

In chapter 4, we use a teleseismic body wave traveltimes tomographic method to image the subducted Juan de Fuca plate beneath Oregon. We use a dataset collected from the Oregon Array for Teleseismic Study (OATS) complemented by data from other available permanent networks and temporary deployments. We developed a new seismic velocity model JdF07 for the Juan de Fuca plate. JdF07 clearly shows that the Juan de Fuca plate dives into the mantle beneath Oregon and continues east of the High Cascades with a dip of $\sim 50^\circ$ reaching a depth of ~ 400 km but no deeper. In addition there is a low-velocity zone beneath the slab in our S-wave velocity model. We propose that the absence of the slab below 400 km today is due to the arrival of the Yellowstone plume head around 17 Ma, which destroyed the Juan de Fuca slab in the upper mantle. The low velocity anomaly beneath the slab is likely the remnant plume head material.

In chapter 5, we use the teleseismic body-wave traveltime tomographic method to study the 3D velocity structure of the entire western USA to understand the mantle convection processes in this region. We use a dataset collected from the Transportable Array, and complemented by data from 26 other available networks in the study region. This results in an unprecedented dense distribution of stations in the western USA allowing us not only to fill the gaps in the resolution of previous studies but also to see deeper into the mantle revealing new features. While previous velocity models derived from body wave traveltime tomographic studies are mostly P-wave velocity models, we developed both P- and S-wave velocity models for the western USA. We refer to our seismic velocity models as DNA07-P for the P-velocity model and DNA07-S for the S-velocity model, where DNA07 is the acronym for the Dynamic North America model of 2007. The high resolution DNA07 models of the western USA reveal an extremely heterogeneous mantle structure and provide important information about mantle convection processes in this tectonically active region and their possible interactions with different geological objects, e.g., the subduction of the Juan de Fuca plate and the upwelling of the Yellowstone plume.

Chapter 2

Asthenospheric Channeling of the Icelandic Upwelling

This chapter has been published in *Earth and Planetary Science Letters* with the title of “Asthenospheric channeling of the Icelandic upwelling: Evidence from seismic anisotropy” [Xue and Allen, 2005].

Summary

Two end-member geometries, radial flow and ridge-channeled flow, have been proposed for the dispersion of material upwelling beneath Iceland. Seismic anisotropy provides information on mantle flow, and therefore has the potential to discriminate these two geometries. In this study, we combine the HOTSPOT and SIL datasets (39 stations) and select 28 events for teleseismic shear-wave splitting analysis. Splitting results in central and eastern Iceland show 1-2 sec splitting times with an average NNW-SSE orientation of the fast splitting direction and an anti-clockwise rotation of fast axes from east to central Iceland. In western Iceland, smaller splits with a more N-S orientations are observed. Since crustal splitting times in Iceland are 0.1 sec to 0.3 sec, our delays of up to 2 sec indicate a mantle source. Both the lack of dependence of the splitting parameters on event back azimuth and the observations of null splits for events where the back azimuth is parallel or perpendicular to the fast splitting directions (observed using other events) suggest that one layer of anisotropy dominates beneath Iceland. While both high stress

plus enriched water content and melt-rich layers can result in a 90° rotation of the fast splitting direction with respect to the flow direction, we interpret our fast axis orientation as pointing in the direction of flow as the magnitude of stress is low and the amount and geographical extent of melt is likely small beneath Iceland. The observed anisotropy pattern beneath Iceland is inconsistent with radial flow away from the upwelling. Instead we propose a ridge-channeled flow model in which there is horizontal flow of material away from the upwelling axis beneath southeast Iceland toward the southern end of the Kolbeinsey Ridge and the northern end of the Reykjanes Ridge, both of which are west of the upwelling. This geometry is similar to the ridge perpendicular flow predicted for off-ridge hotspots towards the ridge. We hypothesize that upwelled material then feeds ridge parallel asthenospheric channels beneath the North Atlantic Ridge. Our interpretation is thus consistent with generation of V-shaped ridges by channeling of upwelling material down the Reykjanes and Kolbeinsey ridges.

2.1 Introduction

Iceland is a hotspot located on the North Atlantic Ridge, with the Reykjanes Ridge to the south and the Kolbeinsey Ridge to the north. This special location makes Iceland an ideal place to study the interactions between hotspot upwelling and mid-ocean ridge processes. Seismic studies show the presence of a low velocity anomaly extending vertically through the upper mantle, which has been interpreted as a high temperature buoyant upwelling centered beneath southeast Iceland [Wolfe, *et al.*, 1997; Allen, *et al.*, 1999; Foulger, *et al.*, 2001; Allen, *et al.*, 2002a]. Surface observations such as the broad

high topography of the Reykjanes Ridge, which is much smoother and lacks the segmentation of typical slow-spreading ridges [*Bell and Buck, 1992; Searle, et al., 1998*], and the thicker crust of Iceland up to six times that of normal oceanic crust [*Darbyshire, et al., 2000; Allen, et al., 2002b*] also suggest that the uppermost mantle is relatively high temperature producing large volumes of melt. This influence of the Iceland upwelling extends down the Kolbeinsey and Reykjanes ridges to the north and south of Iceland. A V-shaped pattern of bathymetry and gravity anomalies, interpreted as representing the passage of melting anomalies along the ridge away from Iceland, is observed along both the Reykjanes Ridge [*Talwani, et al., 1971; Vogt, 1971*] and on the eastern side of the Kolbeinsey Ridge (the lack of symmetry of the western side is probably due to the fact that the V-shaped ridge gravity signal has been attenuated by the gravity signal caused by up to 4 km of overlying sediments shed from Greenland [*Jones, et al., 2002*]). Geochemical signatures show that both the Reykjanes Ridge and the Kolbeinsey Ridge are affected by the Iceland upwelling [*Schilling, 1973; Poreda, et al., 1986; Schilling, et al., 1999*]. The Kolbeinsey Ridge is less affected than the Reykjanes Ridge, and might be modified by upwelling beneath Jan Mayen in addition to Iceland [*Poreda, et al., 1986; Taylor, et al., 1997; Schilling, et al., 1999*]. All these observations are generally taken as indicators of the existence and spatial influence of the Icelandic upwelling. While they are consistent with a whole-mantle plume, global tomography studies do not support the continuation of the upper mantle low velocity anomaly down into the lower mantle [*Megnin and Romanowicz, 2000; Ritsema and Allen, 2003; Montelli, et al., 2004*]. We therefore use the term “upwelling” instead of “plume”.

Various models have been proposed for the interaction between the Icelandic upwelling and the North Atlantic Ridge based on the above observations, via either along-axis melt transport [Vogt, 1976; Braun and Sohn, 2003] or large-scale asthenospheric flow [Schilling, 1985; White, et al., 1995; Yale and Morgan, 1998; Ito, et al., 1999; Albers and Christensen, 2001; Ito, 2001]. Estimates of upwelling flux and crustal generation rates imply that the bulk of upwelling material flows away from the region without participating in melting processes beneath Iceland [Allen, et al., 2002a]. A key question is how does this upwelling material disperse in the North Atlantic asthenosphere? This remains enigmatic not only to Iceland, but to other plume-ridge systems [Ito, et al., 2003]. Two geometries have been suggested: radial flow and ridge-channeled flow. Vogt [1971] first discussed both radial and channeled flow and subsequent studies have generally supported one of these two end-member models. In radial flow, material spreads out in all directions away from the upwelling axis [Ito, et al., 1996; White and Lovell, 1997; Ito, 2001], whereas in channeled flow, upwelling material feeds asthenospheric channels below the spreading axis [Vogt, 1976; Schilling, 1985; White, et al., 1995; Yale and Morgan, 1998; Albers and Christensen, 2001].

New constraints are needed to test and distinguish between these two geometries. Seismic anisotropy provides information about mantle strain; constraints on anisotropic structure beneath Iceland therefore have the potential to elucidate mantle flow geometries in the region. In previous anisotropy studies [Bjarnason, et al., 2002; Li and Detrick, 2003], the splitting observations in Iceland fall into two groups: in eastern Iceland the average splitting direction is NNW-SSE, and in western Iceland the average splitting

direction is rotated clockwise to N-S [Li and Detrick, 2003] or NNE-SSW [Bjarnason, *et al.*, 2002]. Bjarnason *et al.* [Bjarnason, *et al.*, 2002] interpret their teleseismic shear-wave splitting results as the consequence of shear between the North American or Eurasian plate and background mantle flow, concluding that mantle flow is in a northward direction. Li and Detrick [Li and Detrick, 2003] also interpret their shear-wave splits as being the result of background mantle flow. In addition, they constrain anisotropy using Rayleigh waves and conclude there are two layers of anisotropy above 100 km in western and central Iceland, and SKS splitting is primarily caused by flow deeper than 100 km. This interpretation reconciles the departure of their surface wave results from splitting results and also implies that the Iceland upwelling and its interaction with the Mid-Atlantic Ridge are not sensed by or does not dominate shear-wave splitting.

In this study, we present new SKS and SKKS splitting data from the HOTSPOT and SIL networks. We use these measurements to constrain the flow of Icelandic upwelling material. The increased number of stations used provides the most detailed map of splitting observations across Iceland thus far. After constraining the depth of the anisotropy, and considering the effect of water plus stress and melt on the relationship between anisotropy and flow, we conclude that upwelling material flows from the upwelling axis northwestward towards the southern end of the Kolbeinsey Ridge. The splitting observations are inconsistent with radial flow of material away from the upwelling and we hypothesize that upwelling material instead feeds asthenospheric channels between the Kolbeinsey and Reykjanes Ridges.

2.2 Data and method

In our study, we used a total of 39 seismic stations from the HOTSPOT and SIL networks (Fig. 2.1). The HOTSPOT network was a temporary PASSCAL deployment of broadband instruments from July 1996 until July 1998 [Allen, *et al.*, 1999]. We also included 11 broadband stations from the Southern Iceland Lowlands project (SIL network) [Stefansson, *et al.*, 1993], which provided high quality data during the same period. Among 658 teleseismic events with magnitude equal to or greater than 5.5 and epicentral distances equal to or greater than 85° , 28 events provided useful data (Fig. 2.2, Table 2.1). For data to be useful the SKS or SKKS core phases must be well separated from other phases such as S and ScS and have a high signal-to-noise ratio on the transverse seismogram. Generally, events with magnitude in the range of 6.3 to 6.8 and epicenter distance around 100° provide a relatively large number of useful events. The back azimuths of the 28 useful events fall into three groups: 9° - 45° , 220° - 255° , and 327° - 347° , as shown in Fig. 2.2. In total, 258 shear-wave splitting measurements were made in this study.

We followed the method of Silver and Chan (1998; 1991) to calculate the shear-wave splitting parameters ϕ (the splitting direction) and δt (the delay time) for individual earthquakes and then followed a multi-event stacking procedure [Wolfe and Silver, 1998] to stack the error surfaces of individual earthquake and reduce the uncertainty in estimated ϕ and δt at each station. We low-pass filtered all teleseismic phases at 10 sec to reduce microseismic noise before making splitting measurements.

We observed many null results (by which we mean zero or little energy on the transverse component) in western Iceland. A null observation suggests there is either isotropic structure beneath the station or there is anisotropy but the fast axis is near-parallel or -perpendicular to the initial polarization direction (the radial direction for SKS). Calculation of the energy on the corrected transverse component for the usual range of ϕ and δt results in a broad minimum and elongated double contours in δt direction within 10° - 15° of a direction parallel or perpendicular to the back azimuth [Savage, 1999]. Correspondingly, including null splits in stacking can constrain fast splitting directions while leaving the splitting delay unconstrained. We can therefore include null observations in our stacking procedure using multiple events recorded.

2.3 Splitting results

The splitting parameters for the HOTSPOT and SIL networks derived by the stacking procedure of Wolfe and Silver (1998) are given in Table 2.2. The splitting results fall into two groups as shown in Fig. 2.3: (1) in western Iceland the average fast splitting direction is $N21^\circ E$ with an average delay time 0.6 sec; (2) in central and eastern Iceland: the average fast splitting direction is $N27^\circ W$ with an average delay time 1.4 sec. Two subgroups are also observed in central and eastern Iceland with the Mid-Atlantic Ridge as the dividing line: the average fast splitting direction is $N38^\circ W$ with an average delay time 1.5 sec in central Iceland and the average fast splitting direction is $N17^\circ W$ with an average delay time 1.2 sec in eastern Iceland. Generally, the splitting results for central

and eastern Iceland are very well constrained, whereas the splitting results for western Iceland show weak to negligible anisotropy with less well-constrained splitting directions.

Comparison of our splitting observations with regional anisotropic models shows broad consistency. Pilidou et al. (2005) use Rayleigh waves to constrain anisotropy in the upper few hundred kilometers of the North Atlantic and western Europe [Pilidou, et al., 2005]. They observe a rotation of the fast axis orientation from N-S west of Iceland to NW-SE east of Iceland (the lateral resolution is several hundred kilometers), which is consistent with the trend we see from west to east across Iceland. Compared with the two previous studies of shear-wave splitting across Iceland [Bjarnason, et al., 2002; Li and Detrick, 2003], we add new observations at HOT27, HOT12, HOT11, HOT14, HOT26 and all SIL stations. Although most of our splitting observations are consistent with previous studies, there are two exceptions at station HOT27 and HOT12 in central Iceland (Fig. 2.3). At station HOT27, the splitting direction we observed is NW-SE, which is almost perpendicular to NE-SW observed by Li and Detrick (2003) and NNE-SSW observed at nearby station BLOL by Bjarnason and Silver (2002). At station HOT12, the splitting direction we observed is NW-SE, different from N-S observed by Li and Detrick (2003). We note that the NW-SE fast axes indicated by our splitting observations at HOT12 and HOT27 are consistent with observations at surrounding stations. Fig. 2.4 shows the splitting parameters of ϕ as a function of event back-azimuth at station HOT27 and HOT12. On the basis of consistency between adjacent stations we also expect a NW-SE fast axis for HOT11. However we can only make null observations given the limited range of back azimuths to events providing good SKS observations at

HOT11. These nulls could indicate isotropic structure or anisotropy with a fast axis parallel or perpendicular to the back azimuth. In the case of HOT11, we prefer an interpretation with a NW-SE oriented fast axis, i.e. anisotropy similar to surrounding stations. We also performed bootstrap tests of stacked splitting parameters to new observations at HOT27, HOT12, HOT13, HOT14, SIG and GRI, showing that these new observations are robust.

In our study, after stacking 11 events at station HOT07, we observed a very large apparent splitting time of 2.8 sec. For each event, we observed only negligible energy with respect to noise levels on the original transverse seismogram, energy contours elongating in the δt direction, and/or poorly constrained optimal ϕ and δt . The apparently large δt is therefore more likely due to noise rather than real signal and was discarded.

2.4 Interpretation of shear-wave splits

2.4.1 Source depth of the anisotropic signal

Because the conversion from an S- to P-wave in the outer core removes any splitting due to the source-side of the path, SKS splitting measurements represent an integral along the mantle ray path on the receiver side. As the ray path is nearly vertical through the mantle and crust, the anisotropy is located within a nearly vertical column beneath the station. Silver (1996) studied contributions of various layers in the Earth to SKS splitting times. He found the average contribution from the crust to be 0.2 sec, and the

contribution from the lower mantle and transition zone to be typically less than 0.2 sec. He concluded that the SKS splitting times (with typical values of 1 sec) arise primarily from anisotropy in the upper mantle beneath the Moho [*Silver, 1996*]. In Iceland, splitting times of 0.1-0.3 sec are observed in the crust beneath the Western Volcanic Zone and smaller splitting times of 0.1 sec are observed in South Iceland Seismic Zone [*Menke, et al., 1994*]. Our observed SKS splitting times of up to 2 sec therefore suggest that any crustal contribution to SKS splitting times is small and the upper mantle is the primary source.

Two features of our data also suggest that the anisotropy we observed is in the upper mantle. Firstly, the close proximity of adjacent stations in Iceland results in near-identical lower-mantle ray paths from a single event. It is only in the upper mantle that ray paths to western and central Iceland are distinct while differences in splitting time of up to 1 sec are observed. This requires strongly heterogeneous anisotropy in the upper mantle. Secondly, the insensitivity of the fast axis orientation at a single station to event back azimuth implies a shallow source as it is only in the upper few hundred kilometers that rays from multiple events to the same station share the same path.

We conclude that in central and eastern Iceland the upper mantle is the primary source of anisotropy for the following reasons: (1) the previously observed crustal splitting times are roughly a factor of six smaller than what we observed in central and eastern Iceland, (2) our splitting times do not correlate with crustal thickness, and (3) splitting orientations do not correlate with surface structures. In western Iceland, the

contribution of the crust may be more important. Our splitting observations in the Westernfjords are only a factor of 2 to 3 greater than typical crustal splitting times. This may suggest that the upper mantle is more isotropic or the apparent thickness of the asthenospheric layer of anisotropy is thinner beneath western Iceland.

2.4.2 Single layer of anisotropy

Our interpretation of the SKS splitting observations assumes a single layer of uniform anisotropy. If there were multiple layers of anisotropy, there would be a dependence of splitting times and/or splitting directions on back azimuth. In our splitting observations, neither ϕ nor δt show a significant dependence on back azimuth. Fig. 2.5a and b show the splitting parameters of ϕ and δt as a function of event back-azimuth at station HOT17. Splitting observations for individual events are quite uniform with small variations for different back-azimuths, indicating that a single layer of anisotropy dominates the observations. Further, we observe null splits at more than ten stations for events whose back azimuth is near-parallel or -perpendicular to the splitting directions observed using other events. If there was more than one layer of anisotropy, a null result could not be observed except in the unusual case in which different layers cancel the anisotropy of one another exactly. Given the incomplete coverage of event back azimuth and the low frequency of the SKS waveforms used, it is still possible that additional layers of relatively thin anisotropy are present beneath Iceland. If such layers exist, they are most likely beneath western Iceland as the area shows weak anisotropy with less well-constrained splitting directions. Similar splitting observations have been made in the case

of layered structures [*Favier and Chevrot, 2003*] or vertical heterogeneity [*Saltzer, et al., 2000*]. In central and eastern Iceland we interpret our splitting results in terms of a single layer of anisotropy by which we mean a single layer of anisotropy dominates the splitting observations.

It is impossible to determine the thickness of an anisotropic layer generating SKS splits as the layer thickness and strength of the anisotropy trade-off against one another. To get a sense of the order of magnitude of the thickness of the anisotropic layer beneath Iceland we assume that the strength of anisotropy is similar to the average 4% anisotropy observed in natural peridotites from 120 to 170 km depth [*Mainprice and Silver, 1993*]. Given 4% anisotropy a 2 sec delay would be generated by a 200 km thick layer.

2.4.3 Relating flow to the fast splitting direction

The relation between the mantle flow direction and mineral preferred orientation is complicated as different olivine fabrics develop not only for different types of deformation, such as simple shear, pure shear, and axial compression, but also with different strain amplitudes [e.g., *Nicolas, et al., 1973; Ida, 1984; Parks and Ahzi, 1990; e.g., Ribe and Yu, 1991; Wenk, et al., 1991*]. While simple shear is believed to be the dominant mode of deformation in the upper mantle [e.g., *Nicolas, et al., 1973; e.g., Zhang and Karato, 1995*], deformation types other than simple shear may exist in the vicinity of Icelandic upwelling. When flow occurs in simple shear the olivine a axis tracks with the strain ellipsoid. For relatively small strains (e.g., lower than ~75%

[Zhang and Karato, 1995]), olivine a axes are closely aligned with the principal axis of strain ellipsoid within the foliation plane, and at an angle of 45° counterclockwise from the flow direction [Ribe and Yu, 1991; Wenk, et al., 1991; Zhang and Karato, 1995]. With progressive strain, olivine a axes follow the strain ellipsoid and rotate towards the flow plane [Ribe and Yu, 1991; Wenk, et al., 1991] becoming subparallel to the flow direction for large strains ($\sim 150\%$) [Zhang and Karato, 1995]. Thus olivine a axes are expected to be parallel to asthenospheric flow for large strain by simple shear. Given the complex flow close to the upwelling conduit beneath Iceland (within ~ 100 km) we cannot assume simple shear across a horizontal plane. Instead we might expect more variable crystallographic orientations due to both different types of deformation and magnitudes and orientations of strain. An SKS phase traveling through such complex structure would not develop a simple split due to reduced amplitude on the tangential component caused by scattering [Saltzer, et al., 2000]. We would therefore expect null or small delay time splitting observations close the upwelling axis. In our interpretation we make the simplifying assumption that away from the upwelling conduit material is flowing away from Iceland by simple shear on a horizontal plane. Close to the upwelling axis the more complex relationship between crystallographic axes and flow is likely to result in small or no splitting delays. Given the assumption of simple shear, we must still consider the effect of water [Jung and Karato, 2001] and melt [Holtzman, et al., 2003] on the relationship between flow direction and crystallographic orientation, both of which are possible beneath Iceland.

2.4.3.1 The influence of water on the fast splitting direction

The experimental study by Jung and Karato (2001) questions the assumption that flow directions are generally parallel to the seismically fast splitting direction corresponding to the type-A fabric of olivine [Jung and Karato, 2001]. Their results show that when water is added to olivine, the relation between seismic anisotropy and flow geometry undergoes marked changes. In addition to the well-known type-A fabric in which the olivine [100] axis is subparallel to the shear direction and the (010) plane is subparallel to the shear plane, they identified two new types of fabric: type-B and type-C. In type-B, the olivine [001] axis is subparallel to the shear direction and the (010) plane is subparallel to the shear plane. In type-C, the [001] axis is subparallel to the shear direction and the (100) plane is subparallel to the shear plane. In addition to the above three types of fabric, a fourth type of fabric, type-D, has been reported [Bystricky, *et al.*, 2000]. Type-D develops at high strain, and has a sharp [100] maximum oriented parallel to the shear direction and girdles of [010] and [001] normal to that direction. Jung and Karato [49] concluded that type-A dominates at low stress and low water content, type-B dominates at high water content and/or high stress, type-C dominates at high water content and modest stress, and type-D dominates at high stress and low water content. In type-A, type-C, and type-D fabrics, the fast splitting direction of an S-wave is subparallel to the flow direction (in a horizontal flow for type-A and type-C; the shear plane can not be identified for type-D); whereas in type-B fabric, the fast splitting direction of the S-wave is nearly perpendicular to the flow direction (in a horizontal flow) [Bystricky, *et al.*, 2000; Jung and Karato, 2001]. Although type-B fabric has a significant influence on the lattice preferred orientation, the required conditions for type-B fabric to dominate (high

stress and high water content) are not common in the mantle [Kaminski, 2002]. Thus before interpreting our splitting observations, it is important to know the water content and the state of stress beneath Iceland to derive the fabrics of olivine and corresponding relations between the fast splitting direction and the flow direction.

Geochemical studies suggest that Iceland is not only a hotspot but also a wetspot. A comprehensive petrological and geochemical study of basalts dredged along the axis of the Mid-Atlantic Ridge from 29°N to 73°N shows that the mantle beneath Iceland is enriched in water [Schilling, *et al.*, 1983]. Water concentrations show an increasing trend from south of 61°N to Iceland [Poreda, *et al.*, 1986], reaching 0.47 wt.% in Iceland [Metrich, *et al.*, 1991]. They are 1.5 to 4 times higher than typical mid-ocean ridge basalts (0.12 wt.%; [Byers, *et al.*, 1986]). Water concentrations of between 620 and 920 ppm have also been measured in basaltic glasses from submarine and subglacial eruption sites along the Reykjanes Ridge and Iceland, respectively [Nichols, *et al.*, 2002]. All these observations suggest that Iceland is a wet hotspot.

Stress is the other key factor to decide the dominant fabric type of olivine beneath Iceland. Although there are no direct stress measurements available for the Icelandic upper mantle, we assume that the state of stress beneath Iceland is similar to that beneath typical rift zones as Iceland is located on the Mid-Atlantic Ridge. Peridotites from typical rift-zone environments and xenoliths from ocean island basalts show stress magnitudes of ~1 to 10 MPa [Mercier, 1980]. Therefore, we expect the magnitude of stress to be low. In such low stress and medium to high water content (between 620 and 920 ppm)

environments, type-A and type-C fabrics of olivine dominate [*Jung and Karato, 2001*]. Both type-A and type-C fabric of olivine result in the fast splitting direction of a shear-wave with a nearly vertical ray path being parallel to the flow direction (in a horizontal flow). Thus, despite the high water content, the parallelism between the seismic fast axis and the flow direction should hold beneath Iceland due to the expected low stress environment.

2.4.3.2 The influence of melt on the fast splitting direction

Holtzman et al. (2003) deformed partially molten mantle rocks under anhydrous conditions and observed that melt-rich layers cause a switch of the a- and c-axes, resulting in a fast direction perpendicular to the shear direction [*Holtzman, et al., 2003*]. The importance of this observation for the interpretation of anisotropy beneath Iceland is dependent on the percentage of melt in the mantle beneath Iceland and its geometric extent, which we now consider.

Geophysical studies of the uppermost mantle beneath Iceland do not require the presence of melt to explain velocity anomalies which has lead to an estimated upper bound of 1% melt fraction [*Staples, et al., 1997; Darbyshire, et al., 2000*]. More recently, observed disequilibrium of U-series activity ratios in Iceland requires melt to separate from the source region when the melt fraction exceeds a few tenths of a percent, and suggests that the melt reaches the surface within 20 years [*McKenzie, 2000*]. These observations indicate that only a small melt fraction is retained beneath Iceland. In

comparison, the experiments of Holtzman et al. (2003) used samples with melt fractions ranging from 2 to 15%, although more recent experiments with as little as 0.5% melt also show the melt bands resulting in a switch of the a- and c-axes (Holtzman, personal communication). It is therefore likely that the melt fraction beneath Iceland is less than in the experiments of Holtzman. However, it is still possible that a similar switch of the a- and c-axes occurs for the very low percentage of melt we expect beneath the region.

Inversion results using REE compositions of the olivine tholeiites from Iceland suggest that melting initiates at a depth of 120 to 140 km, and stops at depths as shallow as 20 to 22 km [Nicholson and Latin, 1992; White and McKenzie, 1995; MacLennan, et al., 2001; Slater, et al., 2001]. Both geochemical [MacLennan, et al., 2001] and volumetric arguments [Allen, et al., 2002a] suggest there is buoyant upwelling beneath Iceland as mantle material is fluxed through the melt zone more rapidly than passive upwelling would allow. Numerical models [Blackman, et al., 1996] show that in buoyant upwelling, melt is focused within a narrow zone about 50 km across beneath a ridge compared to the much broader ~150 km wide zone of melting when upwelling is passive. If there is any effect of melt on splitting observations beneath Iceland it is therefore most likely confined to a narrow region a few tens of kilometers wide beneath the ridge. Pilidou et al (2005) completed a regional Rayleigh wave study of anisotropic velocity structure beneath the North Atlantic. Their study is not sensitive to variations in anisotropy on a scale less than ~400 km and shows a rotation of the fast axes from NNW-SSE east of Iceland to more N-S west of Iceland in the upper 250 km. Given the sensitivity of Pilidou et al's Rayleigh wave study their observations are not sensitive to

melt beneath the Icelandic mid-ocean ridge. Our splitting observations show the same trend as Pilidou et al. with fast axis orientations NNW-SSE in eastern and central Iceland, and N-S in western Iceland implying that our observations are not sensitive to any melt either.

In our following interpretation we neglect any effect of melt on the orientation of crystallographic axes with respect to flow. We make this assumption on the basis that (1) the percentage of melt beneath Iceland is smaller than in the Holtzman experiments, (2) any melt is probably focused in a narrow region beneath the ridge, and (3) our observations are consistent with the broad trend of Pilidou et al [Pilidou, *et al.*, 2005] which is not sensitive to melt.

2.4.4 Comparison of splits with conceptual mantle flow geometries

Bjarnason et al. (2002) summarized five potential conceptual horizontal mantle flow geometries beneath Iceland: flow associated with relative plate motion perpendicular to the ridge, flow associated with absolute plate motion, background mantle flow, hotspot-related radial flow, and rift-parallel flow ([Bjarnason, *et al.*, 2002] and references therein). We now compare the orientations of our splitting observations with the anticipated flow geometries from these models.

In the flow geometry associated with relative plate motion, mantle material rises beneath the ridge axis and spreads in the direction of relative plate motion, perpendicular

to the ridge. For this geometry, we would expect weak splitting in the neovolcanic zone due to the nearly vertical a-axes of olivine associated with upwelling, and strong splitting with the fast splitting direction aligned with the spreading direction WNW-ESE away from the ridge. This ridge perpendicular geometry has been observed previously at fast-spreading mid-ocean ridges such as the East Pacific Rise [Forsyth, *et al.*, 1998; Wolfe and Solomon, 1998]. Our splitting observations are not ridge perpendicular, suggesting that this flow geometry has little contribution to mantle anisotropy beneath Iceland.

If the flow associated with absolute plate motion is the cause of the anisotropic structure beneath Iceland, we would expect splitting observations east of the ridge to represent the Eurasian plate motion while splits to the west represent the North American plate motion. Absolute plate motion in western Iceland is in a westerly direction while in eastern Iceland, the plate velocity is not significantly different from zero [Gripp and Gordon, 1990]. Thus we would expect strong splitting with a westerly fast splitting direction in western Iceland and negligible splitting in eastern Iceland. This also does not match our splitting observations.

If background mantle flow is responsible for the anisotropic structure, we would expect uniform splitting with a coherent fast splitting direction throughout Iceland, because the background mantle flow is expected to be homogeneous across Iceland, although its direction is unknown. Instead, our splitting observations show a range of fast axis orientations.

In the hotspot-related radial flow geometry (Fig. 2.6a), material rises vertically at the center of the upwelling conduit and diverges radially from the upwelling axis at the base of the lithosphere. We would therefore expect weak splitting at the center of the upwelling due to vertically aligned olivine a-axes surrounded by a radial pattern of fast splitting directions. The amplitude of our observed splits is noticeably smaller in the region of upwelling centered close to HOT23, Fig. 2.3, and in north-central Iceland our fast splitting directions do show a gradual rotation consistent with a radial pattern away from the upwelling center. However, in western and eastern Iceland, our fast splitting directions are almost perpendicular to the predicted radial pattern.

In the rift-parallel flow geometry (Fig. 2.6b), mantle material flows along the rift zones and we expect fast splitting directions parallel to the rifts. Most of the North American-Eurasian spreading is accommodated by the northern and eastern neovolcanic zones as indicated by the plate boundary on Fig. 2.6b. Thus the Mid-Atlantic plate boundary in Iceland is offset ~200 km to the east with respect to the plate boundary to the north and south of Iceland. It is therefore possible that any rift-parallel flow is occurring at two scales. At the smaller scale, just beneath Iceland, rift-parallel flow would be N-S beneath the neovolcanic zones. At the larger scale of the North Atlantic, rift-parallel flow would be NE-SW and run beneath western Iceland. This anticipated rift-parallel flow geometry fits our splitting observations in western and eastern Iceland, but does not match observations in central Iceland.

Bjarnason et al (2002) interpreted their splitting observations on Iceland as the result of relative plate motion over background mantle flow. This model predicts that splitting observations align with the vector sum of the mantle flow and the plate motion resulting in one fast axis orientation for each plate. Their splitting observations fell into two groups with one consistent fast direction for the North American plate and one for the Eurasian plate. This is not the case for our observations as the fast directions in western Iceland are very different from those in central Iceland while all being on the North American plate. The variation in fast direction on the North American plate was not as apparent in Bjarnason et al's study as they had fewer stations in westernmost Iceland.

2.5 Ridge-channeled flow

Although none of the individual models described above is completely consistent with our splitting observations, rift-parallel components are observed in western and eastern Iceland, and a radial geometry away from the axis of upwelling is observed in central Iceland. We therefore propose a hybrid ridge-channeled flow model which is consistent with most of our splitting observations and previous hypotheses for the flow path of mantle material upwelling beneath Iceland [Vogt, 1976; Schilling, 1985; White, *et al.*, 1995; Yale and Morgan, 1998; Albers and Christensen, 2001]. We propose that upwelling material is channeled along the North Atlantic Ridge rather than flowing radially away from the upwelling. For material to flow north and south away from Iceland along the Mid-Atlantic Ridge, upwelling material must flow from the upwelling

center in SE Iceland to the southern end of the Kolbeinsey Ridge and the northern end of the Reykjanes Ridge both of which are west of the upwelling center (Fig. 2.7).

In central Iceland we suggest that the NW-SE orientation of fast axes indicate the flow of material from the upwelling toward the asthenospheric channel beneath the Kolbeinsey Ridge. The rotation of fast axes to more NNW-SSE direction in northeastern Iceland is consistent with both radial flow away from the upwelling and flow toward our proposed asthenospheric channel to the north. The splitting observations in easternmost Iceland are inconsistent with a simple radial flow geometry, but are consistent with flow toward an asthenospheric channel beneath the Kolbeinsey ridge. In western Iceland, farther away from the Icelandic upwelling, the NNE-SSW orientation of fast axes is parallel to the trend of the Kolbeinsey and Reykjanes ridges.

It is also noticeable that the splitting delay times at stations surrounding the axis of upwelling (centered close to HOT23 – see Fig. 2.3 and 2.7) are relatively small. A gradual increase in delay time with distance from HOT23 to the northeast is evident at stations HOT20, HOT25, HOT24 and HOT18 etc. Station HOT22 and HOT21 to the south show only null observations, and stations in the southern half of central Iceland exhibit small delays or nulls with the exception of HOT28. This may reflect either vertical flow and vertical a-axes within the upwelling and/or a more complex flow geometry and variable crystallographic orientations resulting in scattering of polarized energy and reduced delay times as described in section 2.4.3.

Southernmost Iceland does not provide splitting observations to support our hypothesis. Unfortunately there are few stations between the upwelling and the Reykjanes ridge with which to map flow. HOT21 and HOT22 show null observations (Fig. 2.3) consistent with their location close to the center of the upwelling. Stations HOT28 and KRO (Fig. 2.3) are not consistent with the proposed flow geometry being oriented NW-SE rather than SW-NE as we might expect for flow toward the Reykjanes asthenospheric channel.

The horizontal flow of material away from the upwelling axis is most likely confined to the upper few hundred kilometers given the different fast direction orientations between adjacent stations and a lack of back azimuth dependence at individual stations. Regional isotropic tomography models for Iceland [Allen, *et al.*, 2002a] show upwelling material spreading out laterally beneath the Icelandic lithosphere and forming a layer ~200 km thick. If the layer of anisotropy responsible for our splitting observations is 200 km thick it would need to have 4% anisotropy to generate splitting delays up to 2 sec as we observed. This is consistent with the typical value of 4% anisotropy observed in natural peridotites from ~150 km depth [Mainprice and Silver, 1993].

The systematic variations in the rare earth elements, minor elements and isotopic ratios of basalts also suggest that material from the Icelandic upwelling flows down the Reykjanes and Kolbeinsey ridges [Schilling, 1973; Schilling, 1985; Poreda, *et al.*, 1986; Schilling, *et al.*, 1999]. Isotopic constraints as well as thermal anomalies suggest that the Icelandic upwelling influences 2400 km of the Mid-Atlantic Ridge [Taylor, *et al.*, 1997],

including the entire length of the Reykjanes Ridge and ~600 km on the Kolbeinsey Ridge [Schilling, 1973; Poreda, *et al.*, 1986]. While the observed straightness of V-shaped ridges has been used to argue for channeled flow [Vogt, 1976; Schilling, 1985; White, *et al.*, 1995; Yale and Morgan, 1998; Albers and Christensen, 2001], Ito showed that radial flow can also predict V-shaped ridges [Ito, *et al.*, 1996; Ito, 2001] and the only slight curvature expected would be difficult to discern given the relatively high velocity at which the upwelling material is expected to flow horizontally (~100 mm/yr [White, *et al.*, 1995]) compared with the plate spreading rate (~10 mm/yr). We propose that the seismic anisotropy observations described here also supports the hypothesis that upwelling material is preferentially channeled down the adjacent mid-ocean ridges and are inconsistent with radial flow away from the upwelling.

Should our ridge-channeled model be appropriate, it is interesting to note that in some respects Iceland should be treated as an off-ridge hotspot. The proposed flow geometry is consistent with the predicted channeling of hotspot material to adjacent mid-ocean ridges from off-ridge hotspots [Schilling, 1985; Kincaid, *et al.*, 1995; Small, 1995; Kincaid, *et al.*, 1996; Kingsley and Schilling, 1998]. Iceland is usually considered a ridge-centered hotspot; however, the short ridge-segment across Iceland (~350 km in length) is offset from the rest of the North Atlantic Ridge by ~200 km. The horizontal flow of upwelled material beneath Iceland therefore represents both a ridge-perpendicular channel feeding material back to the ridge, and subsequent flow of this material along the ridge in asthenospheric channels.

2.6 Conclusion

Shear-wave splitting observations across Iceland can be related to asthenospheric flow, providing constraints on the interactions of the Icelandic upwelling, the Mid-Atlantic Ridge and larger scale North Atlantic convection processes. Our splitting observations lead to the following conclusions regarding the anisotropic structure and flow beneath Iceland.

1. The primary source of anisotropic signal as observed by teleseismic shear-wave arrivals is the upper mantle. Since crustal splitting times in Iceland are 0.1 to 0.3 sec, our delays of up to 2 sec require a mantle source. Both the close proximity but dissimilarity of anisotropy observations for stations in western and central Iceland, and the insensitivity of inferred anisotropy to back-azimuth, require that the anisotropic structure is located in the upper mantle.

2. The anisotropic structure beneath Iceland is dominated by a single layer of anisotropy. First, the lack of dependence of the splitting parameters on event back azimuth suggests one-layer model. Second, the observations of null splits for events where the back azimuth is near-parallel or -perpendicular to the fast splitting directions (observed using other earthquakes) also indicates that one layer of anisotropy dominates.

3. While both high stress plus enriched water content and melt-rich layers can result in a 90° rotation of the fast shear-wave splitting direction with respect to the flow

direction, we expect the fast axis of shear-wave splits to be parallel to the flow direction beneath Iceland as the magnitude of stress is low and the amount and lateral extent of melt is likely small.

4. We hypothesize that the observed anisotropy pattern beneath Iceland represents ridge-channeled flow: horizontal flow of upwelling material toward and then along the North Atlantic Ridge. The splitting observations are consistent with flow from the upwelling axis to the southern end of the Kolbeinsey Ridge but are not consistent with radial flow of material away from the upwelling. We propose that upwelling material also flows to the northern end of the Reykjanes Ridge and that the V-shaped ridges to the north and south of Iceland are the product of this channeled flow along asthenospheric channels.

Figure captions

Fig. 2.1 Seismic stations used in this study: HOTSPOT (circles) and SIL (triangles) stations. The gray segments show fissure swarms indicating where the Mid-Atlantic Ridge crosses the island, and the circular features represent central volcanoes.

Fig. 2.2 Distribution of the 28 events used in this study. The black dots indicate the locations of earthquakes, and gray circles mark 60° , 120° , and 180° from Iceland.

Fig. 2.3 Splitting results across Iceland. At each station the line orientation gives the fast splitting direction ϕ , and its length is linearly proportional to δt . The black lines indicate the results from our study with the thickest lines indicating fast axis orientation and thin crosses indicating null results. The light gray wedges indicate the 95% confidence region in the polarization direction. The thin dark gray lines indicate the results from Bjarnason et al. [2002]; the thin light gray lines indicate the results from Li and Detrick [2003]. Also indicated are the neovolcanic zones (gray region) and glaciers (light gray shades).

Fig. 2.4 Fast splitting directions ϕ as a function of event back-azimuth for station HOT27 (a) and HOT12 (b). Black dots and vertical solid lines indicate ϕ and corresponding uncertainties, respectively. Circles connected by dotted lines indicate the two candidate fast directions from null results. Horizontal gray bars illustrate the best fit f calculated from stacking the splitting observation from all the events.

Fig. 2.5 Splitting parameters (a) ϕ and (b) δt as a function of event back-azimuth for station HOT17. Black dots indicate ϕ in (a) and δt in (b). Other symbols have the same meaning as in Fig. 2.4.

Fig. 2.6 Conceptual mantle flow geometries beneath Iceland. (a) The hotspot-related radial flow geometry. (b) The ridge-parallel flow geometry. The black arrows in both figures show the expected horizontal mantle flow directions. The big black circle with a black solid dot in the center indicates the approximate location of the Icelandic hotspot.

Fig. 2.7 Map placing asthenospheric anisotropy observations in the context of the proposed ridge-channeled flow model. The black circle with a dot indicates the center of the Icelandic upwelling. The bold gray lines across central Iceland indicate the plate boundary in the North Atlantic including the eastward step of the ridge across Iceland. The white lines indicate the ages of the lithosphere on either side of the spreading ridge. The orientation and length of each short black line indicates the splitting direction and the splitting time, respectively. The thick gray arrows with dotted outlines show the proposed mantle flow directions resulting from preferentially channeling the horizontally spreading upwelled material to, and then along, the Mid-Atlantic Ridges to the south and north of Iceland.

Table 2.1 Earthquakes used in study

No.	Y/M/D	Julian day	Time	Lat.	Long.	Depth (km)	Magnitude	Epicenter distance (°)
1	1996/07/04	186	155038.70	8.49	141.56	33.	5.9	105.1
2	1996/07/16	198	100736.65	1.02	120.25	33.	6.6	107.5
3	1996/07/22	204	141935.77	1.00	120.45	33.	7.0	107.6
4	1996/08/05	218	223822.09	-20.69	-178.81	550.	7.4	133.8
5	1996/09/20	264	000318.37	9.60	126.29	33.	6.4	101.0
6	1996/09/20	264	041027.68	9.46	126.28	33.	6.6	101.1
7	1996/09/20	264	041104.55	9.45	126.33	33.	6.6	101.1
8	1997/03/11	70	192200.13	7.74	127.65	10.	7.2	103.1
9	1997/05/09	129	090637.27	13.20	144.70	29.	6.1	100.9
10	1997/05/22	142	132136.35	18.92	121.34	33.	6.1	90.8
11	1997/05/27	147	150903.76	16.33	145.44	536.	5.6	97.9
12	1997/06/24	175	230453.14	-1.92	127.90	33.	6.4	112.5
13	1997/07/06	187	095400.76	-30.06	-71.87	19.	6.8	103.5
14	1997/07/06	187	231520.49	-30.16	-71.86	33.	5.8	103.6
15	1997/07/08	189	022407.32	23.80	142.70	33.	5.8	90.2
16	1997/07/21	202	231939.35	-30.33	-71.92	33.	6.0	103.8
17	1997/07/27	208	052129.27	-30.52	-71.86	33.	6.3	104.
18	1997/10/04	277	183141.05	-35.29	-106.71	10.	5.7	120.9
19	1997/10/08	281	104749.92	-29.25	178.35	617.	5.7	142.8
20	1997/10/15	288	010333.46	-30.93	-71.22	58.	7.6	104.1
21	1997/11/25	329	121433.63	1.24	122.54	24.	7.0	108.0
22	1997/11/28	332	225341.53	-13.74	-68.79	586.	6.7	87.3
23	1997/12/22	356	020550.08	-5.49	147.87	179.	7.2	119.8
24	1998/05/23	143	174447.77	8.14	123.73	657.	6.0	101.7
25	1998/06/09	160	120455.32	-18.87	-173.31	33.	5.5	131.0
26	1998/06/22	173	202624.91	12.36	144.45	33.	5.7	101.7
27	1998/07/29	210	071424.08	-32.31	-71.29	51.	6.3	105.5
28	1998/07/29	210	180029.99	-2.69	138.90	33.	6.7	115.6

Table 2.2 Shear-wave splitting parameters for HOTSPOT and SIL stations. The σ_ϕ and $\sigma_{\delta t}$ are the standard deviations in ϕ and δt , respectively, and n is the stacked number of records for each station.

Station	$\phi(^{\circ})$	$\sigma_\phi(^{\circ})$	$\delta t(s)$	$\sigma_{\delta t}(s)$	n
HOT01	36	11	0.65	0.30	11
HOT02	20	5	1.20	0.35	9
HOT03		All null results			2
HOT04	-30	21	0.50	0.20	13
HOT05	7	21	0.40	0.175	7
HOT06	-22	22.5	0.20	0.3	15
HOT07	25	1	2.80	0.35	11
HOT08	13	22.5	0.35	0.35	13
HOT09	-3	22.5	0.10	0.2	11
HOT10	2	7.5	0.80	0.125	12
HOT11		All null results			6
HOT12	-43	2	2.00	0.45	7
HOT13	-32	5.5	1.25	0.225	8
HOT14	-39	4	1.00	0.2	12
HOT15	-22	6.5	1.25	0.2	5
HOT16	-19	2	1.20	0.15	11
HOT17	-22	2.5	1.20	0.125	13
HOT18	-27	3	1.45	0.175	6
HOT19	-22	5.5	1.35	0.20	3
HOT20	-3	5	0.85	0.05	7
HOT21		All null results			5
HOT22		All null results			5
HOT23	-17	11	0.80	0.225	6
HOT24	-11	4	1.25	0.1	5
HOT25	-22	12.5	0.90	0.25	5
HOT26		All null results			2
HOT27	-47	1.5	1.70	0.225	8
HOT28	-44	2.5	1.75	0.325	6
HOT29	-17	4.5	1.45	0.425	3
ASB	24	22.5	0.90	0.65	4
VOG		All null result			1
GRI	-33	9.5	1.40	0.425	4
HVE		All null result			3
KRO	-63	3.5	1.40	0.25	3
SIG	-43	2	2.30	0.525	5
SKR		All null result			1
GIL	-36	22.5	1.50	1.175	2
GRA	1	9.5	1.10	0.25	4
GRS	-7	6.5	1.45	0.175	2
REN		All null result			2

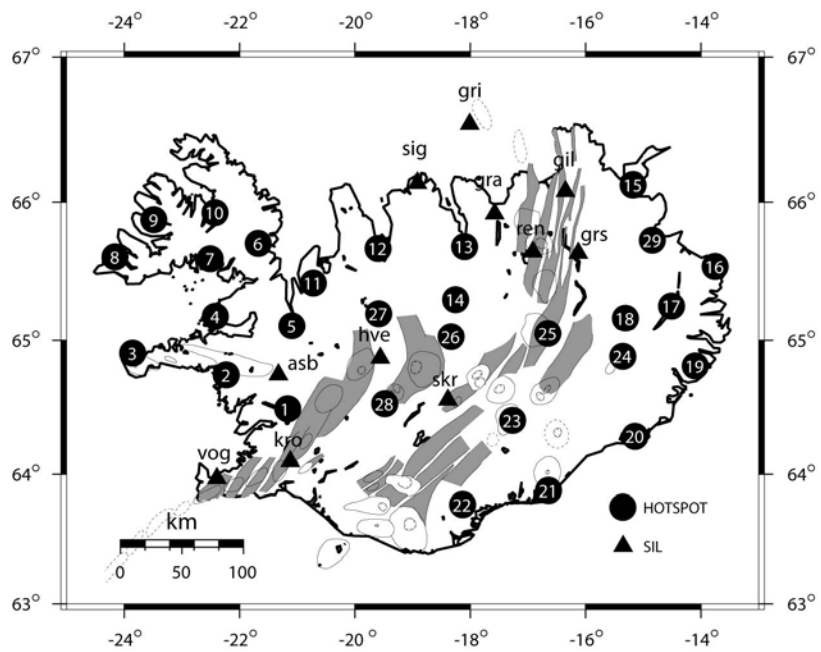


Fig. 2.1

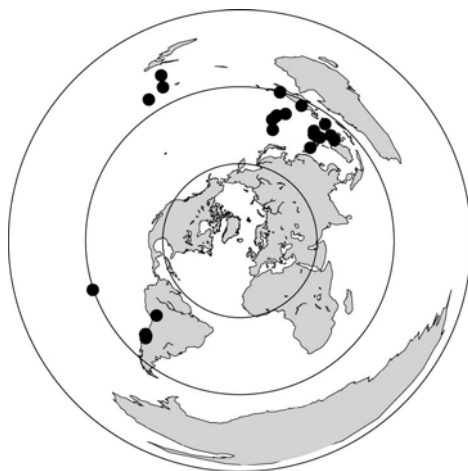


Fig. 2.2

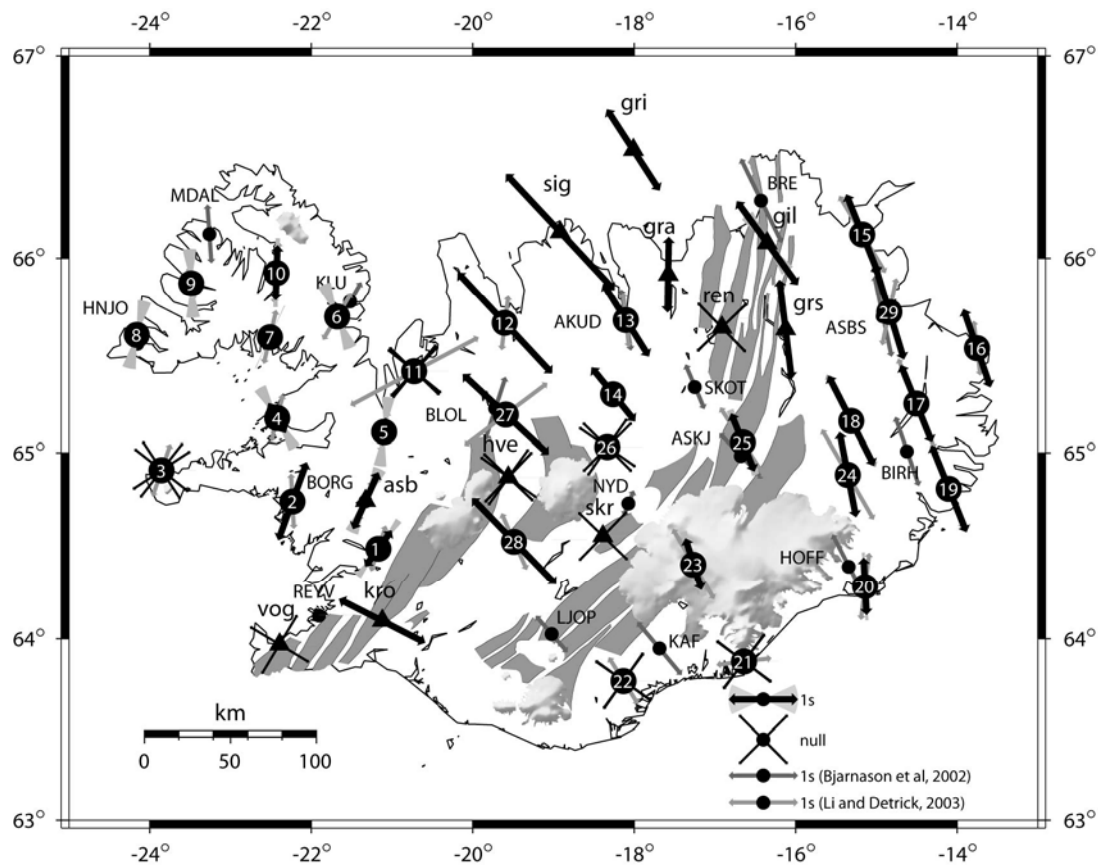


Fig. 2.3

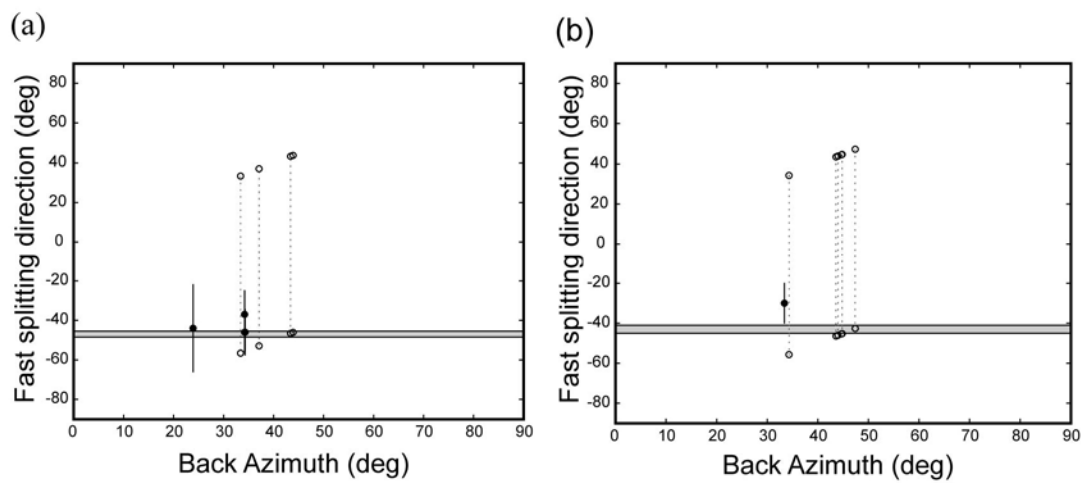


Fig. 2.4

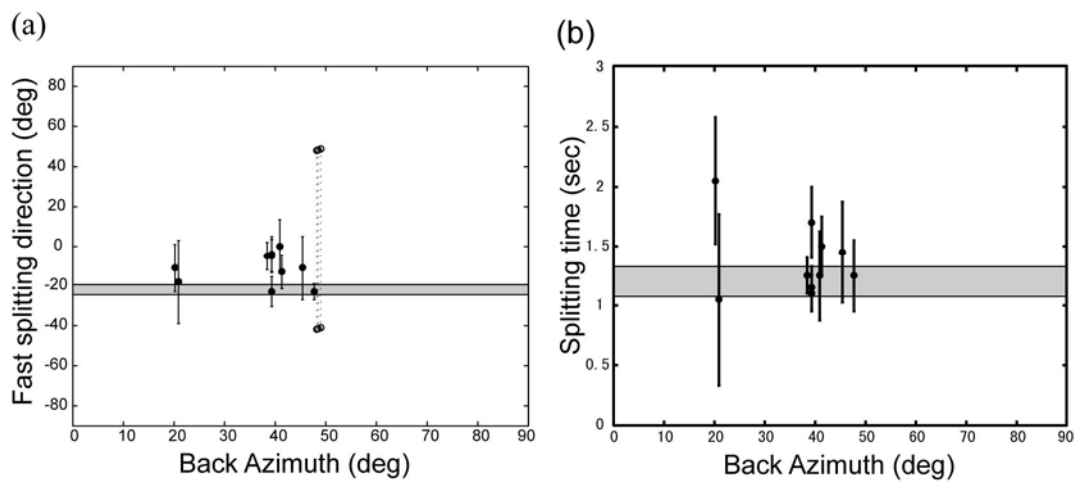


Fig. 2.5

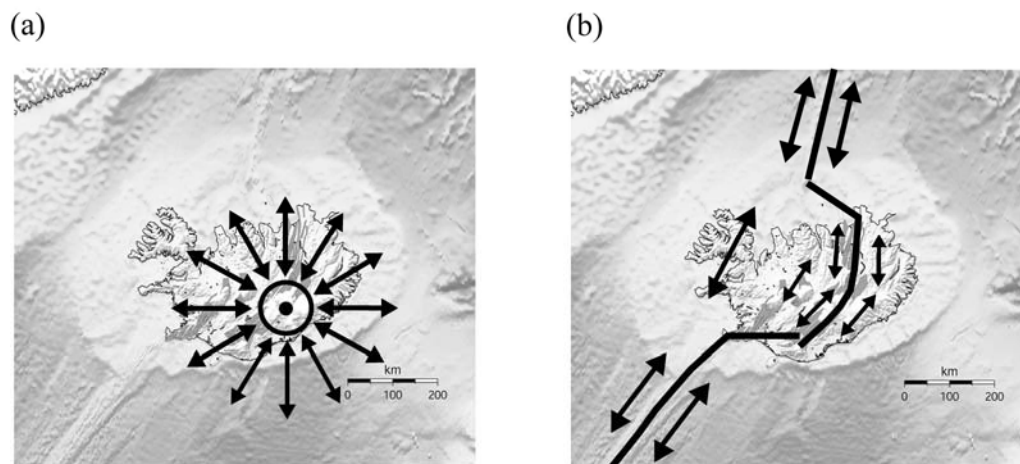


Fig. 2.6



Fig. 2.7

Chapter 3

Origin of the Newberry Hotspot Track

This chapter has been published in *Earth and Planetary Science Letters* with the title of “Origin of the Newberry Hotspot Track: Evidence from shear-wave splitting” [Xue and Allen, 2006].

Summary

Located in the northwestern United States, the Newberry Hotspot Track consists of a sequence of age-progressive silicic volcanic domes and lava flows, showing a monotonic age progression from east to west ending at the Newberry Caldera. While mantle plumes are often called upon to explain hotspot tracks, the Newberry track cannot be the direct product of plate motion over a stationary mantle source as its orientation is $\sim 120^\circ$ to plate motion, making it a good case study for alternative causal mechanisms of hotspot tracks. Four end-member tectonic models have been proposed: (1) subduction counterflow, (2) gravitational flow along the base of the lithosphere, (3) lithospheric faulting, and (4) extension of the Basin and Range. To get fabric information about the asthenosphere and constrain the possible flow fields beneath the Newberry track, SKS splitting measurements were made for 27 events at 12 stations of the Oregon Array for Teleseismic Study (OATS) along the track. A gradual rotation of the fast direction is observed from ENE-WSW at the northwest end of the array to E-W to the southeast and

the delay times average 1.65 sec. We infer that the SKS splits are the product of anisotropy in the asthenosphere and the anisotropy orientation does not vary with depth beneath the track. The average fast directions ENE-WSW to the northwest are consistent with generation by mantle shear parallel to the subduction of the Juan de Fuca Plate, and the more E-W fast directions to the east are perhaps due to shear caused by the Basin and Range extension. Since the observed fast directions are not parallel to the Newberry track, as the subduction counterflow model or the gravitational flow model suggests, the age-progressive volcanism is unlikely a direct product of asthenospheric flow. Instead, we propose that the Newberry track is the product of lithosphere-controlled processes.

3.1 Introduction

Located in the northwestern United States, the Newberry Hotspot Track, along the Oregon High Lava Plains, consists of a sequence of volcanic domes and lava flows. K-Ar dating of rhyolitic domes in the region shows they were widespread from 17 to 11 Ma but domes younger than 10 Ma form two distinct belts each ~250 km long and trending N75°W (Fig. 3.1) [Macleod, *et al.*, 1976; Christiansen and McKee, 1978]. The northern belt of volcanism within the Newberry hotspot track is coincident with the Brothers Fault Zone (Fig. 3.1), a NW-trending fault zone running across the strike of the NE-trending normal faults of the Basin and Range. Isochrones of rhyolitic domes can be drawn across the region showing a monotonic age progression from east to west ending at the Newberry Caldera (Fig. 3.1). More recent $\text{Ar}^{40}/\text{Ar}^{39}$ dating confirms these volcanism trends [Jordan, *et al.*, 2004].

The northwest trending Newberry track crudely mirrors the better-known Yellowstone Hotspot Track, which is associated with northeastward migration of silicic volcanism along the Eastern Snake River Plain ending at the Yellowstone Caldera (Fig. 3.1) [*Christiansen and McKee*, 1978; *Christiansen and Yeats*, 1992; *Pierce and Morgan*, 1992]. Initiation of the Newberry - Yellowstone hotspots occurred near the region of the McDermitt caldera in northern Nevada and is coincident with outpouring of the Columbia River basalts at ~17 Ma [*Christiansen and McKee*, 1978]. The Columbia River basalts extend throughout eastern Oregon, eastern Washington, and western Idaho, and are a series of flows with ages 17-6 Ma, although primarily 17-14 Ma [*Watkins and Baksi*, 1974; *Christiansen and McKee*, 1978; *Christiansen and Yeats*, 1992]. The conduits for these flows lie along a NS-oriented trend, north of the McDermitt caldera and a similar NS-oriented trend of magmatism occurs southward along the Northern Nevada rift zone (Fig. 3.1) [*Camp and Ross*, 2004].

Although both tracks are located on the North American Plate, the Yellowstone track is parallel to the absolute plate motion, while the Newberry trend is oblique to it. The Yellowstone track has been commonly considered as the result of a mantle plume [*Brandon and Goles*, 1988; *Pierce and Morgan*, 1992; *Smith and Braile*, 1994]. This interpretation is consistent with the associated gravity high, topographic high, high heat flow, and geochemical signature, which are characteristic of many hotspots. Yet, despite these features, evidence for an upwelling conduit through the upper mantle beneath Yellowstone remains unclear and the debate continues as to whether a mantle plume is

the origin [Humphreys, et al., 2000; Christiansen, et al., 2002; Ritsema and Allen, 2003; Crosswhite and Humphreys, 2004; Jordan, et al., 2004; Montelli, et al., 2004; Yuan and Dueker, 2005]. The Newberry hotspot is far less studied than Yellowstone and many of its characteristics have yet to be quantified, such as its source, its causal mechanism, and its relation to the Yellowstone track. While the Newberry Hotspot Track is also associated with bimodal age-progressive volcanism, high topography and high heat flow [Christiansen and McKee, 1978; Humphreys and Dueker, 1994a; Jordan, et al., 2004], it cannot be the direct product of a stationary deep mantle plume or any other stationary source, as the hotspot path is northwesterly at $\sim 120^\circ$ to plate motion. Geochemical analyses of Newberry are also limited, but the high $^3\text{He}/^4\text{He}$ ratios often associated with mantle plumes are lacking. Instead there are notable enrichments in Ba, Sr, and Pb, compared with that of mid-ocean ridge basalts, consistent with a subduction component in the source [Jordan, 2005].

3.2 Tectonic models proposed

Four end-member tectonic models have been proposed for the formation of the Newberry Hotspot Track: (1) Subduction counterflow. Counterflow associated with the subduction of the Juan de Fuca plate beneath North America draws material westward across the base of the continental lithosphere [Draper, 1991; Humphreys, et al., 2000; Jordan, et al., 2004; Jordan, 2005]. (2) Gravitational flow along lithospheric topography. Westward flow associated with topography change on the base of the lithosphere. Possible sources of topography include the edge of the craton and the Yellowstone

“plume” head or its residuum [*Humphreys, et al., 2000; Jordan, et al., 2004; Jordan, 2005*]. (3) Lithospheric faulting. Progressive faulting in the lithosphere, initiating near the McDermitt caldera [*Smith, 1977; Pierce, et al., 2000; Rocchi, et al., 2003*]. (4) The extension of the Basin and Range. The enhanced extension at the northern margin of the Basin and Range that propagated with extensional widening of the province [*Christiansen and McKee, 1978; Christiansen, et al., 2002*].

If the Newberry track is a product of asthenospheric processes as model 1 and/or 2 propose, then asthenospheric flow is expected along the length of the hotspot track. Alternatively, if lithospheric processes as proposed by model 3 and/or 4 are responsible for the hotspot track, asthenospheric flow along the hotspot is not required. SKS splits can provide fabric information about the asthenosphere, which constrains the possible flow fields beneath the Newberry Hotspot Track and discriminates between these models.

3.3 Shear-wave splits

Data were collected from the Oregon Array for Teleseismic Study (OATS). The OATS array includes eleven 3-component broadband seismic stations (Guralp CMG-3ESPD) with average station spacing of 50 km, which were installed in May 2003 and will operate till May 2006. The permanent station COR at Corvallis represents a twelfth station. The array extends from the McDermitt Caldera to the southeast along the Newberry track, past the Newberry Caldera, over the High Cascades and on to the coast within ~100 km of the trench (Fig. 3.1 and 2).

Using data from the first one and half years of the OATS deployment, teleseismic events with magnitude equal or greater than 6.3 and epicentral distances greater than 85° were carefully examined. A total of 27 events provide clear SKS or SKKS phases (Fig. 3.2 inset). A low-pass filter at 10 sec was applied to reduce microseismic noise before making splitting measurements. Splitting parameters were determined by minimizing the tangential energy of SKS or SKKS arrivals [*Silver and Chan, 1991*]. As a quality control, events were discarded if their splitting parameters have errors greater than 1 sec in splitting time δt and/or greater than 22.5° in fast direction ϕ at the 95% confidence level. Average splitting parameters at each station were then determined through a stacking procedure [*Wolfe and Silver, 1998*] and are shown in Fig. 3.2. The station-averaged fast directions for the OATS array show a gradual rotation from ENE-WSW at the northwest end of the array to E-W to the southeast and the delay times average 1.65 sec.

The splitting fast directions ϕ for individual events from different event back-azimuths show small variations at each station, suggesting a relatively simple anisotropy orientation beneath the array. Splitting times δt show more variation scattered around the stacked splitting time at each station. Fig. 3.3a and b give an example of the splitting parameters of ϕ and δt as a function of event back-azimuth at station OT09. Neither ϕ nor δt show a $\frac{\pi}{2}$ periodicity as a function of event back azimuth, which would be expected if there were two-layers of anisotropy [*Silver and Savage, 1994; Rumpker and Silver, 1998*]. Instead, the fast directions do not vary with event back azimuth suggesting orientation of anisotropy does not vary with depth. The scatter of δt versus event back azimuth may

indicate either thickness variations of anisotropic layers, incidence angle variations, or errors in splitting measurements. The latter is likely more influential as splitting times measured for different events from similar back azimuths also show some variation. Null results were also observed at all 12 stations when the event back azimuth was parallel or perpendicular to the fast direction determined from other events at the same station (Fig. 3.2). The combination of null observations and well-resolved fast directions from other events at the same station indicates that a single layer of anisotropy dominates the splitting observations. Low-pass filtering of the SKS waveforms, and errors in splitting measurements, limit our ability to detect small variations of splitting parameters that would result from the presence of thin layer of anisotropy. However, such small structures, if they exist would be small compared with the likely thickness of a layer necessary to generate ~ 1.6 sec delays. Accordingly, we interpret our splitting results in terms of a single layer of anisotropy beneath the Newberry track.

As the globally-averaged crustal contribution to the SKS splitting is small with an average value of 0.2 sec [*Silver, 1996*], crustal anisotropy is absent in the adjacent Eastern Snake River Plain [*Peng and Humphreys, 1998*], and we see evidence for one layer of anisotropy only, it is unlikely that the crust is contributing significantly to our observations along the Newberry track. Since anisotropy in the lower mantle and transition zone is typically less than 0.2 sec [*Karato, 1992; Gaherty and Jordan, 1995; Silver, 1996; Savage, 1999*], the upper mantle is the most important source of our anisotropic signal. Given that the lithosphere is thin beneath the array [*Lowry and Smith, 1995; van der Lee and Nolet, 1997; Schutt and Humphreys, 2001*], the observed splits are

most likely from an asthenospheric source. This interpretation is consistent with previous studies in the Pacific Northwest [*Schutt, et al.*, 1998; *Schutt and Humphreys*, 2001; *Walker, et al.*, 2004; *Waite, et al.*, 2005].

Although high stress plus enriched water content or melt-rich layers can cause a 90° rotation of the fast axis of olivine with respect to strain [*Jung and Karato*, 2001; *Holtzman, et al.*, 2003], these conditions are uncommon in natural environments [*Mercier*, 1980; *White and McKenzie*, 1995; *McKenzie*, 2000]. Along the OATS array, if such conditions exist, they are most likely at the NW end, which is adjacent to the trench where the subducting slab may introduce water and increase the stress level. However, the influence of the subduction zone on the asthenosphere would not extend beneath the entire array to the SE. Considering the similarity of the fast directions observed along the OATS array from the NW to the SE, and also the consistency with regional results further inland to the east (Fig. 3.4), it is unlikely that subduction is causing a 90° rotation of the fast axis with respect to the flow direction. We therefore interpret our observed fast directions as aligned with the mantle flow direction [*Zhang and Karato*, 1995; *Ben Ismail and Mainprice*, 1998; *Savage*, 1999].

3.4 Discussion

The observed fast directions along the Newberry Hotspot Track are consistent with the contiguous regional pattern of anisotropy (Fig. 3.4). The ENE-WSW fast direction of OATS adjacent to the coast is consistent with splitting observations from other studies

west of the Cascades and parallel to the subduction direction of the Juan de Fuca plate [Bostock and Cassidy, 1995; Fabritius, 1995; Silver and Holt, 2002; Currie, et al., 2004]. The fast direction rotates to E-W inland along the OATS array consistent with observations in the Western Snake River Plain [Walker, et al., 2004]. Further east, uniform southwest orientation of SKS splits have been observed in Yellowstone and the Eastern Snake River Plain, and have been interpreted as a single asthenospheric layer of anisotropy due to the southwesterly motion of North American plate [Schutt, et al., 1998; Schutt and Humphreys, 2001; Silver and Holt, 2002; Waite, et al., 2005].

Our uniform splitting orientations suggest a relatively simple anisotropic structure beneath the OATS array, and they are not parallel to the absolute plate motion of the North American Plate, as observed to the east around Yellowstone and the Eastern Snake River Plain [Schutt, et al., 1998; Schutt and Humphreys, 2001; Silver and Holt, 2002; Waite, et al., 2005]. Our splitting orientations are generally parallel to the subduction direction of the Juan de Fuca Plate west of the Cascades, and more E-W to stations east of OT05, which marks the west boundary of Basin and Range extension. Therefore, the E-W orientation of fast axes may reflect west-directed Basin and Range extension, which is generally E-W to NW-SE [Christiansen and McKee, 1978]. However, we should be aware of that there may be a more complex interaction, and other tectonic processes, such as the flow associated with the subduction of the Gorda slab, Oregon's clockwise rotation, and the influence of nearby Pacific-North America shear or slab roll back, etc., may generate or contribute to the observed anisotropy pattern, which are beyond what our data can constrain.

The first order observation is that the orientation of fast axes along the OATS array are not aligned with the Newberry Hotspot Track, indicating that either the splits are not sensitive to mantle flow oriented along the track or the track is not the product of asthenospheric flow. We prefer the second explanation as our SKS splits show that the orientation of fast axes do not vary with depth. If the Newberry track was the product of asthenosphere flow moving northwest across Oregon, as the subduction counterflow model or the gravitational flow model suggests, we would expect fast splitting directions parallel to the track. Instead our splitting orientations are generally parallel to Juan de Fuca Plate subduction and fit into a much broader regional picture. Given these preliminary observations we suggest that the progressive volcanism across Oregon is more likely a product of lithosphere-controlled processes.

Propagation of lithospheric faulting [*Smith, 1977; Pierce, et al., 2000; Rocchi, et al., 2003*] and the extension of Basin and Range [*Christiansen and McKee, 1978; Christiansen, et al., 2002*] are two candidate lithospheric processes which have been suggested as responsible for the formation of the Newberry Hotspot Track. Oregon has several NW-trending strike-slip faults oriented parallel to the trend of the Newberry track (Fig. 3.1). The Brothers Fault Zone is coincident with the northern belt of volcanism within the Newberry track, and has been interpreted as the northern termination of the Basin and Range accommodating the right-lateral, strike-slip motion between areas of significant extension to the south and areas of much less extension to the north [*Lawrence, 1976; Christiansen and McKee, 1978; Dickinson and Snyder, 1979*]. The transcurrent

motion is accommodated by short, small offset, and NE-trending normal faults arranged en echelon to the NW-trending Brothers Fault Zone [Pezzopane and Weldon, 1993]. Field relations show that extension of these faults is coeval with the eruption of relatively young basalts [Draper, 1991], leading to the interpretation that extensional/transtensional deformation is facilitating the Newberry volcanic progression [Pierce, et al., 2000]. However, new field evidence suggests that the faulting has not propagated across the province in the time frame of migrating volcanism, but rather has occurred throughout the province since at least 7.5 Ma [Jordan, et al., 2004; Jordan, 2005].

Alternatively, the extension of Basin and Range has been proposed as the cause of the Newberry track [Christiansen and McKee, 1978; Christiansen, et al., 2002]. In this scenario, the interaction of the North American, Pacific, and Farallon plates formed two separate transform zones between the Pacific and North American plates, separated by the remnant subduction of Farallon plate (ie. the Juan de Fuca plate) beneath North American Plate. By 17 Ma, the remnant subduction zone became so short due to the migrating triple junction of these three plates and the two transform zones became partially coupled. This coupling produced an E-W to NW-SE extension within part of the North American plate with an axis parallel to the continental margin through the present Great Basin to the Columbia Plateau. This extension initiated a melting anomaly along the western margin of the Archean craton, forming the kernel from which both the Yellowstone hotspot and the Newberry melting anomaly could propagate. As the central extending region approached a stable configuration, active extension and basaltic magma generation became increasingly concentrated outward toward the margins. The extension

was further enhanced where the extending margin intersected the transform boundary with thicker, cooler, more rigid lithosphere to the north. The enhanced extension at the north margin of the extending and thinning lithosphere produced crustal melting at the western side of the melting kernel, and which propagated northwestward with extensional widening to form the Newberry Hotspot Track. While this model is consistent with previous estimates of ~ 10-35 % extension across the Great Basin during the past ~ 17 Ma [*Christiansen and McKee, 1978; Stewart, 1978*], Jordan [2005] argue that the deformation in the High Lava Plain was minor, probably about 1% extension over ~ 8 m.y., insufficient to drive a magmatic system by adiabatic decompression.

3.5 Conclusion

SKS splitting observations across Oregon suggest a simple pattern of anisotropy which varies smoothly across the region. We infer a single layer of anisotropy beneath the Newberry Hotspot Track that is most likely in the asthenosphere. The fast directions are oriented ENE-WSW to the west of the Cascades which is consistent with mantle shear parallel to subduction of the Juan de Fuca Plate. To the east, fast directions are more E-W, perhaps due to shear caused by Basin and Range. Since the observed fast directions are not parallel to the Newberry track, it is unlikely that asthenospheric flow is responsible for the age-progression volcanism. Instead, we suggest the Newberry track is the product of a lithosphere-controlled process. While progressive lithospheric faulting and the extension of Basin and Range have also been called upon to explain the formation of the Newberry track previously, supporting field evidence is still lacking.

Figure captions

Fig. 3.1 Tectonic map for the study region. The age-progressive volcanic products of the Newberry and Yellowstone hotspots are shown in black. Both initiate in the region of the McDermitt Caldera (MC). Age contours of initial rhyolitic volcanism along the Newberry track are shown in 1 Ma increments extending to the Newberry Caldera (NC) [3]. Major rhyolitic caldera centers from Owyhee Plateau (OP) along the Yellowstone track are shown with age in Ma extending to the Yellowstone Caldera (YC) [*Pierce and Morgan, 1992*]. Dike swarms associated with the ~17 Ma basaltic outpourings are shown in gray: Chief Joseph Dike Swarm (CJDS), Steens Basalt (SB), and Northern Nevada Rift Zone (NNRZ) [*Christiansen and Yeats, 1992; Camp and Ross, 2004*]. Strike-slip faults zones across Oregon are shown in gray lines [*Lawrence, 1976*]. Twelve stations used in this study are shown as white squares, numbered from OT01 at the west end to OT12 at the east end. Plate motions are shown as white arrows.

Fig. 3.2 Splitting results across Oregon. The thick gray line indicates the result after stacking all useful events at each station. The line orientation gives the fast splitting direction, and its length is linearly proportional to the splitting time. The thin black crosses indicate null results. Inset: distribution of the 27 events used in the SKS splitting study, where the black dots indicate the locations of earthquakes.

Fig. 3.3 Splitting parameters (a) the fast splitting direction and (b) the splitting time as a function of event back-azimuth for station OT09. Black dots and vertical solid lines indicate splitting parameters and corresponding uncertainties, respectively. Circles connected by dot lines indicate two candidate fast directions for null results. Horizontal gray bars illustrate the best-fit ϕ and δt calculated from stacking all splitting observations at OT09.

Fig. 3.4 Oregon splits shown in regional context. Oregon splits are plotted as thick black lines; other measured splits are shown with thin, solid lines; and null splits are plotted as short light gray lines [*Bostock and Cassidy, 1995; Fabritius, 1995; Schutt, et al., 1998; Savage and Sheehan, 2000; Schutt and Humphreys, 2001; Savage, 2002; Silver and Holt, 2002; Currie, et al., 2004; Walker, et al., 2004; Waite, et al., 2005*].

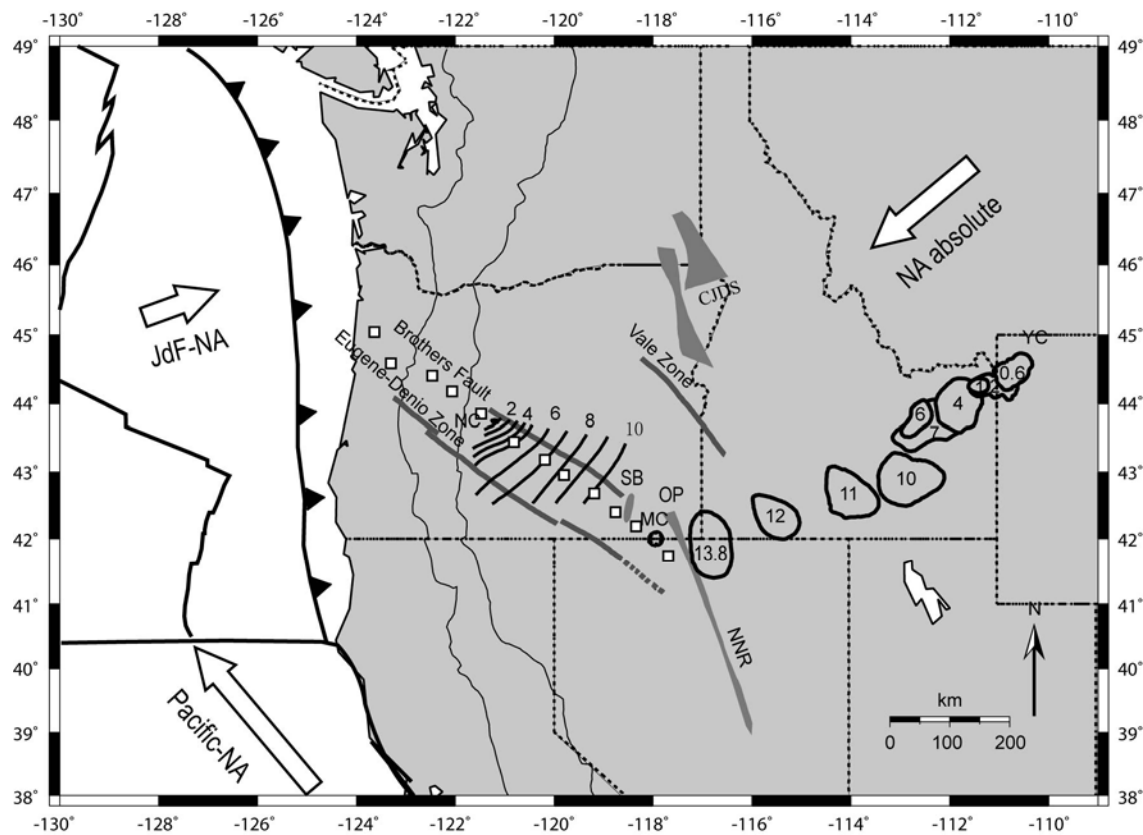


Fig. 3.1

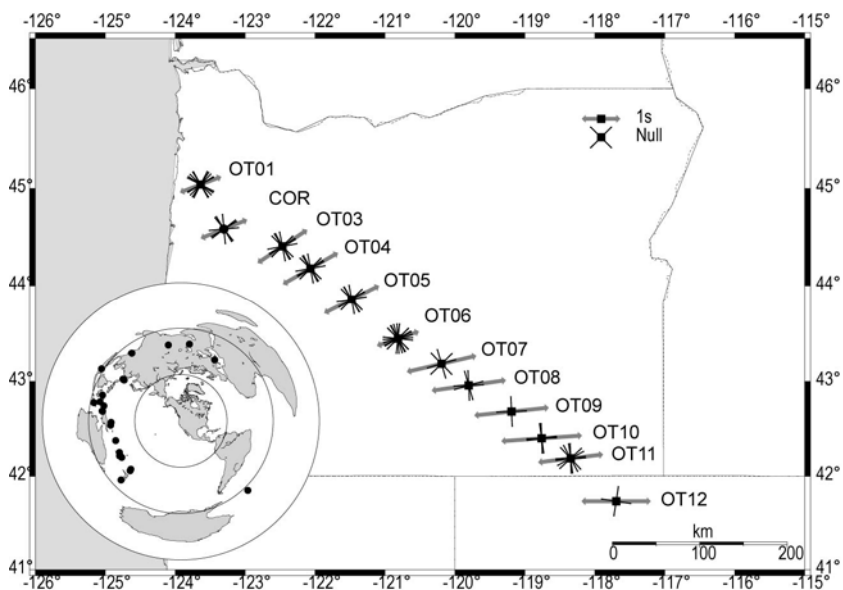


Fig. 3.2

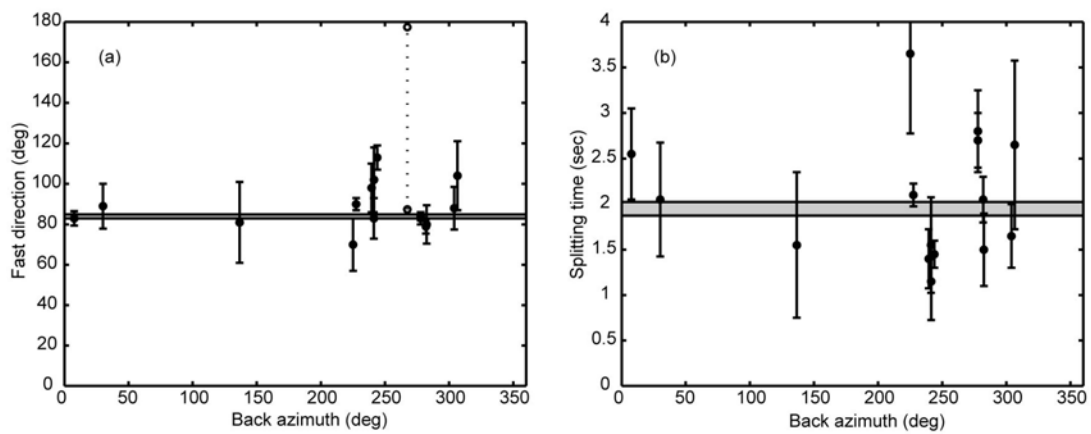


Fig. 3.3

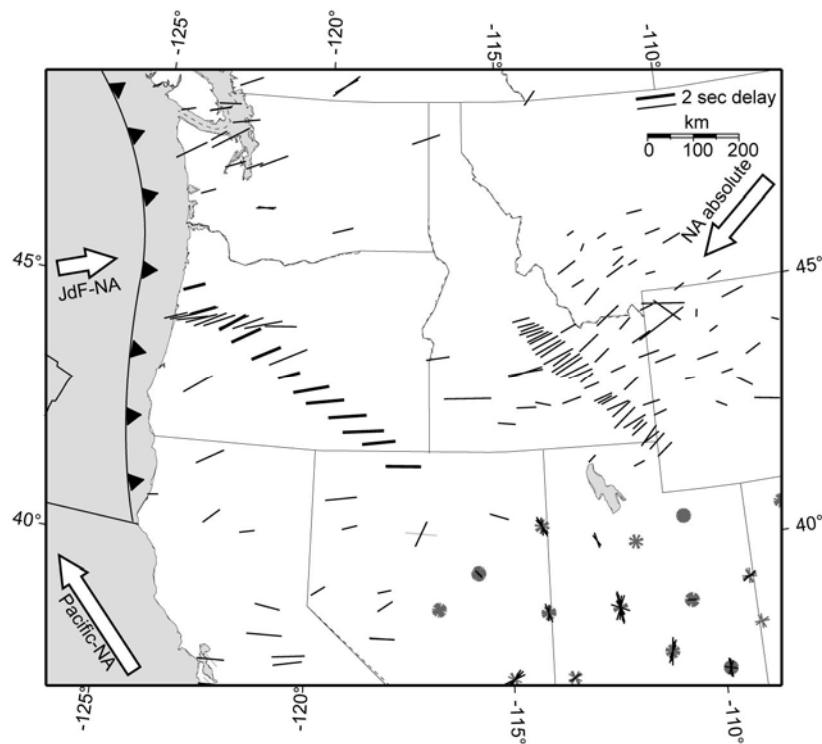


Fig. 3.4

Chapter 4

The Fate of the Juan de Fuca Plate

This chapter has been published in *Earth and Planetary Science Letters* with the title of “The Fate of the Juan de Fuca Plate: Implications for a Yellowstone Plume Head” [Xue and Allen, 2007].

Summary

Beneath the Pacific Northwest the Juan de Fuca plate, a remnant of the Farallon plate, continues subducting beneath the North American continent. To the east of the Cascadia subduction zone lies the Yellowstone hotspot track. The origins of this track can be traced back to the voluminous basaltic outpourings in the Columbia Plateau around 17 Ma. If these basalts are the result of a large melting anomaly rising through the mantle to the base of the North America continent, such as a mantle plume head, the anomaly would need to punch through the subducting Juan de Fuca slab. Here, we use teleseismic body wave traveltime tomography to investigate the fate of the subducted slab and its possible interaction with a plume head. Our dataset is derived from the Oregon Array for Teleseismic Study (OATS) deployment in Oregon and all other available seismic data in this region. We image the subducted Juan de Fuca plate in the mantle east of the Cascades beneath Oregon, where the slab has not been imaged before, to a depth of 400 km but no deeper. The slab dips $\sim 50^\circ\text{E}$ and has a thickness of ~ 75 km. Immediately

beneath the slab, we image a low velocity layer with a similar geometry to the slab and extending down to at least ~575 km depth in the V_S model. The total length of the high velocity slab is ~660 km, about 180 km longer than the estimated length of slab subducted since 17 Ma. Assuming similar slab geometry to today, this 180 km length of slab would reach ~60 km depth, comparable to the thickness of continental lithosphere. We propose that the absence of the slab below 400 km today is due to the arrival of the Yellowstone plume head ~17 Ma, which destroyed the Juan de Fuca slab at depths greater than the thickness of the continental lithosphere. Given this scenario, the low velocity anomaly beneath the slab is likely the remnant plume head material which has been pulled down by traction with the subducting plate. The amplitude of the observed low velocity anomaly is comparable with that expected for plume head material 100-300 °C hotter than the surrounding asthenosphere.

4.1 Introduction

In the Pacific Northwest, the Juan de Fuca plate is currently subducting beneath the northwestern United States and southwestern Canada (Fig. 4.1). Due to its proximity to the Juan de Fuca Ridge to the west, the Juan de Fuca plate being subducted is young ~10 Ma old [*Severinghaus and Atwater, 1990*] and thus thin and warm. The relative youth of the plate may be the cause of some of the unusual characteristics of this subduction zone. There is very little seismicity associated with the slab and a clear Wadati-Benioff zone of earthquakes is lacking compared to other subduction zones (e.g., [*Zhao, et al., 1995; Shelly, et al., 2006*]). The Juan de Fuca plate is a remnant of the Farallon plate. Around

30 Ma, when the ridge separating the Farallon and Pacific plates reached the North American plate, the Pacific and North American Plates began to interact [*Severinghaus and Atwater, 1990*]. The Farallon plate was split into two major sub-plates, and the Juan de Fuca plate is the central part of the northern sub-plate.

To the east of the Juan de Fuca subduction system are the Columbia River Basalts, the Yellowstone Hotspot Track and the High Lava Plains of Oregon, also referred as the Newberry Hotspot Track (Fig. 4.1). The Columbia River basalts extend throughout eastern Oregon, eastern Washington, and western Idaho, and are a series of flows with ages primarily 17-14 Ma (e.g., [*Christiansen, et al., 2002; Camp and Ross, 2004*]). The conduits for these flows lie along a NS-oriented trend, north of the McDermitt caldera (Chief Joseph Dike Swarm and Monument Swarm) and similar NS-oriented trends of magmatism occur southward at Steens Basalt dike and along the Northern Nevada rift zone (Fig. 4.1). The Newberry Hotspot Track, along the Oregon High Lava Plains, consists of a sequence of volcanic domes and lava flows. Isochrones of rhyolitic domes show a monotonic age progression from east to west ending at the Newberry Caldera (Fig. 4.1) [*Jordan, 2005*]. The Yellowstone Hotspot Track is associated with northeastward migration of silicic volcanism along the Eastern Snake River Plain ending at the Yellowstone Caldera) (e.g., [*Pierce and Morgan, 1992; Smith and Braile, 1994*]) (Fig. 4.1). The Newberry and Yellowstone tracks show age-progressive volcanism migrating away from a region near McDermitt Caldera which was first active around ~17 Ma. One interpretation for the voluminous basaltic outpourings of Columbia River Basalts, Steens Basalts, Chief Joseph Dike Swarm and Northern Nevada Rift Zone, and the formation of

the Yellowstone Hotspot Track is that a mantle plume impacted the North America lithosphere around 17 Ma. In this model, the tail of the plume is responsible for the Yellowstone track as the absolute plate motion of North American Plate is in a southwesterly direction. This is consistent with the associated gravity high, topographic high, high heat flow, and geochemical signature, which are characteristics of many hotspots. Yet, despite these features, evidence for an upwelling conduit through the upper mantle beneath Yellowstone remains unclear and the debate continues as to whether a mantle plume is the origin (e.g., [Humphreys, *et al.*, 2000; Jordan, *et al.*, 2004; Yuan and Dueker, 2005; Waite, *et al.*, 2006]). Given the proximity of the slab and the proposed Yellowstone Plume it is likely that the subduction and the upwelling processes interact with one another (e.g., [Geist and Richards, 1993; Pierce, *et al.*, 2000]).

A considerable amount of geophysical data illuminates the subducting Juan de Fuca plate west of the Cascades, e.g. controlled source reflection and refraction data offshore Washington and Oregon (e.g., [Trehu, *et al.*, 1995; Flueh, *et al.*, 1998]) and teleseismic scattered waves in northern Oregon [Bostock, *et al.*, 2002]. These studies provide clear evidence that the oceanic crust of the subducting Juan de Fuca plate is dipping at a few degrees with a steadily increasing dip to the east reaching $\sim 10^\circ$ beneath Coastal Ranges, and $\sim 30^\circ$ beneath Cascades. The andesitic volcanism of the Cascade Mountains also provides independent evidence for the presence of a slab. However, previous tomographic studies suggest that the slab is not ubiquitous at greater depths east of the Cascades. In the northernmost part, the slab has been imaged to depths of ~ 400 to 500 km beneath British Columbia with a dip averaging 50° to the northeast [Bostock and

VanDecar, 1995]. Beneath northern and central Washington, the slab has been imaged to a depth of ~300 to 400 km with a steeper dip of 60° to 65° to the east [*Rasmussen and Humphreys*, 1988; *Bostock and VanDecar*, 1995] or a shallower dip of 45° to the east-northeast [*Michaelson and Weaver*, 1986]. Further south beneath southern Washington and northern Oregon, the imaged slab extends to ~300 km depth dipping 60° to the east [*Michaelson and Weaver*, 1986]. However, further south beneath Oregon, the slab has only been imaged to a depth of ~150 km with an apparently vertical dip beneath the Cascades [*Rasmussen and Humphreys*, 1988]. At the southernmost part of the subduction zone beneath southern Oregon, the imaged slab extends down to a depth of ~200 km beneath the Cascade Range dipping ~65° to the east along a NW-SE array across southern Oregon [*Harris, et al.*, 1991].

Although the slab has been imaged to depths of ~300 to 400 km beneath Washington, there is little evidence for the presence of a slab in the mantle east of the Cascades beneath Oregon [*Michaelson and Weaver*, 1986; *Rasmussen and Humphreys*, 1988; *Harris, et al.*, 1991; *Bostock, et al.*, 2002]. The question, therefore, is does the Juan de Fuca slab extend down deeper into the mantle east of the Cascades beneath Oregon, or does it break up and disintegrate due to its young age or the passage of the proposed Yellowstone Plume? The apparent absence of the slab east of the Cascades has been interpreted as suggesting that (1) the slab has a small velocity contrast making the slab indistinct from the surrounding mantle [*Michaelson and Weaver*, 1986], (2) the slab has a vertical geometry [*Rasmussen and Humphreys*, 1988] or has broken off with a steep dip [*Michaelson and Weaver*, 1986; *Rasmussen and Humphreys*, 1988], or (3) a loss of

seismic resolution prevents imaging of the slab [*Rasmussen and Humphreys, 1988*]. Here, we present a new seismic tomographic model that answers these questions by mapping the Juan de Fuca slab into the mantle to a depth of ~ 400 km east of the Cascades beneath Oregon but no deeper.

4.2 Data and method

We use a dataset collected from the Oregon Array for Teleseismic Study (OATS) that was deployed in May 2003 and operated until May 2006. The OATS array includes eleven 3-component broadband seismic stations (Guralp CMG-3ESPD) with an average station spacing of 50 km. The permanent station COR at Corvallis represents a twelfth station. The OATS array extends northwest-southeast across Oregon from the coast to the McDermitt Caldera (Fig. 4.1). The dataset from OATS was complemented by data from 9 permanent networks and a temporary deployment as shown in Fig. 4.1. The nine permanent networks are the Berkeley Digital Seismograph Network (BDSN), Cascade Chain Volcano Monitoring (CC), Global Seismograph Network (GSN), Laser Interferometer Gravitational-Wave Experiment (LIGO), Princeton Earth Physics Project-Indiana (PEPP), Pacific Northwest Regional Seismic Network (PNSN), USArray Transportable Network (TA), University of Oregon Regional Network (UO), and the United States National Seismic Network (USNSN). The temporary deployment is the Wallowa Mountains Experiment. A total of 52 stations were used. The data from seismic events with epicentral distance greater than 30° and magnitude 6.0 and above from July 19th, 2003 to Nov. 10th, 2004 were inspected for all stations. For the S-velocity inversion,

a total of 95 events (Fig. 4.1) with clear S and SKS phases were recorded at 45 stations and a total of 2148 rays were used. For the P-velocity inversion, a total of 78 events with clear P and PKiKP phases were recorded at 46 stations and a total of 2101 rays were used. As the interference of phases at some epicentral distances can bias the relative arrival times determined using cross-correlation, such as P and PcP at $80^\circ - 90^\circ$, PKIKP and PKiKP at $120^\circ - 144^\circ$, we discarded most events which fall into above epicentral distances and only include events with clearly separated phases.

We follow a similar inversion procedure as described in [Allen, *et al.*, 2002a]. We manually check each waveform and pick either the first valley or the first peak. All the arrivals were picked by hand initially. The arrivals are then cross-correlated to obtain relative arrival times between all pairs of stations for each event [Vandecar and Crosson, 1990]. The average standard deviation of the relative traveltimes determined from cross-correlation is 0.05 sec for S and 0.02 sec for P. The average cross-correlation coefficient is 0.89 for S and 0.86 for P. Rather than reference relative arrival times to an absolute arrival time pick, we set the average relative arrival time of each event to zero. The consequence of this approach is the loss of absolute travel-time, preventing recovery of velocity anomalies common to all ray paths.

We analyzed the noise for OATS stations in December of 2003, and February, July, and October of 2004 and found that the noise peaks from 0.13 – 0.3 Hz. To avoid the possible influence of noise as well as observe the arrivals clearly, S and SKS arrivals were picked and cross-correlated in the frequency window of 0.02-0.1Hz; and P arrivals

were processed in the frequency window of 0.8-2.0 Hz. For cross-correlation, we chose a window length equal to approximately one wavelength or less for the arrivals observed in each frequency window, which is 10 sec for S and SKS and 1.25 sec for P and PKiKP respectively.

The dimension of the model space is $1000 \times 1000 \times 1000$ km, centered at 45°N and 119.375°W . The model grid spacing and the smoothing length are 25 km and 40 km respectively in all three directions. The region parameterized is more expansive than the volume in which we expect to resolve structure in order to ensure that anomalies are not compressed into the model box.

To account for the local structure beneath each station and accommodate any baseline shift between the relative travel-time sets for different events, station corrections and event corrections were included respectively in the inversion. For the S- and P-wave velocity models, a damping factor of 0.2 was used and a priori standard deviations of 3%, 0.6 sec, and 0.5 sec were used for the velocity nodes, station corrections, and event corrections respectively. Different values were tested and variations in these parameters of a factor of 2 or 3 had little effect on the inversion results. For S-wave velocity models, the initial RMS residual is 1.20 sec and after inversion, the RMS is reduced to 0.54 sec, a var reduction of 54%. For P-wave velocity models, after inversion, the RMS residual is reduced from the initial 0.57 sec to 0.30 sec and the var reduction is 46%.

4.3 Tomographic results and resolution tests

Here we present the vertical slices through our S- and P- wave velocity (V_s and V_p hereafter) models along the OATS array where both models have the highest resolution, as shown in Fig. 4.2a and b. The most prominent feature in our tomographic models is the high velocity anomaly which dips $\sim 46^\circ$ and extends down to a depth of ~ 400 km. We interpret this feature as the subducted Juan de Fuca plate. The cross-section is not perpendicular to the trench which is approximately north-south oriented. Instead the cross-section is rotated 28° clockwise from the trench-perpendicular direction. After correcting for the oblique trend of the cross section, the dip angle of the slab is 50° to the east.

The second prominent feature is the low velocity body beneath the slab in the V_s model, though this feature is not as evident in the V_p model. Other features observed are a low velocity anomaly beneath the Newberry volcano, and to its immediate SE a shallow high velocity anomaly. These features are visible in both V_s and V_p models, though their geometry differs a little in the two models.

The better ray coverage available from shear-wave arrivals means the V_s model has greater resolution than the V_p model. We therefore focus on the V_s model and present several resolution tests to assess the reliability of the prominent features. First, we conducted a checkerboard sensitivity test using alternating anomalies of high and low velocity evenly spaced throughout the model to a depth of 525 km in a 3D checkerboard pattern. Each anomaly has the geometry of a cylinder with a vertical axis and a dimension

of 100 km in both the vertical and horizontal directions. In the vertical direction, we put four alternating velocity anomalies centered at depths of 100, 225, 350, and 475 km respectively. Fig. 4.3a shows a vertical slice along the OATS array through the input model and Fig. 4.3b shows the recovered velocity anomalies. The size and shape of the anomalies are preserved well in the upper and middle sections of the model, i.e. in a triangular region beneath the OATS array. We recover two thirds of the input anomaly amplitudes. Outside the triangular region in the bottom corners of the model, the anomalies are smeared. All the velocity model features discussed in this paper are within the well-resolved triangular region.

Next we conducted realistic anomaly recovery tests on the observed slab feature as shown in Fig. 4.3c, d, e, and f. These tests explore how well our dataset can resolve a slab at different depths. At greater depth, the dip angle of all synthetic slab is 50° to the east, the same as imaged in this study. The shallow and nearly horizontal portion of the synthetic slab is based on the observed shallow slab structure in a previous study in northern Oregon [Bostock, *et al.*, 2002]. As demonstrated in the resolution tests, our dataset can not resolve the shallow nearly horizontal portion of the slab (Fig. 4.3d, e, and f). The reason is that we use teleseismic events for which rays have near vertical ray paths beneath stations. For horizontal structures near the Earth surface, the lengths of ray segments passing through such structures are almost identical and so are their contributions to traveltimes delays. As we use relative traveltimes, any common contributions would cancel out, making them difficult to image. Fig. 4.3c shows an input slab extending down to 400 km and the corresponding inversion result is shown in Fig.

4.3d. In this case, the recovered structure closely resembles the observed slab feature. In Fig. 4.3e, the synthetic slab extends down to only 300 km depth. The inversion result shows that a slab ending at 300 km depth does not smear significantly down dip and is not sufficient to produce the observed slab structure between 300 km and 400 km depth.

To test whether the slab extends to depths greater than 400 km, we conducted the test shown in Fig. 4.3f where the input slab extends down to 500 km depth. We conclude that the Juan de Fuca slab does not extend to depths greater than 400 km. This is because the recovered structure in our resolution test differs from the observed structure between 400 and 500 km depth in two aspects: (1) the recovered anomaly in the resolution test shows a strong velocity anomaly to 500 km depth while the observed anomaly does not extend to 500 km depth, (2) the transition of velocity anomaly from higher amplitudes to lower amplitudes along the length of the slab in the recovered structure is smooth along the length of the slab, unlike the step-like transition we observe in our model.

We also conducted realistic anomaly recovery tests on the observed low velocity body underneath the slab as shown in Fig. 4.3g and h. These tests explore if our dataset can resolve such a low velocity body and how well it can be resolved at different depths. We use the same geometry for the synthetic low velocity body as that for the slab. Fig. 4.3g shows the recovered velocity structure for a synthetic low velocity body extending down to 475 km depth. The geometry of the input anomaly is very well resolved with insignificant smearing essentially close to zero. For a low velocity body extending deeper to 575 km depth, our dataset also resolves the geometry well with only minor smearing

about 50 km along the slab as shown in Fig. 4.3h. However, the amplitude is only partially recovered in both cases. These tests demonstrate that our dataset is able to resolve this feature down to a depth of 575 km.

For a synthetic velocity structure consisting of a slab extending down to 400 km depth and a low velocity layer beneath the slab extending to 575 km depth (Fig. 4.3i), the locations and geometries of the recovered the high velocity slab and the low velocity body underneath (Fig. 4.3j) are very similar to what we observed (Fig. 4.2a) but with a reduced amplitude, about two thirds of what we observed. Based on our velocity model images and resolution tests, we propose that the true Earth structure consists of a slab extending down to ~ 400 km depth with a low velocity body beneath extending to at least 575 km depth. While we conclude that the high velocity slab does not extend deeper than ~ 400 km, the low velocity feature may extend deeper than 575 km.

4.4 Discussion

We interpret the high velocity anomaly dipping eastward into the mantle as the subducted Juan de Fuca plate. The observed velocity contrast is likely largely due to the temperature contrast between the slab and the surrounding mantle as temperature anomalies have a greater velocity signature than composition in the upper mantle [Goes, *et al.*, 2000]. The observed dip of 50° is similar to, but a little shallower, than other portions of the slab to the north and south of Oregon, where the slab dip has been

constrained as $\sim 60^\circ$ to 65° to the east [*Michaelson and Weaver, 1986; Rasmussen and Humphreys, 1988; Harris, et al., 1991*].

Though previous studies have speculated that the portion of the Juan de Fuca slab beneath Oregon might have a smaller velocity contrast than that to the north [*Michaelson and Weaver, 1986; Rasmussen and Humphreys, 1988*], the amplitude of the dipping high velocity anomalies are similar in our model beneath both Washington and Oregon (not shown). The maximum velocity contrast we observed for the slab below 100 km depth is 1.25% in the V_s model and 0.75% in the V_p model. These values are likely smaller than the real amplitudes as not all of the anomaly amplitude is recovered during the inversion due to smoothing, damping, and imperfect ray coverage. Our resolution tests show that, for a synthetic slab with 3% high velocity anomaly, the percentage of recovery under our inversion scheme is about $\sim 30\%$ for V_s and $\sim 40\%$ for V_p . Thus we expect that the true velocity anomaly associated with the slab is approximately 3 times stronger for V_s and 2.4 times stronger for V_p than what we recovered, i.e. around $\sim 3.8\%$ for V_s and 1.8% for V_p . When compared to the 3-4 % V_p anomalies observed in old subduction zones such as Tonga, Izu-Bonin, Japan, and Kuril subduction zones [*Deal and Nolet, 1999; Deal, et al., 1999*], the $\sim 2\%$ V_p anomaly we observed for the slab in central Oregon is low. This suggests that the Juan de Fuca plate is warm, likely due to its relatively young age ~ 10 Ma [*Severinghaus and Atwater, 1990*].

The amplitude of the high velocity anomaly is greatest immediately beneath the Cascades in both our V_s and V_p models (Fig. 4.2a and b). Resolution tests show that this

is unlikely to be an artifact of the inversion, indicating the presence of high velocities beneath the Cascades. As any contributions to the velocity models from the crust would be greatly reduced by station correction, the significant increase in high velocity anomalies implies the uppermost mantle has anomalously high velocity. This is likely the result of mantle melts leaving a depleted residuum behind.

Does the slab go deeper than 400 km depth? As the slab descends into the mantle, it is warmed and the surrounding mantle cools. The subduction rate of the Juan de Fuca plate ranges from 33 mm/yr to 41 mm/yr from northern California to central Washington [Gripp and Gordon, 2002]. For a 60° dipping slab with this rate of subduction the temperature anomaly of the slab would be between 200 and 400 °C colder than the surrounding mantle in a region 80 km wide at depths greater than 400 km (i.e. 8 Ma to 22 Ma since subduction) [Davies and Stevenson, 1992]. As every 100 °C decrease in temperature results in an increase of ~1% in the S-wave velocity [Cammarano, et al., 2003], we expect the slab at depths greater than 400 km to have high S-velocity anomalies of ~2% to 4% which should be easily resolved. This warming effect would also generate a gradual velocity contrast between the slab and the surrounding mantle. Instead, we see an abrupt end to the down-dip edge of the imaged slab (Fig. 4.2a and b). Resolution tests also indicate that we would image any slab to depth of ~600 km if it was present (Fig. 4.3d, e, and f). Thus if the slab is present at depths greater than 400 km, we would be able to resolve it. Therefore, we suggest that the slab ends at 400 km depth. Then the question becomes: what caused the abrupt end of the slab at 400 km depth given that there has been subduction in this region for last 150 million years.

It has been proposed that a mantle plume head impacted near the McDermitt Caldera and caused the initiation of broad volcanism throughout the region at ~17 Ma (e.g., [Draper, 1991; Pierce, *et al.*, 2000]). For such a plume to reach the base of the lithosphere it would have to punch through the subducting Juan de Fuca slab blocking the path of the plume to the surface. This would have created a lower edge to the subducted slab which would then continue to subduct deeper into the mantle for the last ~17 Ma. The subduction rate of the Juan de Fuca plate is estimated to be 33 mm/yr N58°E near the trench west of southern Oregon for the last ~6 Ma [Gripp and Gordon, 2002]. The east component of this subduction rate, perpendicular to the trench, is 28 mm/yr. As the average plate speed has remained fairly constant since 19 Ma [Wilson, 1988], we can use this value to estimate the amount of oceanic lithosphere subducted to the east since 17 Ma. The estimated total length of slab subducted to the east in the last 17 Ma is ~480 km. Using our imaged slab (Fig. 4.2a and b) we can measure the length of the observed slab from the present trench in an east-west direction. The total length of imaged slab is ~660 km. This means that at 17 Ma, the bottom edge of the slab we observe today would be at the end of a 180 km length of subducted slab. Assuming that the slab geometry was similar to today, the end of the slab we observe would be at ~60 km depth given the shallow dip of the slab from the trench to the Cascades. While the thickness of the North American lithosphere is uncertain, the 60 km depth of the end of the slab is likely comparable to the thickness of the lithosphere. Thus, the absence of the slab at greater depths could be explained by a plume head destroying a large portion of the Juan de Fuca

slab, potentially all of the slab at depths greater than the thickness of the continental lithosphere.

Unfortunately global and continental scale velocity models typically do not have the resolution to image structures on the scale of those discussed here (e.g., [Bijwaard, *et al.*, 1998; Grand, 2002; Marone and Romanowicz, 2007]). However, Van de Lee and Nolet [vanderLee and Nolet, 1997] imaged a high velocity anomaly above 400 km depth beneath Cascadia, but they do not image this high velocity anomaly extending down into the transition zone from 410 km to 660 km depth. This is in contrast to the clear evidence for the Farallon slab in the transition zone to the south of Cascadia where a continuous high velocity anomaly is observed from northern California to central America [vanderLee and Nolet, 1997]. While the resolution in Van der Lee and Nolet's model is poorer beneath Cascadia than other parts [Van der Lee, personal communication], their observations are consistent with our interpretation of a hole in the slab.

The low velocity body beneath the slab in our V_s model is a feature not commonly observed beneath subducting slabs. The amplitude of the low velocity anomaly is estimated to be ~3% when the damping and smoothing effects of the inversion are taken into account. Michaelson and Weaver [Michaelson and Weaver, 1986] also concluded that a low velocity feature was present in their models from Washington to northern Oregon. They introduced a low velocity layer beneath the high velocity slab to account for the large delays observed at stations on the Olympic Peninsula and Oregon Coast Range. The low velocity layer they introduced was 80 km thick with 2-3% slower

velocities beneath the dipping high velocity layer. This is very similar to what we observed here. Much broader low velocity zones beneath slabs have been observed in other subduction zones, such as in Tonga, Kuril, Japan, and the Izu region (e.g., [Deal and Nolet, 1999; Deal, et al., 1999; Hall and Spakman, 2002]). However, the low velocity zones observed in these studies are diffuse encompassing large regions, not only underneath the slabs but also above them. The low velocity zones above slabs are consistent with arc volcanism caused by partial melting of the crustal component of subducted slabs as well as convection processes related with back arc spreading [Zhao, et al., 1997; Deal and Nolet, 1999]. However, the cause of the diffuse low velocity zones beneath slabs remains enigmatic.

We propose that the low velocity material beneath the Juan de Fuca slab is the remnant plume head material that has been dragged down by the subducting slab for the last 17 Ma. The plume head is estimated to be 100-300 °C hotter than the surrounding asthenosphere [Hill, et al., 1992], and the time scale for cooling a plume head is of order hundreds of millions of years due to its thickness (100 to 200 km) [Hill, et al., 1992]. Thus the plume head material is expected to have a low velocity anomaly of 1 – 3%, comparable with the amplitude of the low velocity body we observed beneath the Juan de Fuca slab. Davies and Stevenson [Davies and Stevenson, 1992] showed that a subducting slab can drag mantle material beneath the slab down with it. An experimental convection study also shows the possibility that the plume head material can be dragged down with cold downwellings [Davaille, et al., submitted]. This high temperature low velocity body may also be partially responsible for some of the unusual characteristics of the Juan de

Fuca subduction zone. The absence of a Wadati-Benioff zone of earthquakes all along the Cascadia is particularly clear beneath Oregon, east of the McDermitt Caldera where the plume head is proposed to have impacted.

To summarize our interpretation, Fig. 4.4 shows a tectonic reconstruction of our proposed model for the evolution of subduction beneath western North America and the interaction of the slab with a plume. We build on tectonic models proposed by Geist and Richards [*Geist and Richards, 1993*] and Pierce, et al. [*Pierce, et al., 2000*]. When the rising plume head (Fig. 4.4a) reaches the base of the continuous Juan de Fuca slab it begins to spread laterally. Based on geometric considerations, the buoyant plume material would spread preferentially upwards and westwards along the base of the plate while traction with the subducting plate pulls some plume head material down (Fig. 4.4b). At ~17 Ma, the plume head had punched through the slab, breaking up much of the subducted oceanic lithosphere, and impacted the North American continent initiating the broad voluminous volcanism in the region (Fig. 4.4c). Part of the plume head would spread westward (Fig. 4.4d) possibly as far as the Juan de Fuca Ridge [*Hill, et al., 1992; Parsons, et al., 1994*]. The continuing subduction of the Juan de Fuca slab then drags the remnant plume head material down deeper into the mantle (Fig. 4.4e), resulting in the low velocity body imaged today (Fig. 4.4f). We note that the only direct evidence for a mantle plume head is the unusual low velocity layer beneath the slab today. This feature could be explained by any mechanism providing a large scale upwelling of high temperature material around 17 Ma. However, if such a plume head impacted the North

American lithosphere around this time, it would explain our observations of the Juan de Fuca plate.

4.5 Conclusions

We image the Juan de Fuca plate as a high velocity anomaly dipping into the mantle east of the Cascades beneath Oregon. The slab reaches ~ 400 km depth with a dip of $\sim 50^\circ$ to the east and a thickness of ~ 75 km. After taking into account damping, smoothing, and imperfect ray coverage in the inversion, the actual amplitude of the velocity anomaly associated with the slab is likely $\sim 3.8\%$ for V_s and 1.8% for V_p . Resolution tests show that we are able to resolve any slab to a depth of ~ 600 km where the slab is expected to have high S-wave velocity anomalies of $\sim 2\%$ to 4% . Thus the abrupt end to the slab at ~ 400 km in our tomographic images suggests that the slab stops at that depth. We also image a layer of low velocity immediately beneath the slab extending to a depth of at least 575 km. This layer has a similar geometry as the slab: a dip of $\sim 50^\circ$ E and a thickness of ~ 75 km. The amplitude of this low velocity anomaly is estimated to be up to $\sim 3\%$ for V_s . Resolution tests show that the low velocity layer is required by data and is not an artifact of the inversion.

Using the relative plate motion between the Juan de Fuca plate and the North America Plate (HS3-NUVEL1A), the estimated total length of the slab subducted to the east in the last 17 Ma is ~ 480 km. This is less than the total imaged slab length of ~ 660 km from the present trench in an east-west direction. Therefore, the bottom edge of the

slab we observe today was east of the trench around 17 Ma. Assuming similar slab geometry to today, the ~180 km length of slab would reach a depth of ~60 km, comparable to the likely thickness of the continental lithosphere. We propose that the absence of the slab below 400 km depth today is due to the arrival of the Yellowstone plume head around 17 Ma, which destroyed the Juan de Fuca slab at depths greater than the thickness of the continental lithosphere. As the plume head material would spread westward beyond the trench possibly as far as the Juan de Fuca Ridge, traction with the subducting plate would then pull some plume head material down into the mantle. We image this material as the low velocity layer beneath the slab in our V_s model. The observed low V_s anomaly of up to 3% is comparable with what expected for plume head material 100-300 °C hotter than the surrounding asthenosphere. Finally, this hot remnant plume head material beneath the slab would warm the slab and may therefore reduce its strength and the ability to generate earthquakes. This may be partly responsible for the absence of a Wadati-Benioff zone associated with the subduction of the Juan de Fuca plate.

Figure captions

Fig. 4.1 Tectonic map for the study region. Plate motions from HS3-NUVEL 1A are shown as black arrows [Gripp and Gordon, 2002]. Blue dotted lines show the depth contours of the Juan de Fuca slab [McCrory, *et al.*, 2006]. The thick black lines delineate the Cascade Range. Age contours of initial rhyolitic volcanism along the Newberry track are shown in 1 Ma increments extending to the Newberry Caldera (NC) [3]. Major

rhyolitic caldera centers along the Yellowstone track are shown with age in Ma extending to the Yellowstone Caldera (YC) [*Pierce and Morgan, 1992*]. Both tracks initiate in the region of the McDermitt Caldera (MC), which is shown as a red circle. The Columbia River Basalt is shown in blue (12 to 17 Ma) [*Christiansen, et al., 2002*]. Dike swarms associated with the 17 Ma basaltic outpourings are shown in gold [*Christiansen and Yeats, 1992; Camp and Ross, 2004*]: Chief Joseph Dike Swarm (CJDS), Monument Swarm (MS), Steens Basalt (SB), and Northern Nevada Rift Zone (NNRZ). The seismic stations used in this study are shown as triangles and squares with a total number of 52. Inset shows the distribution of the 95 events used in the inversion for the S-wave velocity model. The red square outlines the study region. The thick black line across OATS array indicates the location of the cross section shown in Fig. 4.2 and 4.3.

Fig. 4.2 Vertical slices through the (a) V_s and (b) V_p models along the OATS line indicated in Fig. 4.1. The envelope of the synthetic slab ending at 400 km depth as shown in Fig. 4.3 (c) is shown by the blue outline. The contour interval is 0.25% indicated by vertical lines in the color bar of the velocity scale. Zero contours are not shown. The locations of the Cascades and the Newberry Volcano are shown as blue and red triangles respectively.

Fig. 4.3 Resolution tests for the V_s velocity model. All slices are along the OATS line as in Fig. 4.2. (a) The input model of the checkerboard test and (b) the recovered model. (c) A synthetic slab ending at 400 km and (d) the recovered model. The recovered models for a slab ending at 300 km and 500 km depth are shown in (e) and (f) respectively. The

recovered model for a low velocity body to 475 km and 575 km depth are shown in (g) and (h) respectively. (i) The synthetic model with a slab ending at 400 km depth and a low velocity anomaly body underneath ending at 575 km depth and (j) the recovered model. The amplitude of the input Vs anomaly is 3%. Input models are overlain on the recovered models by thick lines with blue for high velocity anomaly and red for low velocity anomaly. The contour interval and color scale are the same as in Fig. 4.2.

Fig. 4.4 Proposed tectonic model for the interaction between the subducting Juan de Fuca Plate (blue) and the Yellowstone plume head (pink). Snapshots in time are shown as: (a) 25 Ma, the Yellowstone Plume is approaching the subducted Juan de Fuca plate; (b) 20 Ma, the plume head has intersected the Juan de Fuca plate and preferentially flowed westwards along the base of the slab; (c) at 17 Ma, the plume head has punched through the Juan de Fuca plate, destroyed a larger portion of the slab and caused the volcanism at the surface; (d) 15 Ma, the plume head material spreads out in a larger region at the base of the lithosphere; (e) 8 Ma, the subducting slab drags the remnant plume head material down into the mantle; (f) at present, the hot material from the remnant plume head has been brought to greater depth by the ongoing subducting slab. The vertical dashed line indicates the progression of the current Yellowstone caldera to the west. The red plume stem represents a hypothetical Yellowstone Plume since the arrival of the plume head (pink). Note: this model builds on the tectonic models proposed by Geist and Richards [Geist and Richards, 1993] and Pierce, et al. [Pierce, et al., 2000].

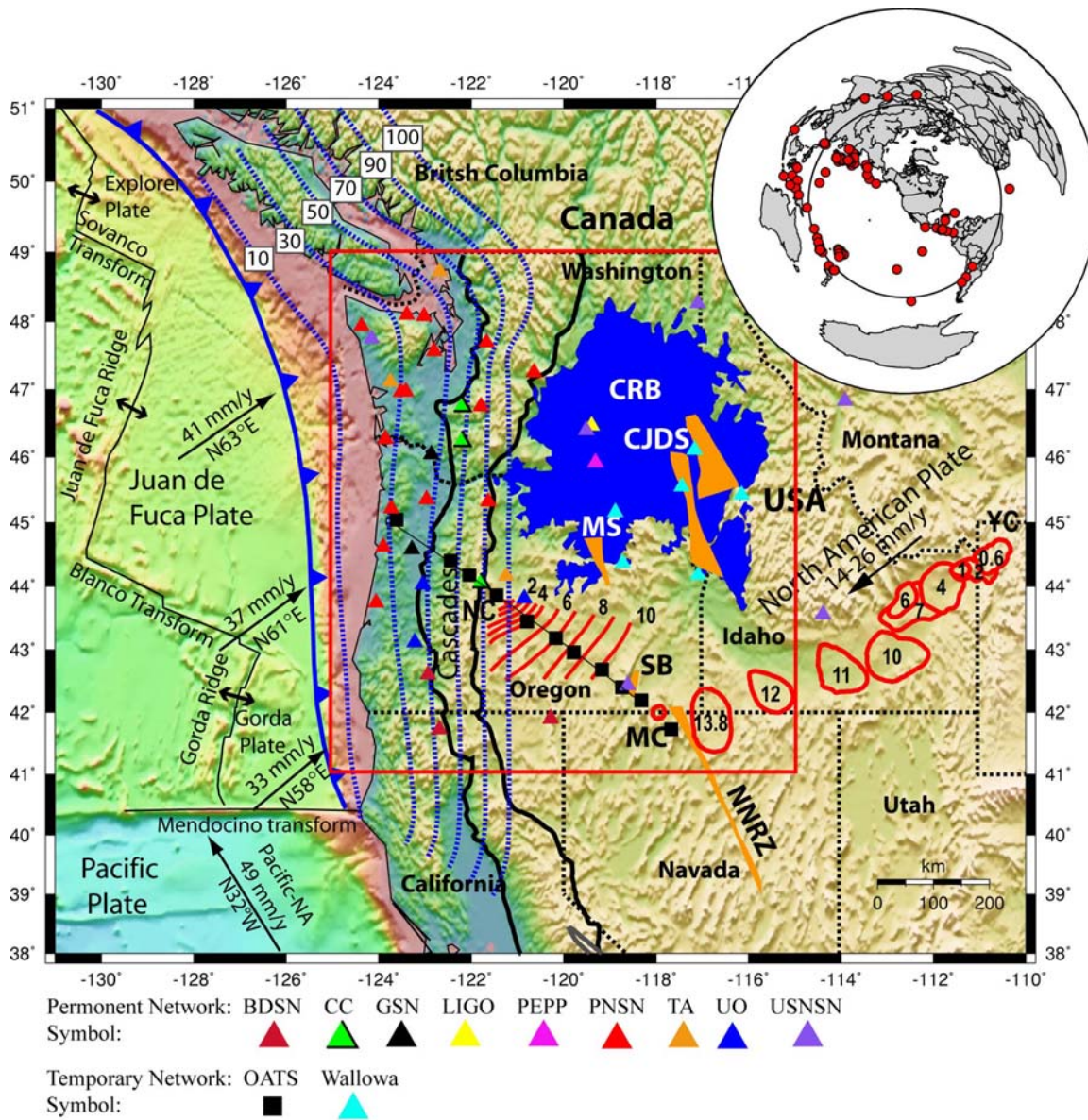


Fig. 4.1

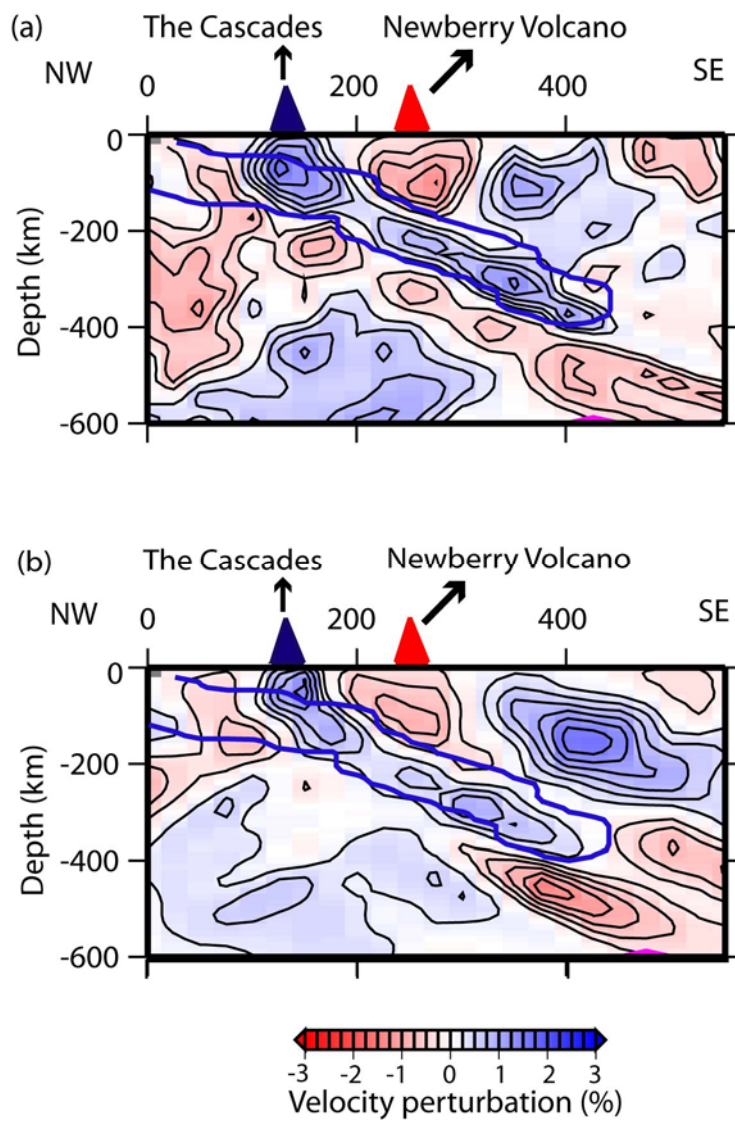


Fig. 4.2

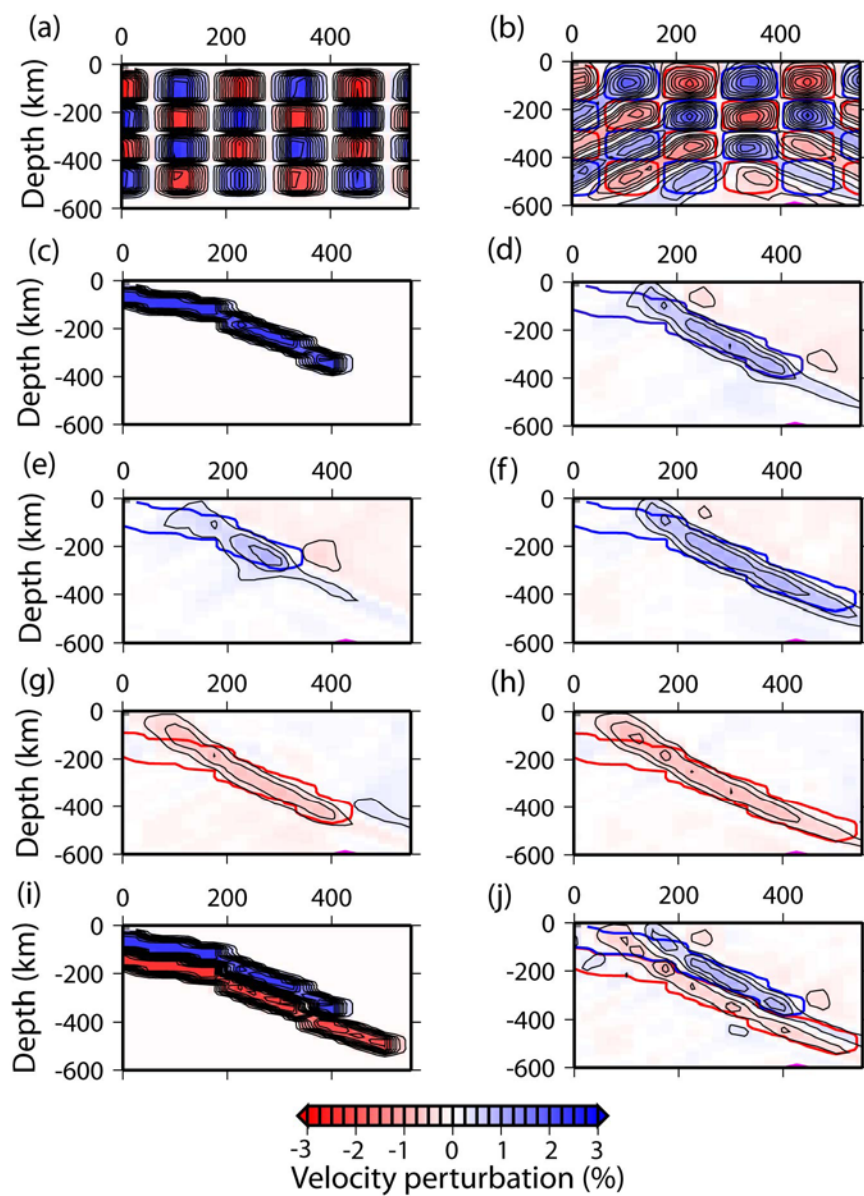


Fig. 4.3

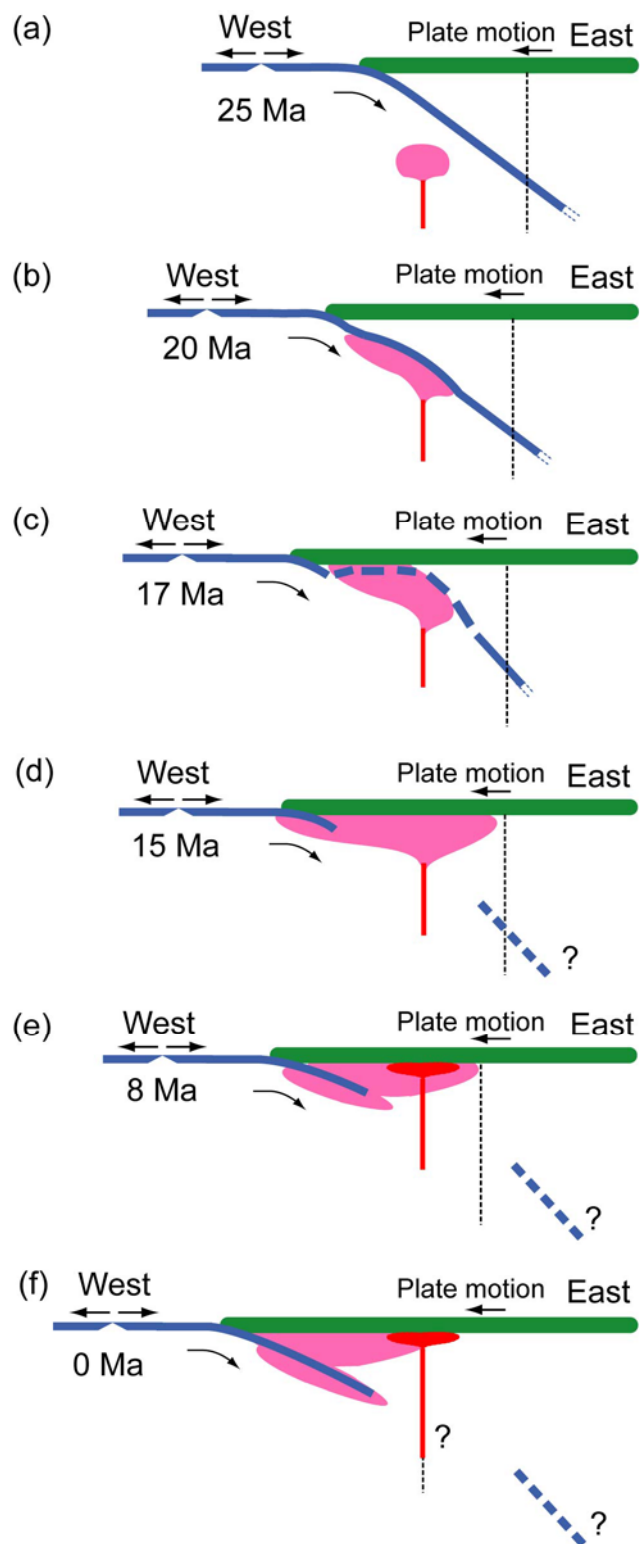


Fig. 4.4

Chapter 5

Western USA Mantle Structure and its Implications for Mantle Convection Processes

Summary

High resolution velocity models beneath western USA can provide important constraints on mantle convection processes in this tectonically active region, e.g., the subduction of the Juan de Fuca plate, the upwelling of the Yellowstone plume, and their possible interactions. In this study, we apply the tomography technique using data from the Earthscope Transportable Array and complemented by regional network data. This provides a total of 809 seismic stations for our analysis. To build our velocity models, we use 88 earthquakes for our S-model and 58 earthquakes for our P-model. We call our model the Dynamic North America model, and it is the first in a suite of models that we plan to develop as the Transportable Array moves across the North America continent. We therefore refer to the models presented here as DNA07. Our tomographic images show some common features which have been imaged before such as the high velocity anomaly beneath the Cascades and the low velocity anomaly beneath the Yellowstone National Park. However, the unprecedented aperture of the network and dense station distribution allows us to see deeper and reveals new features: (1) the imaged Juan de Fuca subduction system stops at ~ 400 km beneath Oregon, and is disrupted in Oregon, implying an interaction with the proposed Yellowstone plume; (2) the low velocity

anomaly beneath the Yellowstone park stops at 500 km and dips towards the northwest; (3) we do not detect a low velocity conduit reaching greater depth beneath Yellowstone, implying either there is no deep mantle plume, if there was a plume it was short-lived, or the conduit is smaller than 50 km or the velocity perturbation is less than 1.5% for S and 0.75% for P, and therefore beyond our resolution; (4) two low velocity zones are observed beneath the Eastern Snake River Plain: a shallow one to depths of 200 to 250 km and a deeper one at depths greater than 600 km. These two zones are separated by a high velocity zone; (5) low velocity anomalies shallower than 150 km depth are observed along the Newberry hotspot track indicating no deep asthenospheric low velocity anomaly beneath it; (6) immediately south of the Juan de Fuca subduction system, we image low velocity anomalies down to ~ 400 km depth, coincident with the proposed location of the slab gap; (7) we see the high velocity Pacific plate abutting against the low velocity North American plate across the San Andreas Fault System; (8) we image a fast velocity anomaly beneath northeast Oregon down to ~ 300 km depth, representing the depleted mantle after the eruption of the Columbia River flood basalts; (9) the Big Drip beneath Transverse Ranges and the high velocity body beneath the southern Central Valley/Sierra Nevada; (10) a high velocity anomaly beneath the central Basin & Range surrounded by low-velocity anomalies; (11) low velocity zone beneath the Coast Ranges and east of the Cascades from southern Washington to northern Nevada; (12) a strong north-south trending low velocity zone above the slab east of the Cascades from southern Washington to northern Nevada; (13) high velocity anomalies down to 250 to 300 km depth beneath the central Washington; (14) a low velocity anomaly beneath the Salton Trough. These observations reveal extremely heterogeneous mantle structure for the

western USA and suggest we are only just beginning to image the complex interactions between geologic objects beneath the western USA.

5.1 Introduction

Western USA is on the west margin of the North American plate and is a region that has complicated and active tectonics. The Juan de Fuca plate, the Pacific plate, and the North American plate meet in this region and formed the Mendocino triple junction just offshore northern California (Fig 5.1). North of the triple junction, the Juan de Fuca plate is subducting beneath the North American plate from the northwest. South of the triple junction is the strike-slip San Andreas Fault, the plate boundary between the Pacific and North American plates.

The Juan de Fuca plate is a remnant of the much larger Farallon plate. Around 30 Ma, when the ridge separating the Farallon and Pacific plates reached the North American plate, the Farallon plate was then split into two major sub-plates, separated by the San Andreas Fault, and the Juan de Fuca plate is the central part of the northern sub-plates with the Explorer plate to its north and the Gorda plate to its south [*Severinghaus and Atwater, 1990*]. In this paper, the Juan de Fuca plate represents all three plates. In previous studies, the slab has been imaged to depths of ~300 to 400 km beneath Washington but was absent in the mantle east of the Cascades beneath Oregon (e.g. [*Michaelson and Weaver, 1986; Rasmussen and Humphreys, 1988; Harris, et al., 1991; Bostock, et al., 2002*]). A recent seismic traveltime tomographic study focused in Oregon

imaged the Juan de Fuca slab to a depth of ~400 km in the mantle east of the Cascades beneath Oregon but no deeper [Xue and Allen, 2007], this model is named JdF07.

In addition to these primary tectonic objects, many other complicated geologic features are also observed in the western USA. The most prominent features are the voluminous volcanism that initiated around 16Ma to 17Ma: the Yellowstone hotspot track, the Columbia River Basalts, and the Newberry hotspot track (Fig. 5.1). The Yellowstone hotspot track is associated with northeastward migration of silicic volcanism along the Eastern Snake River Plain ending at the Yellowstone Caldera (e.g. [Pierce and Morgan, 1992; Smith and Braile, 1994]) (Fig. 5.1). The Columbia River basalts extend throughout eastern Oregon, eastern Washington, and western Idaho, and are a series of flows with ages primarily 17-14 Ma (e.g. [Christiansen, et al., 2002]). The Newberry hotspot track, along the Oregon High Lava Plains, consists of a sequence of volcanic rhyolitic domes showing a monotonic age progression trending northwest ending at the Newberry Caldera (Fig. 5.1) [Jordan, 2005]. Both the Newberry and Yellowstone tracks initiated from a region near the McDermitt Caldera around ~17 Ma.

The formation of the Yellowstone hotspot track has been proposed to be a mantle plume impacting the North American lithosphere around 17 Ma. This is consistent with the parabolic topography, high heat flow, and the elevated He^3/He^4 ratio, which are predicted characteristics of deep mantle plumes. Despite all of this, evidence for an upwelling conduit through the lower mantle beneath Yellowstone remains unclear and

the debate continues as to whether a mantle plume is the origin (e.g., [Humphreys, *et al.*, 2000; Jordan, *et al.*, 2004; Yuan and Dueker, 2005; Waite, *et al.*, 2006]).

The source of the Columbia River Basalts has also been attributed to the Yellowstone deep mantle plume (e.g., [Geist and Richards, 1993; Pierce, *et al.*, 2000]). However, an alternative causal mechanism which requires no deep mantle plume has also been proposed for the Columbia River flood basalts. [Hales, *et al.*, 2005] propose that delamination of the Wallowa plutonic roots could be responsible for the voluminous outpouring.

While some studies attributed the source of the Newberry hotspot track to be the Yellowstone plume (e.g. [Draper, 1991]), other studies use the northwest-propagating Newberry hotspot track to disfavor the Yellowstone plume hypothesis all together (e.g. [Christiansen, *et al.*, 2002]). Alternative causal mechanisms such as subduction counterflow, gravitational flow along lithospheric topography, and lithospheric processes would require no plume (e.g. [Smith, 1977; Draper, 1991; Humphreys, *et al.*, 2000; Pierce, *et al.*, 2000; Christiansen, *et al.*, 2002; Jordan, 2005]). Seismic anisotropy beneath the Newberry track suggests no flow along the length of the track implying that lithospheric processes are the most likely cause [Xue and Allen, 2006]. Therefore, the Newberry hotspot track itself cannot be used to argue for or against the Yellowstone Plume hypothesis.

Given the proximity of the slab and the proposed Yellowstone Plume it is likely that the subduction and the upwelling processes interact with one another (e.g., [*Geist and Richards, 1993; Pierce, et al., 2000*]). The JdF07 model imaged the subducted Juan de Fuca plate in the mantle east of the Cascades beneath Oregon but found it stops at a depth of 400 km. Xue and Allen (2007) propose that the absence of the slab below 400 km today is due to the arrival of the Yellowstone plume head at ~17 Ma, which destroyed the Juan de Fuca slab at depths greater than the thickness of the continental lithosphere.

In addition to these primary tectonic objects and volcanic processes described above, there are several other prominent geologic provinces in western USA shown in Fig 5.1. To the west is the Coastal??? Ranges, a mountain belt following the coastline from the Olympic Mountains of Washington south to the westernmost Transverse Ranges in southern California. Immediate east of the Oregon Coast Ranges is the Cascades extending from Okanogan Highlands in Washington south to the northern California Coast Ranges. The Cascades delineate the active volcanic arc related with the Juan de Fuca subduction system. The Sierra Nevada is an extension of the Cascades towards the south and ends just north of the Transverse Ranges. While the Cascades has a lithology of mainly extrusive Cenozoic volcanic rocks, the Sierra Nevada is mainly intrusive Mesozoic granitic rocks and therefore represents the roots of an ancient volcanic arc. Between the rugged mountains of the California Coastal Ranges and the Sierra Nevada lies the Central Valley (also known as the Great Valley) which is about 650 km long and 80 km in wide [*Harden, 1998*].

South of the California Coastal Ranges, Central Valley, and the Sierra Nevada lies the east-west trending Transverse Ranges, formed by the convergence of the Pacific and North American plates at the “Big Bend” in the San Andreas Fault (Fig 5.1). Located in southernmost California, the Salton Trough is a pull-apart basin bordered on the northeast by the San Andreas Fault and on the southwest by the San Jacinto Fault. South of the Salton Trough, beyond the margins of our study, rifting continues down the center of the Gulf of California.

East of the Sierra Nevada is the Basin and Range, extending from eastern California to central Utah, from southernmost Oregon and Idaho to southern Arizona, southwestern New Mexico and further south into the Sonoran State of Mexico. East the Basin and Range is the Colorado Plateau with the Wasatch Front on its north side, and the Rocky Mountain front on its east. These features are all marked in Fig. 5.1.

Here we image the mantle structure beneath these geologic terranes in an effort to understand their deep structure and origin. Previous surface wave studies resolved that on average, upper mantle S-wave velocities of western USA are considerably slower than that beneath the North American craton (e.g. [*van der Lee and Nolet, 1997; Marone and Romanowicz, 2007*]). Body wave traveltimes tomography studies have better lateral resolution of velocity features in the mantle beneath western USA (e.g. [*Dueker, et al., 2001*]) and show more detailed velocity features such as the high-velocity Juan de Fuca plate beneath the Cascades, the low-velocity anomalies beneath the Yellowstone and the

East Snake River plain, and the high-velocity anomaly beneath the Transverse Ranges of southern California etc.

In this study, we incorporated the Transportable array data with all other available networks resulting in an unprecedented dense distribution of stations in the western USA. This results in the best coverage for the region so far, which allows us not only to fill the gaps in the resolution of previous studies but also to see deeper into the mantle revealing new features. While previous velocity models derived from body wave traveltime tomographic studies are mostly P-wave velocity models, we developed both P- and S-wave velocity models for the western USA. We refer our seismic velocity models as DNA07-P for P-wave and DNA07-S for S-wave, where DNA07 represents the Dynamic North America model of 2007. The high resolution DNA07 models of the western USA reveal an extremely heterogeneous mantle structure and provide important clues to mantle convection processes in this tectonically active region and possible interactions between different geological objects, e.g., the subduction of the Juan de Fuca plate and the upwelling of the Yellowstone plume.

5.2 Data and method

5.2.1 Station distribution

We use a dataset collected from the Transportable Array, and complemented by data from 26 other available networks in the study region as shown in Fig. 5.2. The total of

stations is 809 and most are from the Transportable Array with an average station spacing of 70 km.

The 26 permanent networks are composed of the following networks: (1) 2 Global Seismograph Network: (IRIS/IDA and IRIS/USGS); (2) 5 Federal Digital Seismic Network: the Canadian National Seismograph Network (CNSN), GEOSCOPE (GEO), International Miscellaneous Stations (IMS), Leo Brady Network (LB), and the United States National Seismic Network (USNSN); (3) 14 regional networks: the ANZA Regional Network (ANZA), Berkeley Digital Seismograph Network (BDSN), Cascade Chain Volcano Monitoring (CC), Caltech Regional Seismic Network (CRSN), Montana Regional Seismic Network (MRSN), Northern California Seismic Network (NCSN), Western Great Basin/Eastern Sierra Nevada (WGB/ESN), Princeton Earth Physics Project-Indiana (PEPP), US Bureau of Reclamation Seismic Networks (USBR), Southern California Seismic Network TERRAscope (TERRA), University of Oregon Regional Network (UO), University of Utah Regional Network (UURN), Pacific Northwest Regional Seismic Network (PNSN), and the Yellowstone Wyoming Seismic (YWSN); (4) 3 temporary networks: the North Bay Seismic Experiment (NBSE), DELTA LEVY Northern California (DLNC), and the Wallowa TA 2006-2008 (WTA); and (5) 2 other networks: the Laser Interferometer Gravitational-Wave Experiment (LIGO) and the Network of Autonomously Recording Seismographs (NARS).

To invert for the DNA07-S model, 557 stations have been used. To invert for the DNA07-P model, 580 stations have been used.

5.2.2 Event distribution

We examined seismic events with epicentral distance greater than 30° and magnitude equal to or greater than 6.0 from January 1st, 2006 to October 13th, 2007. For events from May 19th, 2006 to March 31st, 2007, we examined all events at all stations; for events outside this time period, we only examined events which would improve the event back azimuth coverage.

We use both direct S and SKS phases to build the dataset for inverting the DNA07-S model. As direct S phases have higher signal to noise ratios on the tangential component than on the radial component, we use arrival data from tangential components for direct S phases. Similarly; for SKS phases, we use arrival data from radial components. We found 82 events providing useful S picks and 44 events providing useful SKS picks. To build the dataset for the DNA07-P model, we examined both direct P phases and core phases i.e. PKiKP. We found 75 events providing useful P picks and 6 events providing useful PKiKP picks.

Events are generally clustered in back azimuth from the northwest, west, southwest, and southeast. To reduce the data redundancy, when events are within 1° in epicenter distance as well as back azimuth, we only kept the event which has the highest signal to noise ratio and the largest number of picks. We removed 8 redundant events for SKS, 19 events for direct S and P phases, and 2 events for PKiKP phases. Concerned about

possible contamination of PKIKP to PKiKP, we removed the remaining 4 PKiKP events. Inversion results didn't change much with or without these 4 PKiKP events, probably due to the insignificant 713 rays for PKiKP, compared with the 15141 rays for P.

For the S-wave velocity inversion, DNA07-S, a total of 88 events are used with 36 providing clear SKS phases and 65 providing clear S phases. These phases are recorded by a total of 557 stations (Fig. 5.3), providing a total of 23233 rays with 8371 SKS rays and 14862 S rays. For the P-wave velocity model, DNA07-P, a total of 58 events are used with clear P phases recorded by 580 stations, resulting in a total of 15141 rays (Fig. 5.3).

5.2.3 Method

We follow the same inversion procedure as [Allen, *et al.*, 2002a]. We manually check each waveform for good signal to noise and manually pick either the first valley or the first peak. The arrivals are then cross-correlated to obtain relative arrival times between all pairs of stations for each event [Vandecar and Crosson, 1990]. The average standard deviation of the relative traveltimes determined from cross-correlation is 0.014 sec for S and 0.005 sec for P. The average cross-correlation coefficient is 0.91 for S and 0.89 for P. Rather than reference relative arrival times to an absolute arrival time pick, we set the average relative arrival time of each event to zero. Traveltime residuals are determined by calculating the relative arrival times at all stations for each event using the 1-D IASP91 model. The relative traveltime residue for each ray then is obtained by subtracting the predicted values using IASP91 from the observed relative arrival time. This approach has

the advantage of eliminating the uncertainties caused by the inaccurate locations of earthquakes as well as our incomplete knowledge about structures outside our study region. The consequence of this approach is the loss of absolute travel-time, preventing recovery of velocity anomalies common to all ray paths.

According to the noise analysis of data recorded by the Oregon Array for Teleseismic Study [*Xue and Allen, 2007*], we expect noise to peak at the frequency range of 0.13 – 0.3 Hz. To avoid the possible influence of noise, S and SKS arrivals were picked and cross-correlated in the frequency window of 0.02-0.1Hz; and P arrivals were processed in the frequency window of 0.8-2.0 Hz. For cross-correlation, we chose a window length equal to approximately one wavelength or less for the arrivals observed in each frequency window, which is about 8 sec for S and SKS phases and 1 sec for P phases.

The dimension of the model space is $5000 \times 5000 \times 2500$ km with the vertical dimension being 2500 km and centered at 40°N and 115°W . The model grid spacing and the smoothing length are 50 km and 100 km respectively in all three directions. The region parameterized is more expansive than the volume in which we expect to resolve structure in order to ensure that anomalies are not compressed into the model box.

5.2.4 Event correction and station correction

To account for any baseline shift between the relative travel-time sets for different events, event corrections were included in the inversion as a set of free parameters. To

get more accurate images of the mantle, we also need to correct for crustal effects. There are two approaches to correct and reduce the effect of crustal contamination on the images of the mantle. One approach is to use station correction where we consider the crustal structure to be unknown and we include a station correction in the inversion with the goal of removing the crustal traveltime delays from the mantle velocity model. Alternatively a crustal correction could be calculated using existing crustal models to remove the crust effect.

There is currently no crustal model covering the study region with a lateral resolution comparable to the stations spacing used in this study. Therefore, we use station corrections in order to correct for the true crustal structure. Rather than leave the station corrections unconstrained in the inversion, we use corrections calculated from the CRUST2.0 crustal model as a reference. CRUST2.0 is a global model of crustal structure, topography, and bathymetry with a resolution of 2° [Bassin, *et al.*, 2000] and can be found online at <http://mahi.ucsd.edu/Gabi/rem.html>. Individual ray parameters were used to compute the ray paths and traveltimes through CRUST2.0 using bicubic interpolation and taking into account station elevations. The resulting distribution of CRUST2.0 crustal corrections for the stations used in our study has a standard deviation of 0.50 sec for S-wave velocity and 0.27 sec for P-wave velocity. We assume that the distribution of CRUST2.0 crustal corrections represents the distribution of the true crustal corrections and we weight the station corrections in our inversion to have the same standard deviation as the CRUST2.0 correction. This allows us to use CRUST2.0 as a guide to the amplitude of true crustal corrections while letting our dataset adjust the individual

correction at each station. Fig. 5.4 shows maps of station corrections for the DNA07-S and DNA07-P.

For the DNA07-S model, a priori standard deviations of 6%, 0.39 sec, and 0.32 sec were used for the velocity nodes, station corrections, and event corrections respectively. Similarly, for the DNA07-P model, a priori standard deviations of 3%, 0.28 sec, and 0.16 sec were used for the velocity nodes, station corrections, and event corrections respectively. For both the DNA07-S and -P models, a damping factor of 0.1 was used in the inversion. The choice of these parameters effects the apparent velocity structure in the upper ~300 km as traveltimes delays are preferentially satisfied by station corrections or velocity anomalies in the uppermost mantle. Different values were tested and variations in these parameters of a factor of 2 or 3 had little effect on the amplitude of structure or velocity anomalies below ~300 km depth.

For the DNA07-S model, the initial RMS residual is 1.83 sec and after inversion, the RMS is reduced to 0.49 sec, corresponding to a variance reduction of 73%. For the DNA07-P model, after inversion, the RMS residual is reduced from the initial 0.60 sec to 0.15 sec and the var reduction is 74%.

5.3 Checker-board resolution tests

To demonstrate the resolution of our model in general, we conducted several 3-D checkerboard sensitivity tests using alternating anomalies of high and low velocity evenly spaced throughout the model.

First, we conducted a 3-D test with a length scale of 250 km. Each anomaly has the geometry of a cylinder with a vertical axis and a dimension of 250 km in both the vertical and horizontal directions. In the vertical direction, we put four layers of alternating velocity anomalies centered at depths of 125, 375, 625, and 875 km. Fig. 5.5 shows the results for the DNA07-S model. Fig. 5.5a and c are two depth slices of the recovered model through the center of two of the input layers, showing the size and shape of the anomalies are recovered very well except along the eastern and southwestern margins of the model where the resolution is reduced as shown on the ray density plots. The recovered amplitudes are reduced with increasing depth. Fig. 5.5b is a depth slice through the boundary of two of the input layers, showing that vertical smearing is insignificant. Fig. 5.5d and f are two vertical slices of the recovered model sliced into the center of the input velocity anomalies. They also show that size and shape of the anomalies are well recovered to a depth of 750 km although the recovered amplitudes are reduced at greater depth especially on the east margin. Fig. 5.5e is a vertical slice through the boundary of two of the input columns, showing that horizontal smearing is insignificant. Fig. 5.6 shows the results of the same resolution test for the DNA07-P model. The results demonstrate similar resolution as for the DNA07-S, although there is increased smearing in both the vertical and horizontal smearing directions. This is likely due to the lack of near-vertical core phases in the P-model.

As good resolution of small-scale structures does not demonstrate that larger structures can also be retrieved [Leveque, *et al.*, 1993], we conducted 3D checker-board tests for larger cell sizes of 500 km and 1000 km. Both tests demonstrate that our dataset can retrieve larger structures just as well as the 250 km anomalies. Fig. 5.7 and Fig. 5.8 show the results for 500 km anomalies for DNA07-S and -P respectively.

In the above synthetic tests and other synthetic tests to follow, we add Gaussian white noise in the synthetic relative traveltimes. In order to have a better representation of actual noise in data, we used the standard deviation of each relative traveltimes as the reference standard deviation when randomly generating noise for a data point. This results in a peak to peak noise of 0.2 sec for the P traveltimes data and 0.6 sec for the S traveltimes data.

5.4 Tomographic results and interpretations

Of the two velocity models (P- and S-velocity), DNA07-S has better event back azimuth coverage, better ray incident angle coverage, and a larger number of events and therefore rays, than DNA07-P (Fig. 5.3). DNA07-S therefore has better resolution as demonstrated in the checker-board tests (Fig. 5.5 to Fig. 5.8). Despite these differences in resolution, the main geologic features in the model region, e.g. the subducted Juan de Fuca plate and the Yellowstone upwelling, are clearly imaged in both models though the detailed geometry sometimes differs. Multiple, regular slices through DNA07-S and -P

are shown in Fig. 5.9 and Fig. 5.10. Fig. 5.9 plots depth slices from 100 km depth to 800 km depth with an interval of 100 km and Fig. 5.10 plots vertical slices corresponding to east-west cross-sections from northern Washington to southern California. The main features observed in the DNA07-S and -P models are described in the following sections

The synthetic tests in section 5.3 demonstrated that our dataset has good resolution and can retrieve features as large as 500 to 1000 km across or as small as 250 km across. In addition, we conducted another 3D checker-board test with a cell size of 200 km along the same vertical slices as are shown in Fig. 5.10. The results of this test are shown in Fig. 5.11, and helps identification of features from the models (Fig. 5.10) which fall into a region of good resolution and are therefore worthy of interpretation. In addition to the resolution tests, all velocity slices also have a corresponding ray density plot immediately to the left side of the velocity slice. White indicates zero hits and black indicates 100+ hits.

5.4.1 The Juan de Fuca subduction system

The Juan de Fuca subduction system can be observed as a zone of high velocity anomaly parallel to the plate margin and beneath the Cascades at 100 km depth and then migrates towards the east with increasing depth (Fig. 5.9). At 200 km depth, the slab seems weakened in northern Oregon; at 300 km depth, the slab is weakened in Oregon and the weakening is more obvious in the DNA07-P model; at 400 km depth, a coherent linear slab pattern is absent in DNA07-S model and the Oregon segment of the slab is

absent in DNA07-P model. At greater depths, a coherent slab feature is absent. Note that this region is one of relatively high ray density.

In vertical slices (Fig. 5.10), the slab shows up as a dipping high velocity anomaly reaching 400 km depth in Washington (B-B'), is weakened and disrupted in Oregon (C-C', D-D', E-E'), and shows up as a coherent slab feature again in DNA07-S and a strong slab feature in DNA07-P beneath northern California (F-F' and G-G'). An interesting feature is observed in northern California (F-F') and south of the Mendocino triple junction (G-G'), particularly in DNA07-P, where a dipping high velocity anomaly is imaged at depths greater than 400 km. This high velocity anomaly has a similar dip as the Juan de Fuca slab and is perhaps a segmented slab associated with the Cascadia subduction. In the disrupted slab section beneath Oregon (C-C', D-D', E-E', particularly in the DNA07-S) the weak slab segment seems to overlay another, deeper slab segment. A tentative explanation is that the deeper slab segment may be a previously broken-off slab which then sank, and continues to sink, due to its negative buoyancy. We also observe a low velocity zone immediately beneath the Juan de Fuca slab in the DNA07 models from central Oregon to northern California (Fig. 5.10 from E-E' to G-G'). This was previously observed in the JdF07 model and interpreted as remnant plume head material [*Xue and Allen, 2007*].

Previous studies suggest that the slab has a dip of 60° to 65° to the east [*Rasmussen and Humphreys, 1988; Bostock and VanDecar, 1995*] or a shallower dip of 45° to the east-northeast [*Michaelson and Weaver, 1986*] beneath northern and central Washington,

a dip of 60° to the east beneath southern Washington and northern Oregon [Michaelson and Weaver, 1986], a dip of 50° [Xue and Allen, 2007] or a vertical dip [Rasmussen and Humphreys, 1988] beneath the Oregon Cascades, and a dip of $\sim 65^\circ$ to the east along a NW-SE array across southern Oregon [Harris, *et al.*, 1991]. In our single model covering the length of Cascadia we image a nearly constant slab dip of $\sim 60^\circ$, which does not vary much from Washington through northern California.

The Juan de Fuca subduction system as described above is in a region away from the edge of the model and we therefore have good resolution as shown in Fig. 5.11. To further illustrate this we conducted realistic anomaly recovery tests on the observed slab feature as shown in Fig. 5.12. This test explores how well our dataset can resolve a slab-like anomaly at different depths. We use a synthetic slab anomaly with a dip of 50° to the east below 100 km depth and a nearly horizontal synthetic slab above 100 km based on the previously observed shallow slab structure in northern Oregon [Bostock, *et al.*, 2002]. We conducted two tests, a synthetic slab ending at 400 km and a slab ending at 600 km (Fig. 5.12). The results of the synthetic resolution tests shown in Fig 5.12 are sliced long the same cross-sections as the DNA07-S and -P in Fig. 5.10. The tests show that (1) we can recover the geometry of the slab with insignificant smearing for the DNA07-S and with minor smearing for the DNA07-P, and (2) slab recovery is very similar in the different cross-sections from Washington to northern California. Therefore, the observed disruption of the slab beneath Oregon is most likely real, and the slab, at least in this narrow clearly defined form, stops at about 400 km depth.

The DNA07 observation that the slab stops at 400 km is consistent with the preliminary contention of the JdF07 model [*Xue and Allen, 2007*] and also *Xue and Allen's* interpretation that the Juan de Fuca subduction system interacted with a Yellowstone plume head around 17 Ma. The additional disruption of the slab in Oregon at shallower depths may indicate that Oregon is the impact location of the Yellowstone plume head with the subducting Juan de Fuca slab. It also explains the absence of deep seismicity in Oregon.

5.4.2 The Yellowstone upwelling and the East Snake River Plain

In depth slices (Fig. 5.9), DNA07-P shows a strong low velocity anomaly beneath the Yellowstone region that extends down to 200 km depth. At 300, 400, and 500 km depth, no low velocity anomaly is observed directly beneath Yellowstone. Instead, a low velocity anomaly shows up northwest of Yellowstone (Fig. 5.9). This anomaly is much weaker in DNA07-S except at 100 km depth, where a strong low velocity anomaly is observed directly beneath Yellowstone. At 600 km, a low velocity anomaly is present in DNA07-S and this feature migrates towards the southwest and is still prominent at 800 km depth where it is also observed in DNA07-P. Fig. 5.13a is a NW-SE cross-section through the Yellowstone anomaly showing that a strong low velocity anomaly is located beneath the Yellowstone Caldera to a depth of 200 km and then dips towards the northwest. This anomaly stops at 500 km depth and its amplitude is reduced greatly at depths greater than 200 km in DNA07-S while it remains strong in DNA07-P.

To check whether the dip of the low velocity anomaly beneath Yellowstone towards the northwest is caused by smearing along rays coming from this back azimuth, we conducted a resolution test. In the test, we put a synthetic anomaly beneath the Yellowstone Caldera which extends down to 250 km, and test whether there is smearing towards the northwest with increasing depth. As shown in Fig. 5.13b, our dataset can recover the geometry of this anomaly with little smearing. This demonstrates that the northwest migration of the Yellowstone anomaly with depth is not caused by smearing and most likely a real feature. The observation of such a dipping low-velocity feature is consistent with previous tomographic studies (e.g. [Christiansen, *et al.*, 2002; Yuan and Dueker, 2005; Waite, *et al.*, 2006]).

Along the East Snake River Plain, low velocity anomalies are observed to 200-250 km depth in both DNA07-S and -P and are flanked by high velocity anomalies at 100 km (Fig. 5.9, Fig. 5.10 E-E', and Fig. 5.13 a and c). This has been observed before and has been interpreted as partially molten mantle (of low seismic velocity) beneath the hotspot track and basalt-depleted mantle (of high velocity) beneath the rest of the swell [Humphreys, *et al.*, 2000]. At much greater depths, greater than 600 km, a strong low velocity anomaly is clearly visible in DNA07-S and also observed in DNA07-P but with reduced amplitude (Fig 5.13c). There is no evidence for low-velocity anomaly connecting this lower mantle feature with the shallow anomaly beneath the Yellowstone Caldera. In fact there is a (weak) high velocity zone separating the shallower (<250 km) and deep (600-1000km) low velocity features (Fig. 5.13c).

The suggestion that the present Yellowstone melting anomaly is connected to a deeper mantle source in the transition zone to the northwest of Yellowstone is consistent with the topography of the 410 and 660 mantle discontinuities in this region. *Fee and Dueker (2004)* found that the “410” mantle discontinuity is deeper than 410 km in a circular region northwest of the Yellowstone caldera which is consistent with higher mantle temperatures in the region as would be expected for a mantle upwelling. However, *Fee and Dueker (2004)* did not find a shallow 660 km discontinuity in the same region suggesting that the same high temperatures are not present at 660km depth. Accordingly, *Fee and Dueker (2004)* argue for the presence of a warm upwelling at the 410 anomaly northwest of the Yellowstone caldera but that the anomaly does not extend across the 660 mantle discontinuity [*Fee and Dueker, 2004*]. Our tomographic observations are consistent with this observation.

While we do not image a plume conduit down into the lower mantle, the resolution limit of our model may prevent us from seeing a conduit if the conduit is too narrow. We therefore conducted several tests to determine the resolution limit. We put a low velocity anomaly beneath the Yellowstone caldera representing a mantle plume. The input anomaly has a radius of 50 km and extends from 0 to 1000 km depth with a -3 % velocity perturbation for S and -1.5 % for P (Fig. 5.14a and c). The recovered models are shown in Fig 5.14 b and d, and demonstrate that our dataset can recover the geometry of the input anomaly but with reduced amplitude at greater depths. We conducted two additional tests. First, we keep the same -3% and -1.5% velocity perturbations but reduce the conduit radius to 25 km. Second, we use a 50 km radius but reduce the velocity

perturbations by 50% to -1.5% and -0.75% for S- and P-velocity respectively. In both cases, we are not able to recover the input model (not shown). Thus if the conduit is smaller than 50 km in diameter or the velocity perturbation is small, i.e. less than 1.5% for S-velocity and 0.75% for P-velocity, our dataset will not be able to detect it.

5.4.3 The Newberry track/High Lava Plains

Small amplitude low velocity anomalies beneath the High Lava Plains and along the Newberry track are observed in the 100 km depth slice but do not extend to the 200 km depth slice (Fig. 5.9). The vertical cross-section of E-E' in Fig. 5.10 shows the low velocity anomalies are shallower than 150 km and have no further continuation deeper into mantle. The largest low-velocity anomaly is directly beneath the Newberry Caldera (at 350km on E-E', Fig 5.10) and is offset to the east of the High Cascades volcanic chain. Just as beneath the Yellowstone hotspot track, lower amplitude low-velocity anomalies are imaged along the track to the northwest (compare Fig 5.10 E-E' with Fig 5.13c). While shear-wave splitting observations suggest flow along the length of the Yellowstone track (e.g. [Waite, *et al.*, 2005]), shear-wave splitting results along the Newberry track do not align with flow along the volcanic progression [Xue and Allen, 2006]. The seismic anisotropy study led Xue and Allen [2006] to conclude that the Newberry hotspot track is not a product of asthenospheric flow, and is more likely a result of lithospheric processes. If this is the case, the low velocities observed in our tomography models may be generated by the melting anomaly.

5.4.4 High velocities beneath eastern Washington, northeastern Oregon and northern Idaho

A high velocity zone is observed from 100 to 300 km depth beneath central Washington and extends through northern Idaho reaching the northwest of Montana (Fig. 5.9). At shallow depths, e.g. 100 km, the high velocity zone connects with the high velocity slab (beneath the Cascades at 100 km) and the high velocity anomaly beneath the northeast Oregon. In the vertical cross-section through central Washington (Fig. 5.10 A-A'), this high velocity zone extends down to 250 to 300 km depth. Beneath northeast Oregon, the Wallowa Mountains, a high velocity anomaly is observed extending to ~400 km depth (Fig. 5.9, Fig. 5.10 C-C' and D-D').

Previously imaged high velocity anomalies beneath Washington have been interpreted as thick lithosphere or melt extraction (e.g. [Humphreys and Dueker, 1994b] and see references therein). The location of this high velocity zone corresponds with the margin of the North American craton as delineated by the $\text{Sr}^{87}/\text{Sr}^{86} > 0.706$ line [Ernst, 1988] (Fig. 5.1).

Hales, et al. (2005) imaged a high velocity anomaly to 175 km depth beneath the Wallowa Mountains. They hypothesized that it is depleted mantle remaining after the eruption of the Columbia River flood basalts which were in turn the result of delamination of the Wallowa plutonic root. This proposes an alternative causal mechanism for the eruption of the Columbia River Basalts, which would not require a

mantle plume. Yet, it is still unknown whether this mechanism can explain geochemistry observations such as the elevated He^3/He^4 ratios and an inclusion of oceanic crust in the source for the Columbia River Basalts. However, plume or no plume, the melt extraction due to the eruption of the Columbia River Basalts can generate high velocity anomalies in the mantle beneath it and therefore explains our observed velocity anomalies.

Beneath this broad shallow high velocity zone, other high velocity anomalies are observed at greater depths (particularly A-A' and B-B' in Fig 5.10). These are resolved features and illustrate the complexity of upper mantle structure. They may be previously subducted slab segments and/or delaminated craton roots.

5.4.5 High velocities beneath southern Sierra Nevada and Transverse Ranges

A high velocity anomaly is imaged at the southern tip of the Central Valley/Sierra Nevada (Fig. 5.9). In a region of good resolution, this feature shows up with a similar geometry in DNA07-S and -P: from the surface to 200 km depth this anomaly remains nearly vertical and then dips about 45° east ending at 400 km depth east of the southern Sierra Nevada tip (Fig. 5.10 J-J'). This feature has been previously imaged to a depth of 200 to 300 km and has been associated with an abandoned slab and/or lithospheric downwelling, or the eclogitic root of the Sierra batholith [*Humphreys and Dueker, 1994b; Ducea, 2001*].

Beneath the Transverse Ranges a high velocity anomaly is imaged to a depth of 200 km (Fig. 5.9). This anomaly dips 45° towards the east along the east-west cross-section in DNA07-S but is weaker in DNA07-P (Fig. 5.10 K-K'). The geometry of the feature beneath the Transverse Ranges is similar to that beneath the southern Sierra Nevada, particularly in DNA07-S (compare Fig 5.10 J-J' and K-K'). Similar features have been revealed before in P-wave velocity models beneath the Transverse Ranges and been interpreted as downgoing subcrustal lithosphere resulting from the convergence of the Pacific and North American plates [Humphreys, *et al.*, 1984; Humphreys and Hager, 1990].

In the cross-section through this anomaly along the trend of the Transverse Ranges (Fig. 5.15a), a similar velocity structure is observed as that along the K-K' in Fig. 5.10. In DNA07-S, the high velocity anomaly is strong and dips 45° towards the east reaching 300 km depth. In addition, a low velocity zone is imaged with a similar dip of 45° immediately beneath the high velocity anomaly. In DNA07-P, the high velocity anomaly is weaker and reaches a depth of 200 km without any apparent dip and there is only a weak low velocity anomaly beneath. When the anomaly is sliced perpendicular to the trend of the Transverse Ranges (Fig. 5.15b), the high velocity anomaly has a nearly vertical geometry in both S- and P- models reaching 200 km depth. A low velocity zone beneath the high velocity feature is observed again in the DNA07-S model but absent in the DNA07-P model.

The DNA07 models allow us, for the first time, to image the Transverse Ranges and the southern Sierra Nevada with a similar resolution to the Juan de Fuca subduction system to the north. Comparison of these southern Californian anomalies with the currently subducting slab shows remarkable similarity; compare Fig 5.10 C-C' or F-F' with J-J' and K-K'. Given this similarity, the simplest interpretation for the southern Sierra Nevada and Transverse Ranges anomalies may be that these two dipping high velocity bodies were part of the Farallon subduction system and remained attached to the North American lithosphere when subduction ceased.

5.4.6 The Coast Ranges

At 100 km depth, a low velocity zone is located beneath and along the length of the Coast Ranges from the northern Washington to central California. This is particularly clear in DNA07-P where the anomaly is strong everywhere except northern Oregon. The strongest anomalies, in DNA07-P and -S, are beneath the Olympic Mountains and northern California (Fig. 5.9).

This low velocity zone can also be observed in the vertical cross-sections of A-A' to H-H' in Fig. 5.10. The depth it reaches in different cross-sections ranges from ~200 km in the north to >500 km in the south. An explanation is that the low velocity layer has been carried with the oceanic lithosphere from the Juan de Fuca ridge. Low shear velocities have been observed in the upper 200 km offshore west of northern Oregon and

Washington near the Juan de Fuca ridge in the global model S20RTS leading to it being categorized as a ridge-type hotspot [*Ritsema and Allen, 2003*].

At the southern end of the anomaly (E-E' to H-H') this low velocity zone lies directly beneath the subducting slab and has a similar dip as the slab. A similar low velocity feature was observed in JdF07 by *Xue and Allen (2007)* and was interpreted as the remnant plume head material that spread beneath the oceanic lithosphere when the Yellowstone plume head impacted the North American Lithosphere around 17 Ma. The appearance of the feature on cross-sections E-E' through H-H' is consistent with this interpretation as these east-west sections straddle the latitude of the McDermitt Caldera (at 42°N) which is believed to have been the center of the plume head as it is the origin point for the Yellowstone hotspot track.

5.4.7 Low velocities above the Juan de Fuca slab

A strong north-south trending low velocity zone is observed east of the Cascades from southern Washington to northern Nevada (Fig. 5.9). This low velocity zone is parallel to the Cascades and extends from the surface down to 300 km depth with the maximum velocity perturbation located in central to northern Oregon. In vertical slices (Fig. 5.10), this low velocity anomaly is located above the subducted slab and can be seen in the cross-sections of C-C', D-D', E-E', F-F', G-G' and H-H'. This low velocity anomaly was also present in previous tomographic images (e.g. [*Humphreys and Dueker, 1994b; Dueker, et al., 2001*]). To the south this low velocity feature merges with the low

velocities of the Basin and Range province (F-F' through H-H'), to the north it is sandwiched between the high velocities of the slab and the Columbia River Basalts.

5.4.8 The “slab gap” south of the Mendocino Triple Junction

The “slab gap” was created and has been growing as the Mendocino triple junction migrated north [*Dickinson and Snyder, 1979*]. As the southern edge of the Juan de Fuca subduction system (the Gorda plate) migrates north with the triple junction, asthenospheric material emerges and upwells from beneath. We image the slab gap as a low velocity anomaly extending from the southern end of the Juan de Fuca (including the Gorda) subduction system to latitude of $\sim 37^{\circ}\text{N}$ just south of the San Francisco Bay region (Fig. 5.9). These low velocity anomalies are persistent to a depth of ~ 400 km in both DNA07-S and -P (Fig. 5.9 and Fig. 5.10 H-H' and I-I').

5.4.9 Velocity contrast across the San Andreas Fault

The San Andreas Fault system delineates strong velocity contrasts in two regions. At the northern end of the fault, from Cape Mendocino to the San Francisco Bay region, the high velocities of the Pacific plate are juxtaposed against the low velocities of the North American plate, as shown in Fig 5.9 at 100 km depth and G-G' to I-I' in Fig 5.10. The plate boundary in this region is along the coastline so only rays from the west recorded at the coastal stations provide constraints. The fault also divides the high velocities at the southern tip of the Central Valley and Sierra Nevada from the low velocities to the

southwest of the California Coast Ranges. As to the north, old oceanic lithosphere is adjacent to continental lithosphere but the oceanic material is to the east and the continental material is to the west. The oceanic lithosphere was subducted beneath the Sierra Nevada and the continental material is a slice that has been moved northward by the motion across the San Andreas Fault.

5.4.10 The volcanic arcs and the Central Valley

Negative station corrections (Fig 5.4) are observed along the Cascades and Sierra Nevada, indicating the crustal structure is fast which could be due to high velocity or thin crust. The most likely explanation is that these volcanic arcs have cold crystalline roots consisting of the residuals of previous melts. At 100 km depth, fast velocity anomalies are still observed beneath the Cascades in Oregon and northern California, representing the subducted Juan de Fuca plate (Fig. 5.9). However, fast velocity anomalies are not observed beneath the Sierra Nevada at 100 km depth due to the absence of any slab and indicating a shallow origin for the positive station corrections beneath the Sierra Nevada, i.e. a shallow depth for the Sierra Batholith. The negative station corrections of the Sierra Nevada contrast with the positive station corrections for the Central Valley indicating a relatively slow crustal structure likely due to the thick pile of sediments that fills the valley.

5.4.11 The Salton Trough

A zone of low velocity is observed under the Salton Trough rift valley, extending to a depth of about 200 km (Fig. 5.9). This is consistent with the suggestions that small-scale convective upwelling is occurring beneath the rift valley [Humphreys, *et al.*, 1984]. The vertical cross-section through the Salton Trough anomaly (Fig 5.10 L-L') reveals additional low velocity features extending to greater depth. How these may relate to the rifting processes extending south through the Gulf of California is unclear as this is the southern edge of our model.

5.4.12 The slow Basin and Range and the high velocity anomaly in central Nevada

Beneath the whole Basin and Range, a low velocity perturbation is persistent to a depth of ~300 km (Fig. 5.9). In vertical cross-sections through the Basin and Range from F-F' to I-I' in Fig. 5.10, a coherent low velocity perturbation is observed extending to ~300 km depth. This anomaly is expected as the whole region is under extension resulting in upwelling of the asthenosphere and a hotter mantle than normal [Humphreys and Dueker, 1994a; van der Lee and Nolet, 1997].

In the center of the Basin and Range low velocity region we also observe a smaller high velocity anomaly beneath central Nevada from 100 km to 300 km depth (Fig. 5.9). This anomaly is stronger in DNA07-P than in DNA07-S, and can be clearly seen in the vertical H-H' slice through DNA07-P. This anomaly has also been imaged in other body-wave tomographic studies (e.g. [Humphreys and Dueker, 1994b; Dueker, *et al.*, 2001]), and surface wave studies [Pollitz, submitted; Yang and Ritzwoller, submitted]. The high

velocity anomaly was tentatively interpreted as due to melt extraction [*Humphreys and Dueker, 1994b*], or thickened lithosphere [*Dueker and Humphreys, 1993; Pollitz, submitted*]. In DNA07-P the shallow (<400 km depth) high velocity feature connects to a deeper (> 400 km depth) high velocity anomaly to the east (see H-H', Fig 5.10). While the resolution degrades below ~500 km depth at this location (see H-H' in Fig 5.11), the dip of this feature is parallel to similar dipping features in slices from K-K' up to F-F'. We propose that this remnant feature in the Basin and Range is perhaps an old slab that was previously attached to the North American Craton. The slab-like anomaly is continuous from H-H' up to at least F-F' and perhaps E-E' in DNA07-P and while the anomaly is less slab-like, i.e. continuous, in DNA07-S, high velocity anomalies are present in the same locations.

5.4.13 The Colorado Plateau and the Rocky Mountain

The Colorado Plateau and the Rocky Mountain are located on the eastern edge of our study region and the resolution is therefore reduced. Both DNA07-S and -P image low velocity anomalies to depths of 300 to 400 km beneath the northwest and southwest margins of the Colorado Plateau, at the eastern edge of Basin and Range extension (Fig. 5.9).

Beneath the western Rocky Mountains high velocity anomalies are generally observed with the exception of the Yellowstone region and corresponding low-velocity anomaly (Fig. 5.9 and Fig. 5.10 from A-A' to F-F'). The contrast across the Wasatch

Front is clearly images as a transition from the low velocities of the Basin and Range to the high velocities of the Rocky Mountains.

5.5 Implications for mantle convection processes: The origin on Yellowstone and the fate of the Juan de Fuca slab

The observation that Juan de Fuca subduction system stops at a depth of 400 km supports the tectonic model proposed by *Xue and Allen (2007)* where the absence of the slab below 400 km depth today is due to the arrival of the Yellowstone plume head around 17 Ma. The plume head would need to break through the slab to reach the base of the North American lithosphere destroying the Juan de Fuca slab at depths greater than the thickness of the continental lithosphere. Beneath Oregon, the slab is further disrupted at depths < 400 km and has a reduced velocity contrast. The slab shallower than 400 km today had not been subducted at 17 Ma. The Oregon disruption to the slab may be due to lingering melting processes in this region where the plume impacted including the Newberry volcanism. The disruption of the slab in Oregon explains the absence of deep seismicity (> 30 km) in Oregon, an unusual observation for a subduction zone.

The low velocity zone immediately beneath the Juan de Fuca slab in southern Oregon and northern California has a similar dip to the slab and was interpreted by [*Xue and Allen, 2007*] as remnant plume head material being pulled down by the subducting slab after spreading beneath the oceanic lithosphere of the Juan de Fuca plate. An alternative hypothesis is that this material traveled with the Juan de Fuca plate from the Juan de Fuca

Ridge. There are also low velocity anomalies above the slab in this region which may also represent remnant plume head material that reached the surface when the Yellowstone plume head impacted the North American Lithosphere around 17 Ma. Whatever the causal mechanism is, these strong low velocity anomalies in Oregon correspond to a region where there is an absence of Wadati-Benioff zone earthquakes. Given that the low velocities most likely represent high temperatures, they may be modifying the frictional properties of the interface and be the reason for the absence of seismicity.

While the state of the Juan de Fuca plate can be explained by the proposed history of the Yellowstone Plume, beneath Yellowstone we image no vertical whole mantle plume. Instead we only image a strong low velocity anomaly down to 200 km depth directly beneath Yellowstone. This low-velocity feature then dips towards the northwest but stops at 500 km depth. There is a strong low-velocity region directly beneath Yellowstone at the top of the lower mantle, but there is no evidence for low-velocity conduit connecting this feature to the surface. The resolution limit of our dataset prevents us from recovering a conduit smaller than 50 km in diameter or the velocity perturbation less than 1.5% for S-velocity and 0.75% for P-velocity so a thin weak anomaly may remain undetected.

Jordan et al [CHECK REF – Bob Smiths group] propose that the low-velocity anomaly dipping to the northwest is the plume conduit. Mantle convection flow models suggest that the conduit could be deformed in the mantle “wind” which could also cause it to segment. This is their explanation for the fact that the anomaly appears to stop in the transition zone. Another possibility is that the plume was short lived. A significant

amount of plume material may have accumulated beneath the slab before breaking through, and today we only see the weak end of the upwelling anomaly. Alternatively there may never have been a mantle plume. However, we prefer the plume model for western North America for several reasons. The plume model is a single process which explains not only Yellowstone and the Yellowstone track, but also our observations of a broken and disrupted Juan de Fuca slab. It is also a mantle process validated by many numerical and analog experiments. Our model of slab disruption by a plume is also consistent with the geochemistry. At Yellowstone elevated $^3\text{He}/^4\text{He}$ ratios of up to 16 Ra (where 1 Ra = the $^3\text{He}/^4\text{He}$ ratio in air) have been observed and is often used to argue for a deep mantle source in the form of a plume (e.g. [Dodson, *et al.*, 1997]), although this is not uncontested e.g. [Christiansen, *et al.*, 2002]. In addition, the Columbia River Basalts are mainly aphyric basaltic andesites with a composition that requires a heterogeneous source involving ocean island basaltic material and recycled oceanic crust [Takahashi, *et al.*, 1998]. The suggestion of oceanic crustal material in the source of the Columbia River Basalts is explained by our model of interaction between the Yellowstone upwelling and the Juan de Fuca subduction system.

Low velocity anomalies beneath the High Lava Plains and along the Newberry track are observed shallower than 150 km depth and have no further continuation deeper into mantle. This supports the interpretation of an upper mantle origin for the Newberry track [Xue and Allen, 2006]. As fast directions from shear-wave splitting results do not align with the volcanic progression along the Newberry track, Xue and Allen [2006] concluded that the Newberry hotspot track is not a product of asthenospheric flow, and is more

likely a result of lithospheric processes. Even if lithospheric faulting is the cause of the Newberry track, the source region for the melts may still include remnant Yellowstone plume head material. The Newberry track itself, therefore, does not argue for or against the Yellowstone plume hypothesis.

5.6 Conclusions

Perhaps one of the most striking observations from DNA07-S and -P are just how heterogeneous mantle structure is beneath the western USA. Despite this heterogeneity, there is a very strong correspondence with the complicated tectonics of the region. The main features of the velocity models and their implications are:

North of the Mendocino Triple Junction

1. The Juan de Fuca subduction system stops at ~ 400 km, and is disrupted in Oregon, which we interpret as being due to interaction with the Yellowstone plume head.
2. West of the Cascades the forearc is imaged as a low velocity zone beneath the Coastal Ranges with the strongest velocity anomaly beneath the Olympic Mountains and northern California.
3. East of the Cascades and above the Juan de Fuca slab a north-south trending low velocity zone is imaged from southern Washington to northern Nevada.
4. A high velocity region is imaged from central Washington, through northern Oregon, and into Idaho. Beneath Washington the anomalies reach 250 to 300 km depth and deeper, ~400 km, beneath the Wallowa Mountains of northeast Oregon. These are

likely due to a combination of a cold and thick lithosphere and melt extraction during the eruption of the Columbia River Basalts.

5. The low velocity anomaly beneath Yellowstone dips towards the northwest and stops at 500 km depth.

6. A shallow low velocity zone to ~200 km depth lies beneath the Eastern Snake River Plain and does not appear connected to a deeper low velocity zone at the top of the lower mantle.

7. We do not detect a low velocity conduit reaching greater than 500 km depth beneath Yellowstone implying that either (1) any plume was short-lived; or (2) the conduit is < 50 km in diameter and/or the velocity perturbation is less than 1.5% for S and 0.75% for P and therefore unresolved; or (3) there was no deep mantle plume. We prefer the short-lived plume model as it best explains many of the imaged features the Pacific Northwest

8. There are only shallow low velocity anomalies (<150 km depth) along the Newberry hotspot track indicate no deep source.

South of the Mendocino Triple Junction

1. In California the high velocities of the Pacific plate are imaged abutting against the low velocity North American plate.

2. We image the “slab gap” as low velocity anomalies extending to 400 km depth from the southern end of the Juan de Fuca subduction system to the southern end of the Sierra Nevada. These anomalies are particularly strong just south of the Mendocino Triple Junction.

3. High velocity bodies are imaged beneath the southern tip of the Central Valley/Sierra Nevada and the Transverse Ranges with dips to the east. These may be part of a fossil Farallon subduction system.

4. The Basin and Range is a region of low velocities to a depth of ~300km. In the middle of the Basin and Range, in central Nevada, a high velocity feature is imaged extending to 300 km depth.

5. A zone of low velocity is observed to 200 km depth under the Salton Trough consistent with ongoing rifting and small scale convection in the region.

While the upper ~400 km of the DNA07 models correlate well with surface tectonics and geologic provinces, the deeper structure (400-750km) is equally complex and not easily explained in terms of either existing geologic or geodynamic models. Their further investigation is therefore warranted.

Figure captions

Fig. 5.1 Tectonic map for the study region. Labeled features [*Humphreys and Dueker, 1994b*] are OH, Okanogan Highlands; OM, Olympic Mountains; OCR, Oregon Coast Ranges; CCR, California Coast Ranges; KM, Klamath Mountains; MP, Modoc Plateau; MTJ, Mendocino Triple Junction; CV, Central Valley; SN, Sierra Nevada; SAF, San Andreas Fault; TR, Transverse Ranges; ST, Salton Trough; CRB, Columbia River Basalts; BM, Blue Mountains; WM, Wallowa Mountains; NC, Newberry Caldera; MC, McDermitt Caldera; YC, Yellowstone Caldera; YHT, Yellowstone hotspot track along

the eastern Snake River Plain; B&R, Basin and Range; SB&R, southern Basin and Range; TMC, Timber Mountain Caldera; SGVT, Saint George Volcanic Trend; CP, Colorado Plateau; WF, Wasatch Front; RMF, Rocky Mountain Caldera. Black lines trending northwest across Oregon indicates right-lateral strike-slip faults. Dike swarms associated with the 17 Ma basaltic outpourings are shown in gold [Christiansen, *et al.*, 2002]. Plate motions from HS3-NUVEL 1A are shown as black arrows [Gripp and Gordon, 2002].

Fig. 5.2 The seismic stations used in this study with a total number of 809.

Fig. 5.3 Distribution of (a) 88 events and 23233 rays used in the DNA07-S model inversion and (b) 58 events and 15141 rays used in the DNA07-P model. The red dots indicate events providing good direct S phases in (a) and P phases in (b). The yellow dots indicate events providing good SKS phases which are overlay on the red dots.

Fig. 5.4 Station corrections for (a) the DNA07-S model and (b) DNA07-P model. Unites for the color scale are seconds.

Fig. 5.5 Checker-board test for cell size of 250 km for the DNA07-S model. Depth slices of the recovered model are shown at (a) 375 km, (b) 500 km, and (c) 625 km. Vertical slices the recovered model and their corresponding cross-sections are shown in a map view in the right column and the middle column respectively with (d) at 46.42°N, (e) 45.40°N, and (f) 42.20°N. On the right side of each slice shows the corresponding ray density plot with white indicates zero hits and black indicates 100+ hits. The amplitude of

the input V_s anomaly is 3%. Input models are overlain on the recovered models by thick lines with blue for high velocity anomaly and red for low velocity anomaly. The contour interval is 0.5% indicated by vertical lines in the color bar of the velocity scale. Zero contours are not shown.

Fig. 5.6 Checker-board test for a cell size of 250 km for the DNA07-P model. Depth slices and vertical slices of the recovered model are shown at the same depths and cross-sections as Fig. 5.5. The amplitude of the input V_p anomaly is 1.5%. Again input models are overlain on the recovered models by thick lines with blue for high velocity anomaly and red for low velocity anomaly. The contour interval is 0.25% indicated by vertical lines in the color bar of the velocity scale. Zero contours are not shown.

Fig. 5.7 Checker-board test for a cell size of 500 km for the DNA07-S model. Depth slices of the recovered model are shown at (a) 250 km, (b) 500 km, and (c) 750 km. Other descriptions are the same as in Fig. 5.5.

Fig. 5.8 Checker-board test for cell size of 500 km for the DNA07-P model. Depth slices and vertical slices of the recovered model are shown at the same depths and cross-sections as Fig. 5.7. Other descriptions are the same as in Fig. 5.6.

Fig. 5.9 Depth slices through the DNA07-S model (left column) and DNA07-P model (right column) from 100 km to 800 km depth with an interval of 100 km. On the right

side of each velocity slice is the corresponding ray density plot where white indicates zero ray hits and black indicates 100+ hits.

Fig. 5.10 (a) Locations of the cross-sections of vertical slices shown in Fig. 5.10b and Fig. 5.11. (b) Vertical slices through the DNA07-S (left column) and DNA07-P (right column) models. The locations of the cross-sections are shown in (a). The color scale is the same as in Fig. 5.9.

Fig. 5.11 Checker-board test for cell size of 200 km for (a) the DNA07-S and (b) DNA07-P models. For each model, the left column is the input model and the right column is the output model. The cross sections are taken through the same locations to those in Fig. 5.10. The amplitude of the input is 3% for V_s and 1.5% for V_p . Note: as the input amplitudes varies due to it sliced along the great circle instead of a straight line through the same maximum amplitudes, weaker anomalies in the outputs do not necessarily mean worse recoveries. The contour interval and color scale are the same as in Fig. 5.5 and Fig. 5.6.

Fig. 5.12 Resolution tests on the observed slab feature for (a) the DNA07-S and (b) –P models. For each model, there are two tests: the recovered model for a synthetic slab ending at 400 km (left column) and the recovered model for a synthetic slab ending at 600 km (right column). The cross-sections are the same locations as those in Fig. 5.10 and Fig. 5.11. Input models are overlain on the recovered models by thick lines with blue for

high velocity anomaly. The contour interval and color scale are the same as in Fig. 5.5 and Fig. 5.6.

Fig. 5.13 Vertical slices through the DNA07 models: (a) a NW-SE cross-section through the Yellowstone Caldera; (b) the synthetic test along the same cross-section as (a); (c) a cross-section along the East Snake River Plain.

Fig. 5.14 A synthetic test for a mantle plume located beneath the Yellowstone caldera. The input anomaly has a radius of 50 km and extends from 0 to 1000 km depth with -3 % velocity perturbation for S and -1.5 % for P. (a) the same NW-SE cross-section as in Fig. 5.13a through the input model and (b) the recovered model; (c) the same cross-section along the East Snake River Plain as in Fig. 5.13c through the input model and (d) the recovered model.

Fig. 5.15 Vertical slices through the Transverse Ranges anomaly: (a) an east-west cross-section along the trend of the Transverse Ranges; (b) a south-north cross-section perpendicular the trend of the Transverse Ranges.

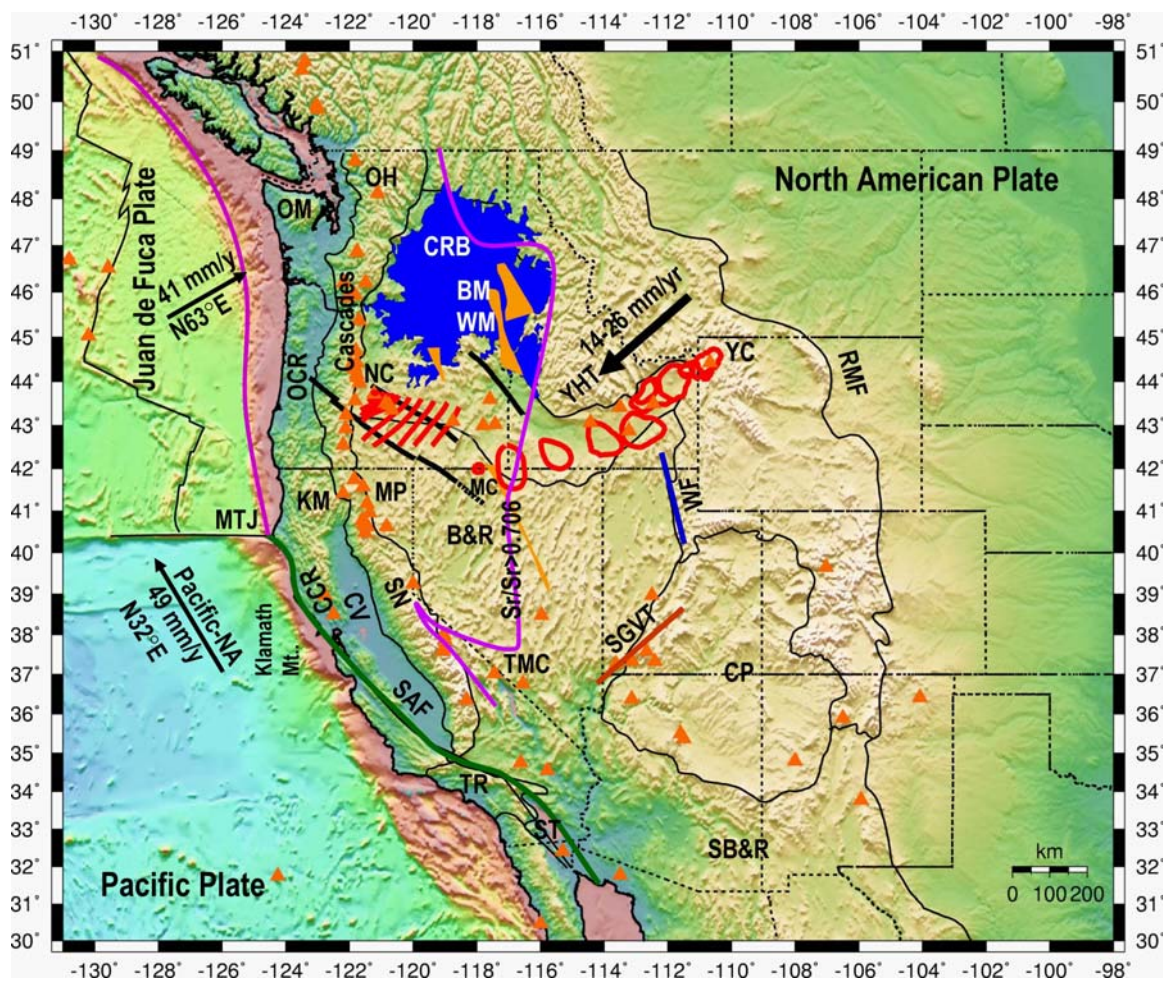


Fig. 5.1

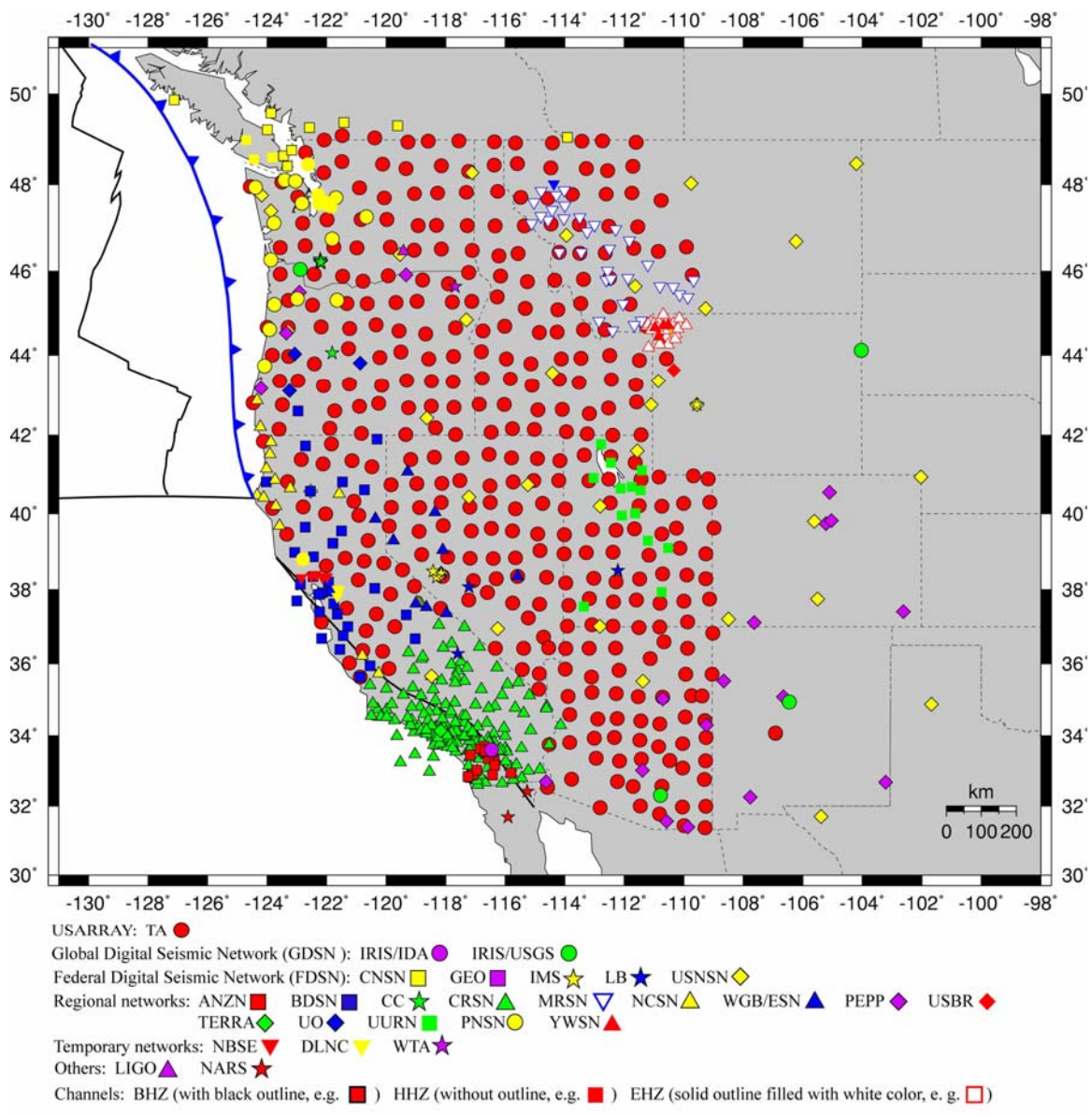


Fig. 5.2

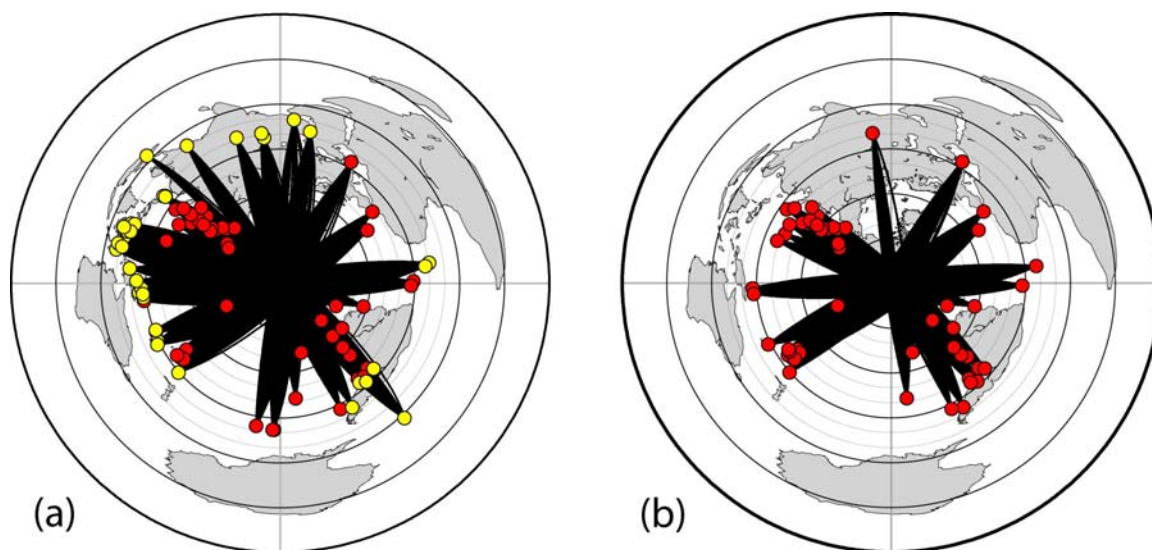


Fig. 5.3

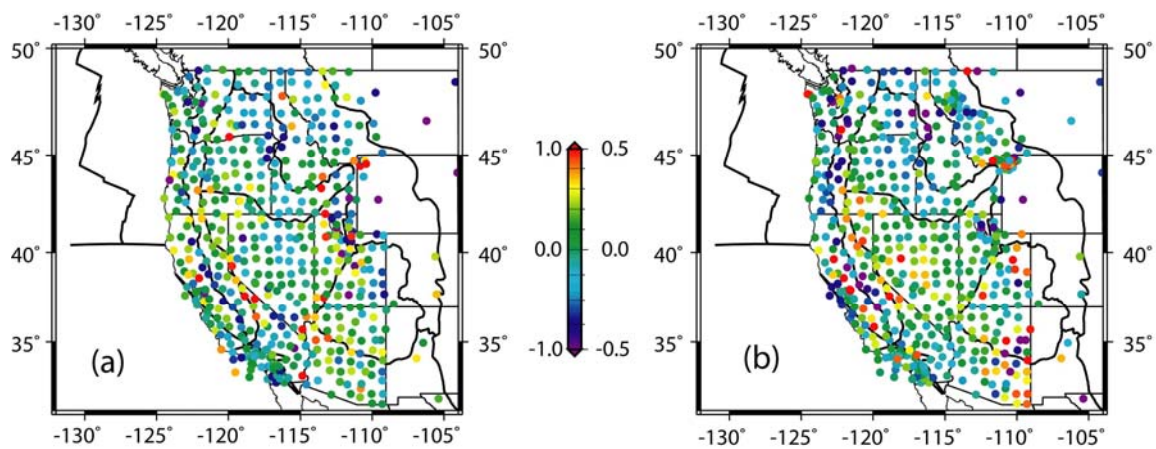


Fig. 5.4

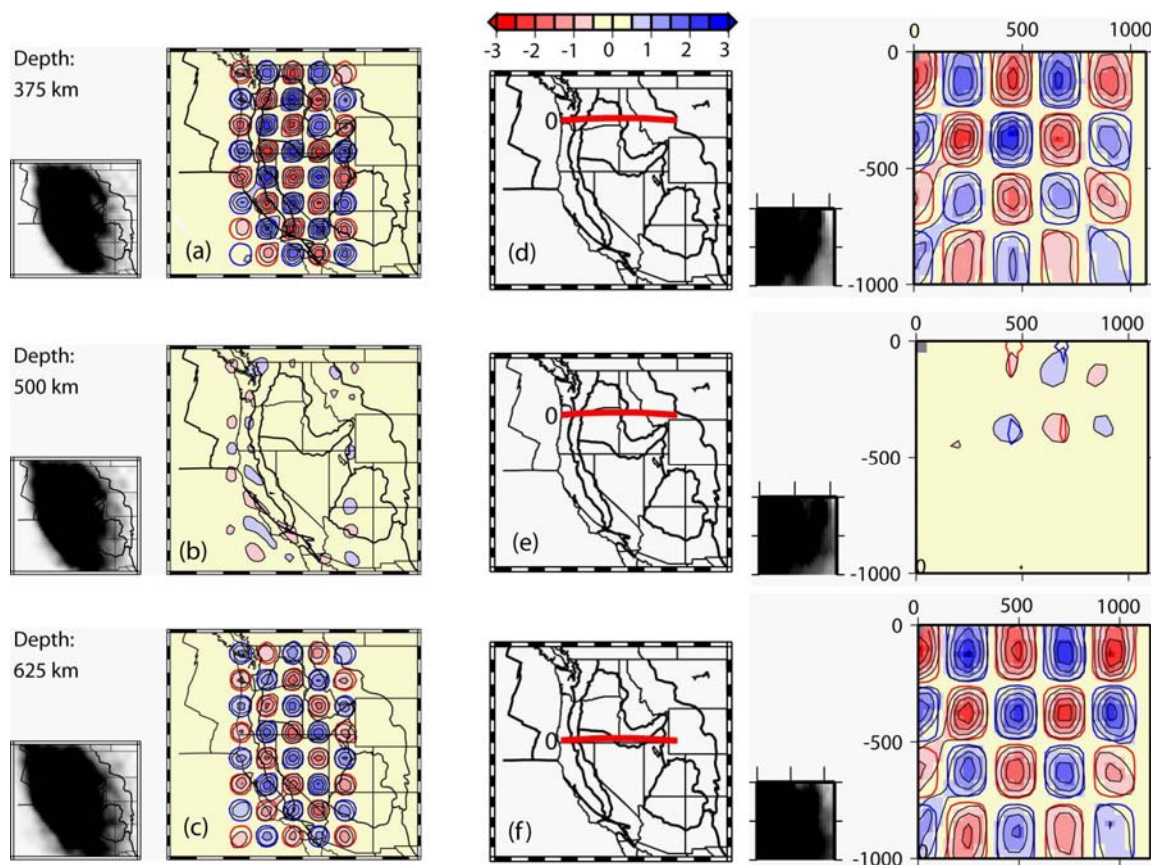


Fig. 5.5

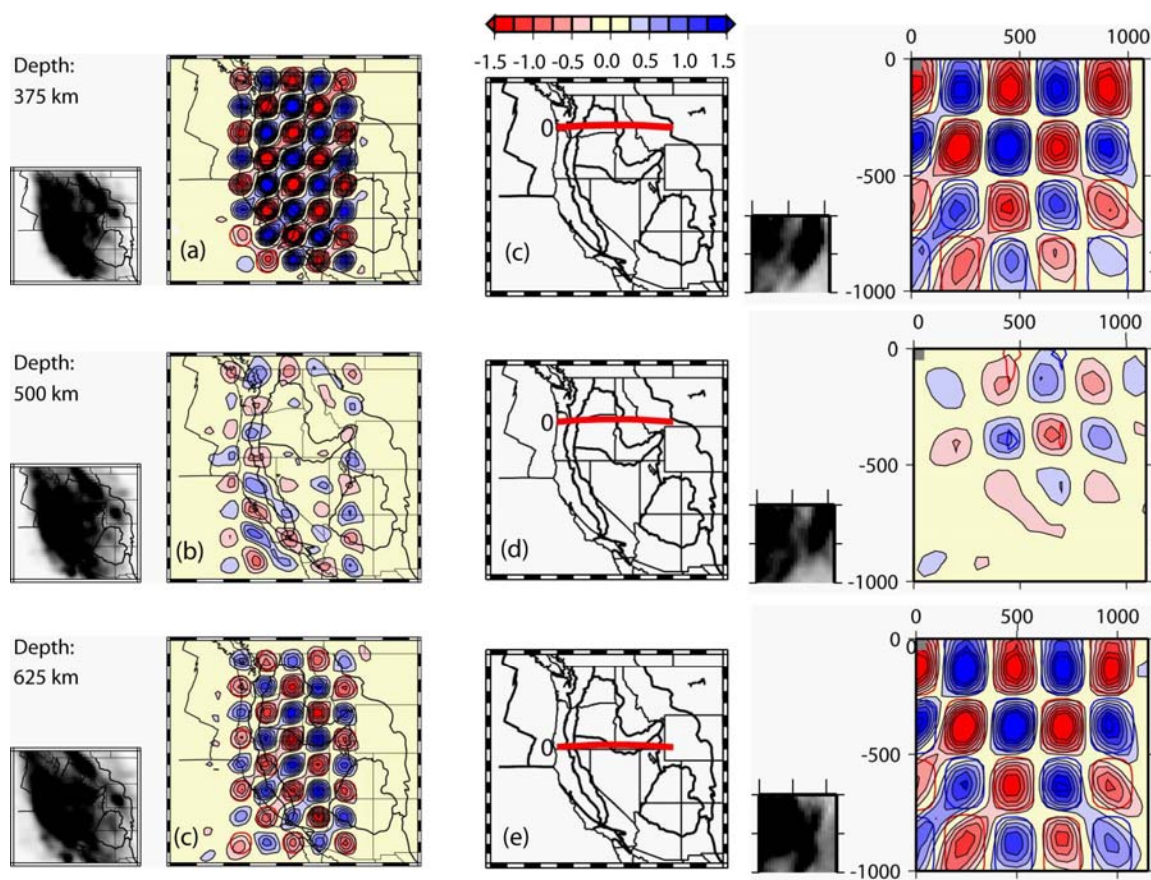


Fig. 5.6

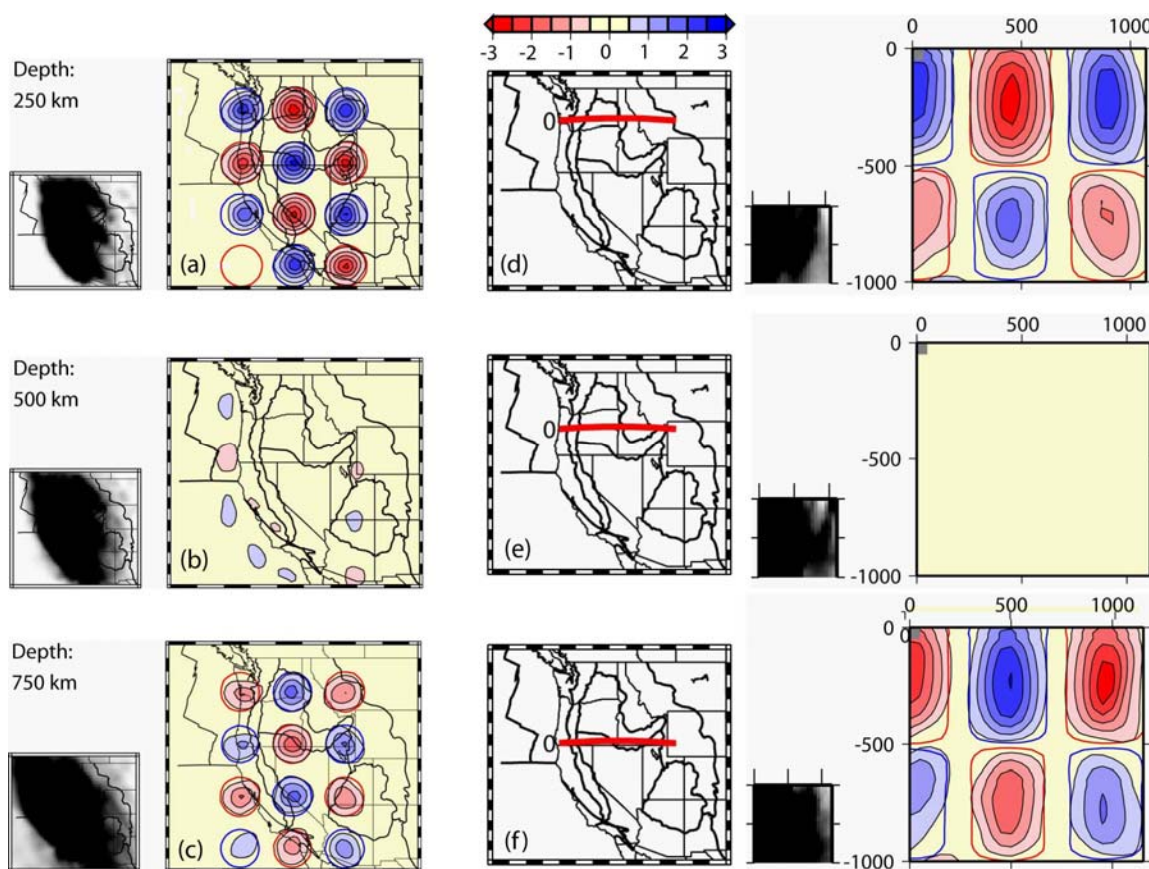


Fig. 5.7

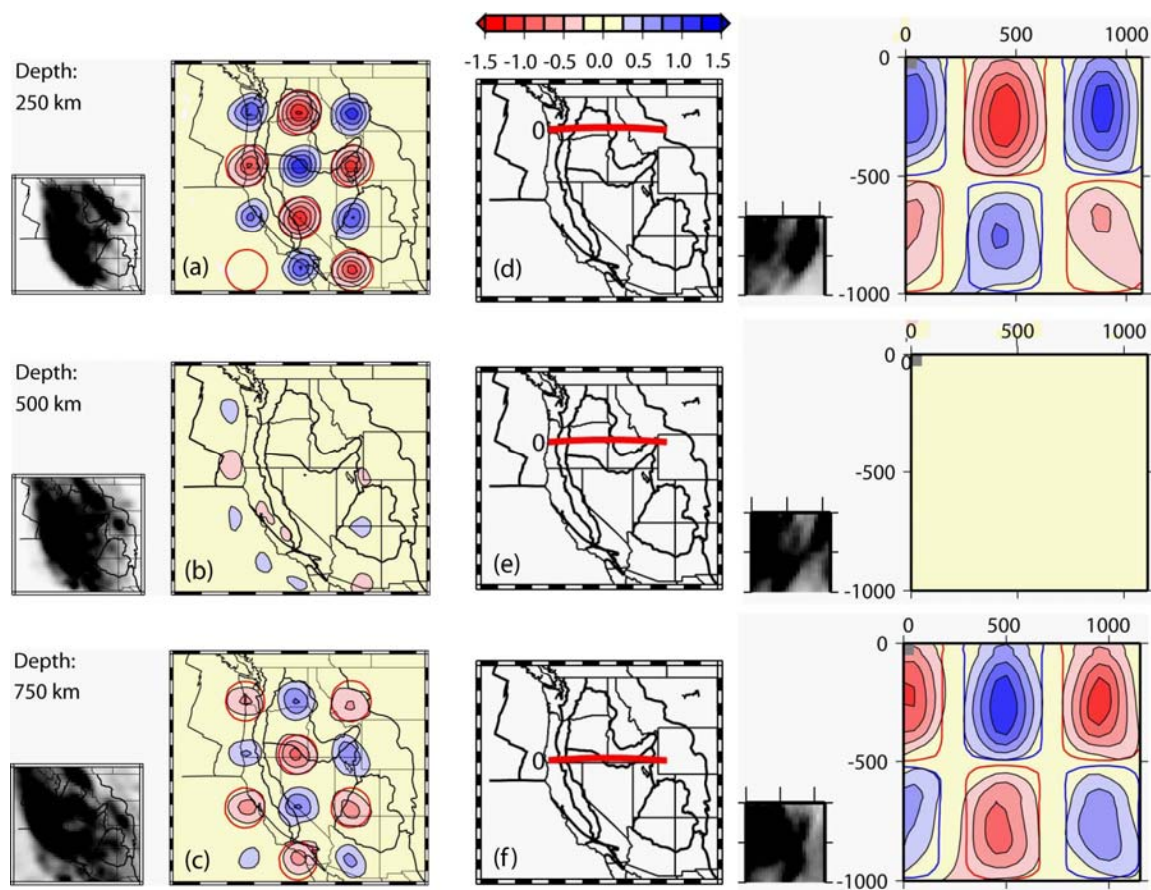


Fig. 5.8

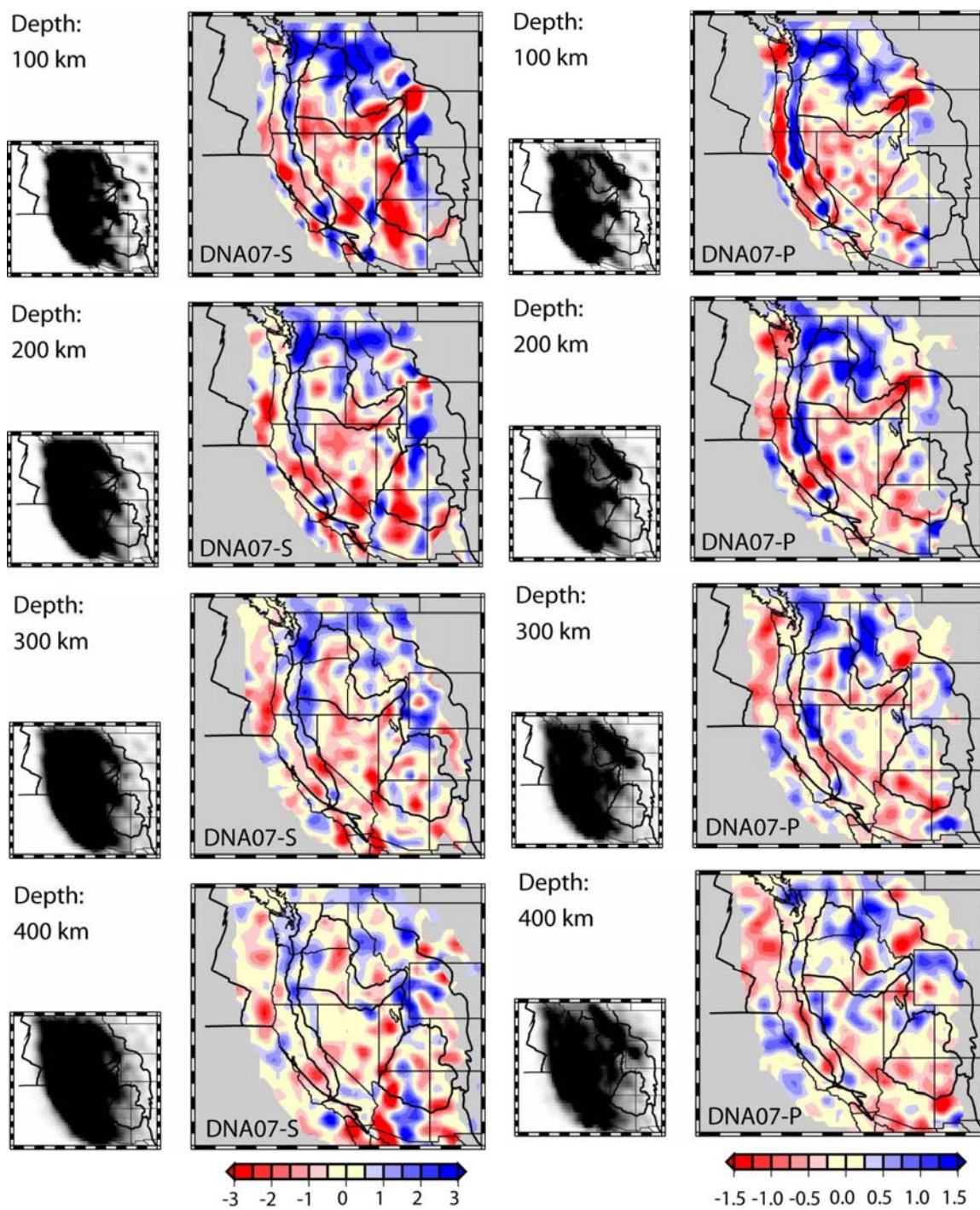


Fig. 5.9

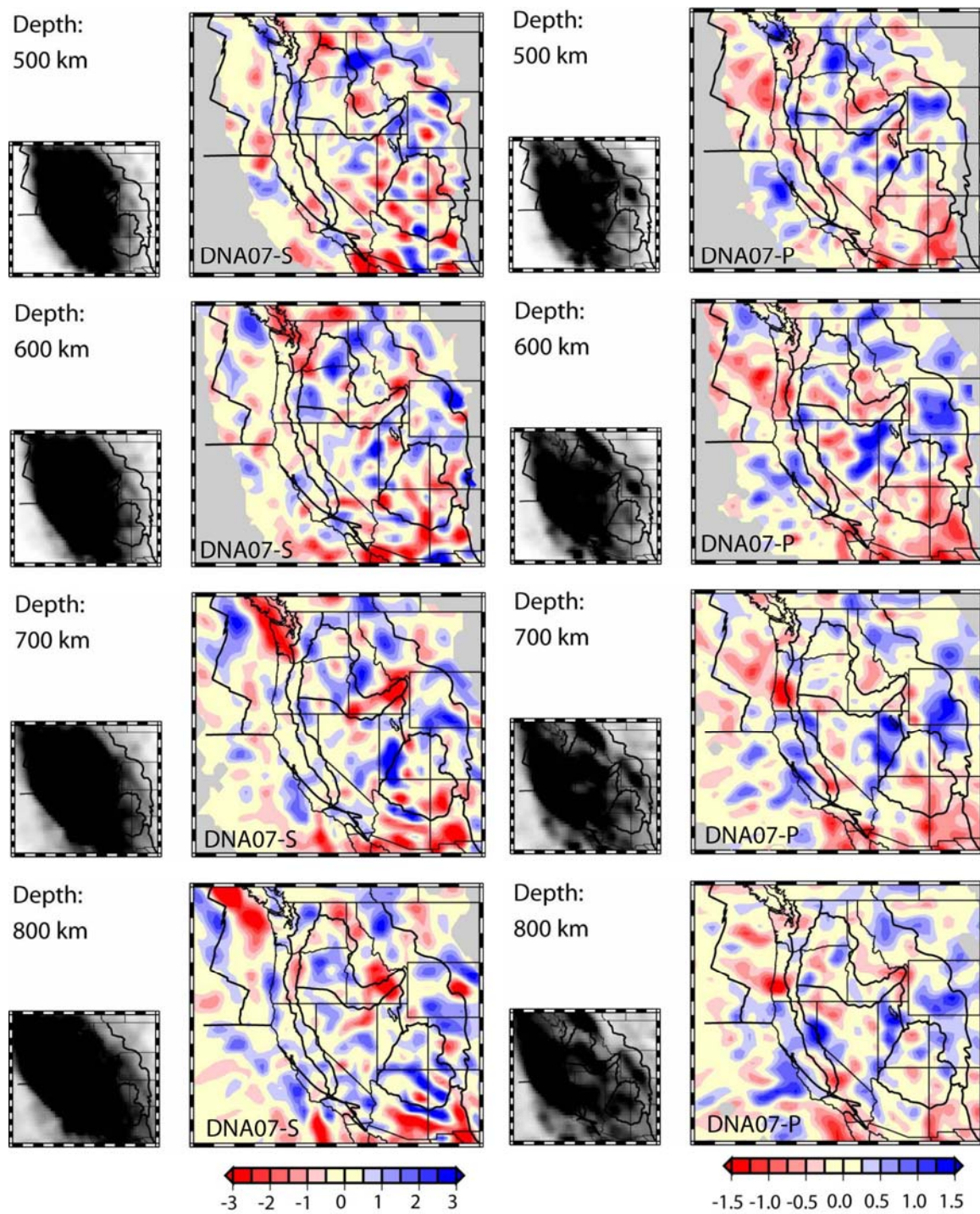


Fig. 5.9 (continued)

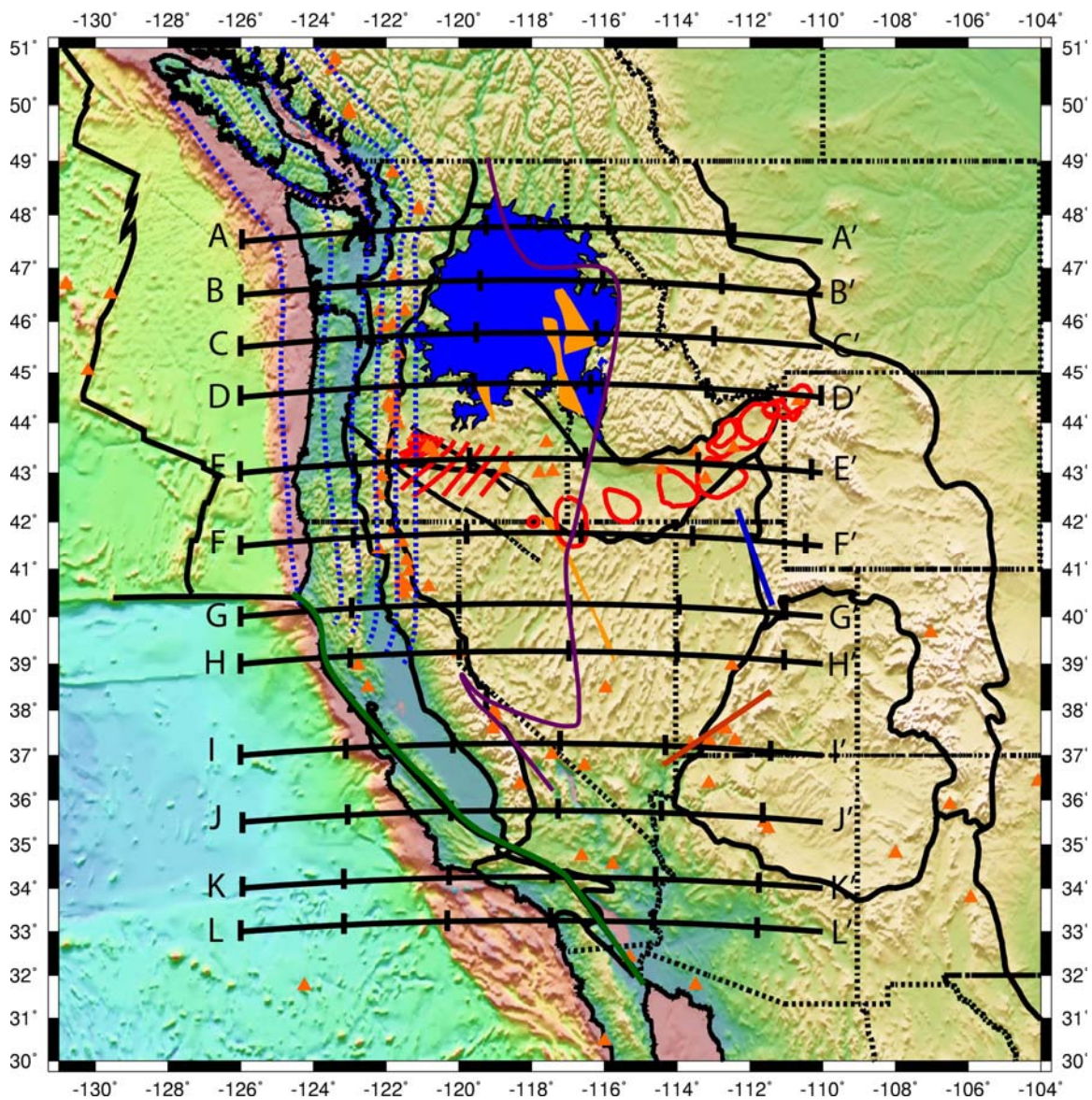


Fig. 5.10

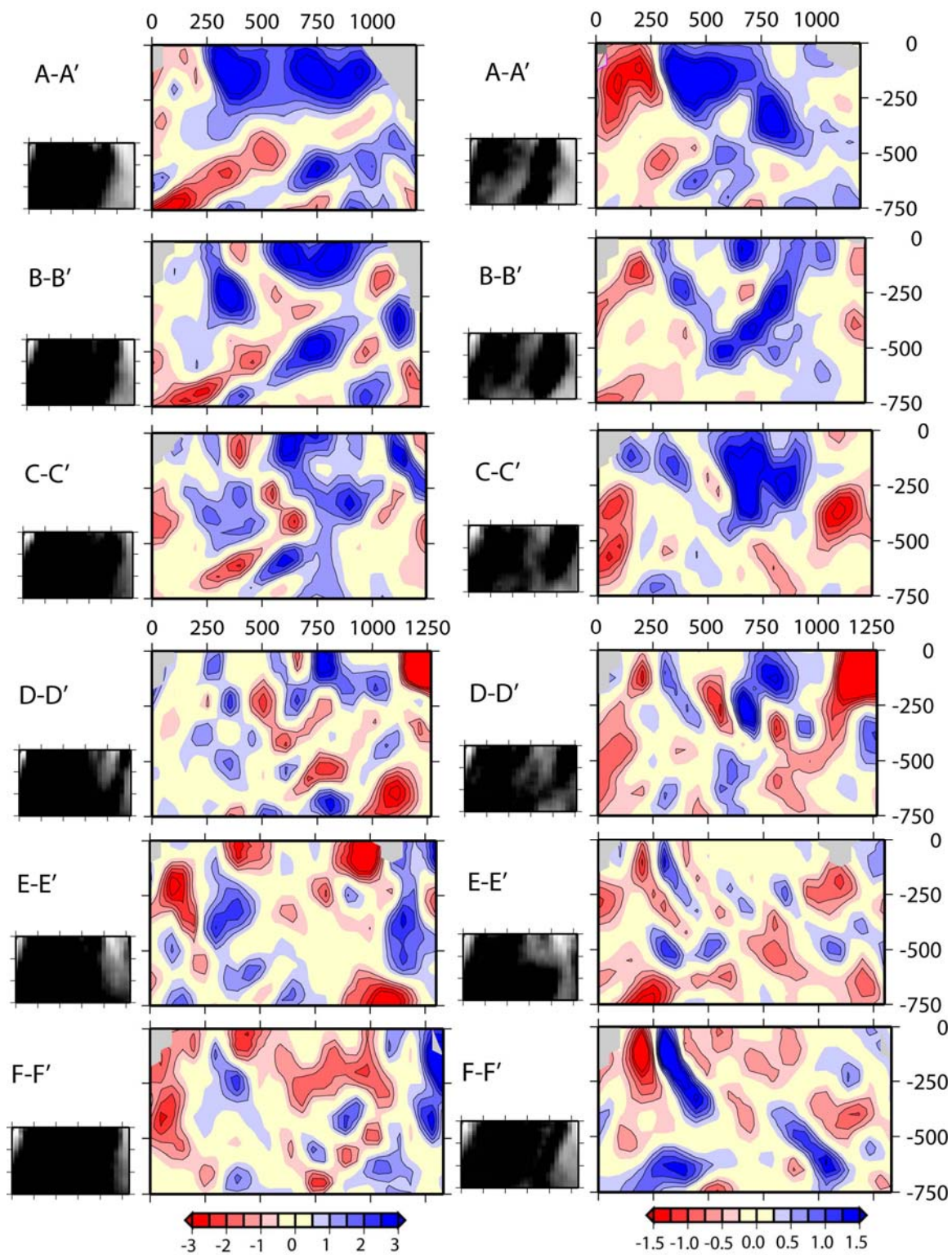


Fig. 5.10 (continued)

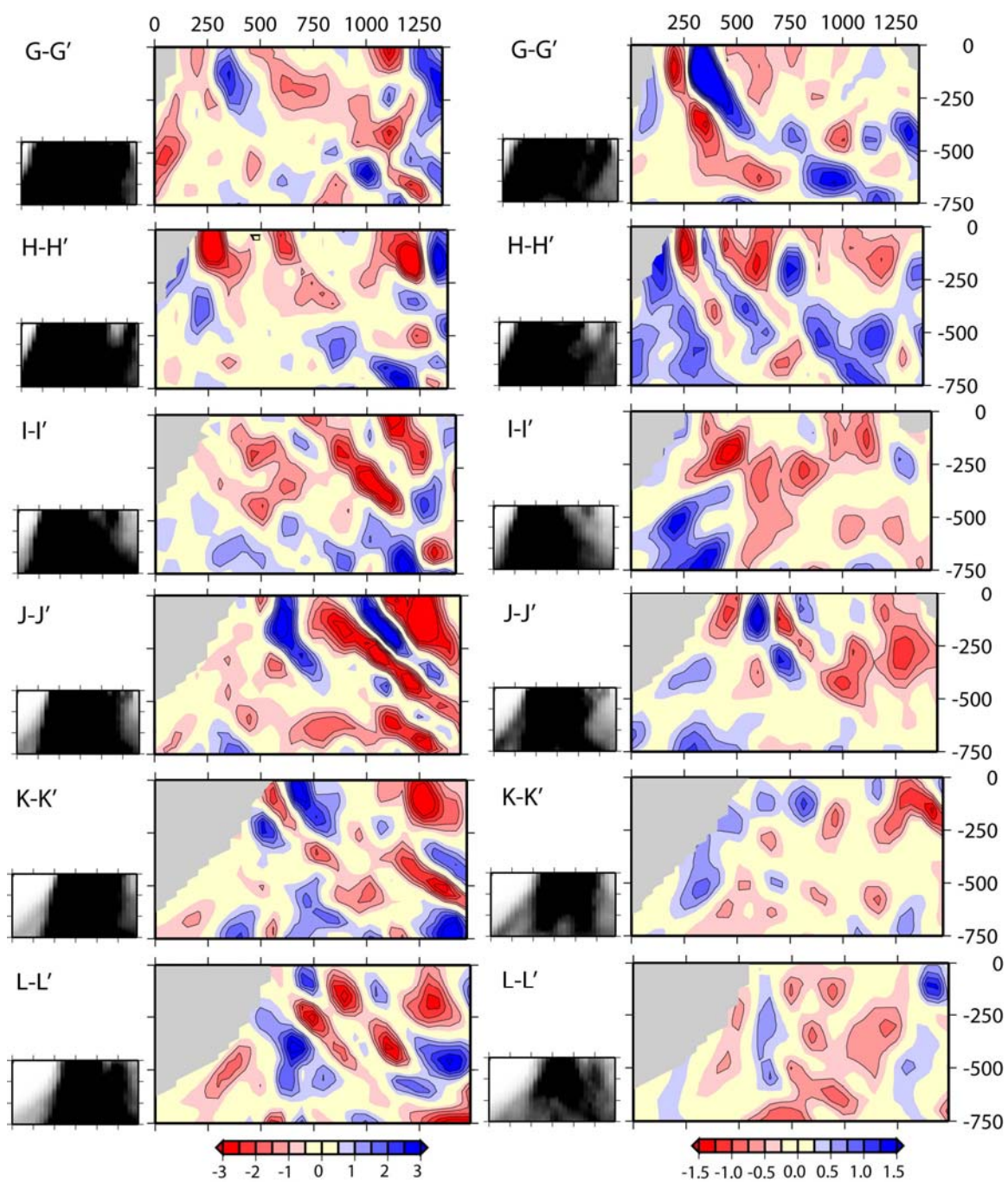


Fig. 5.10 (continued)

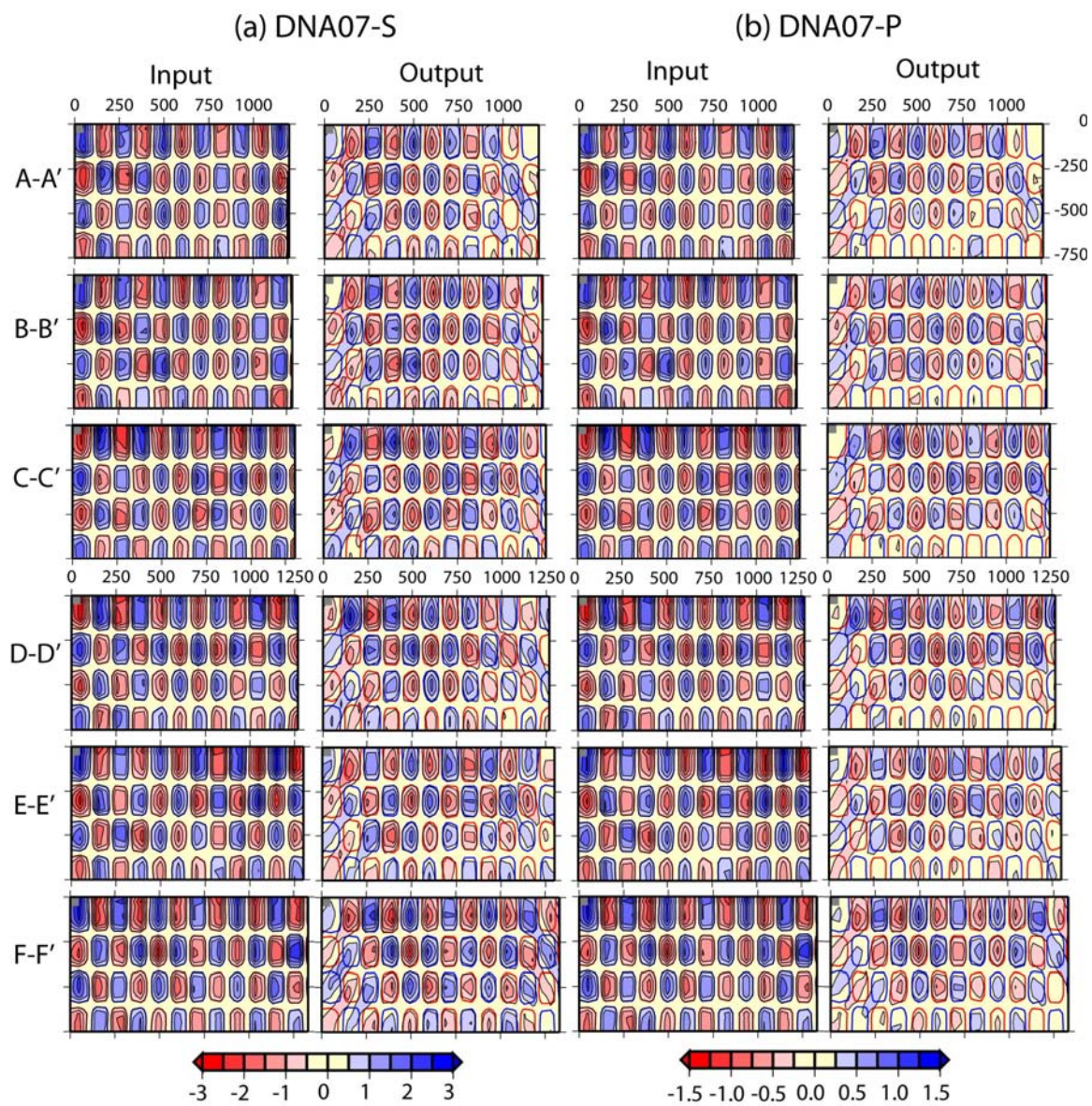


Fig. 5.11

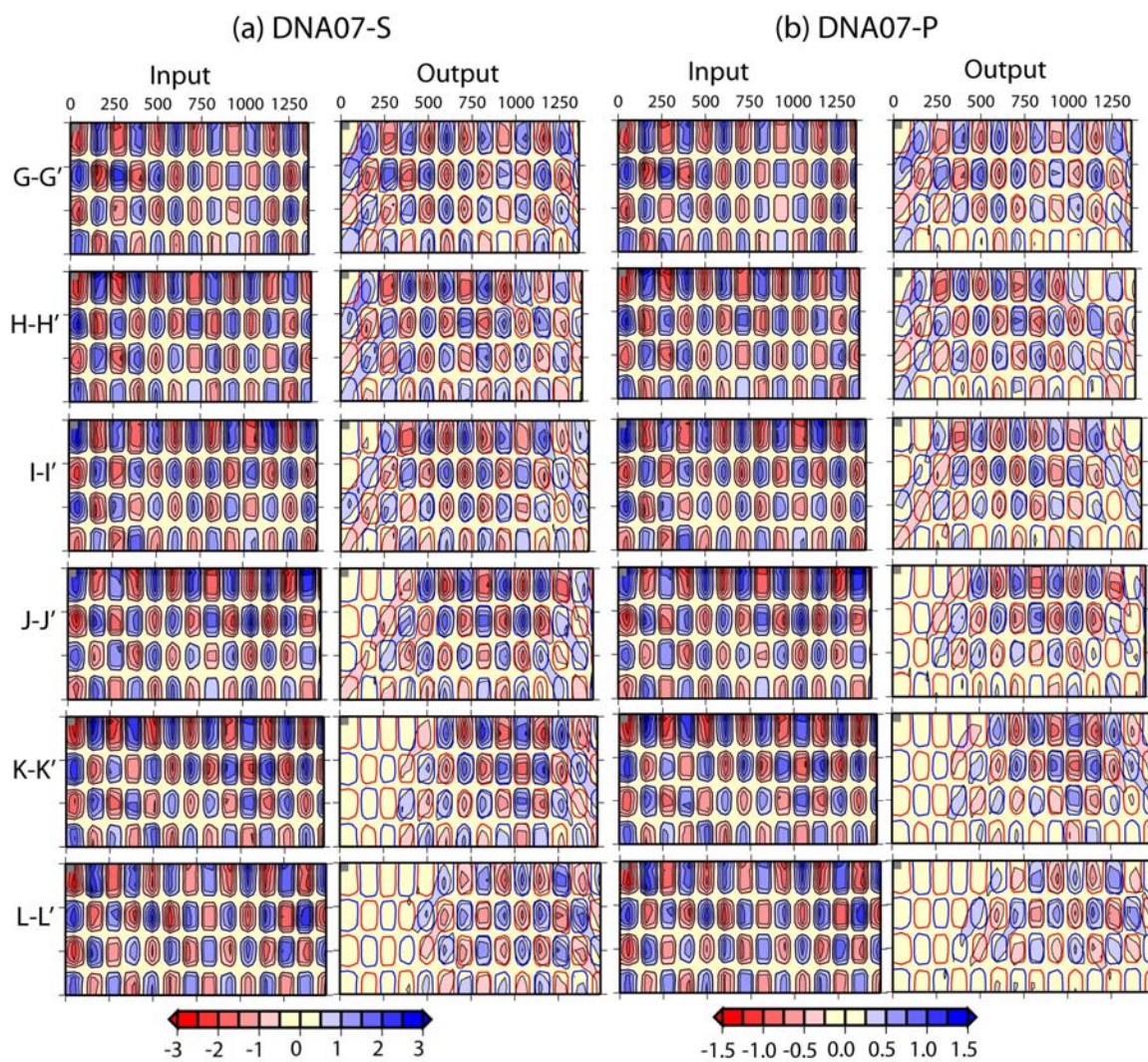


Fig. 5.11 (continued)

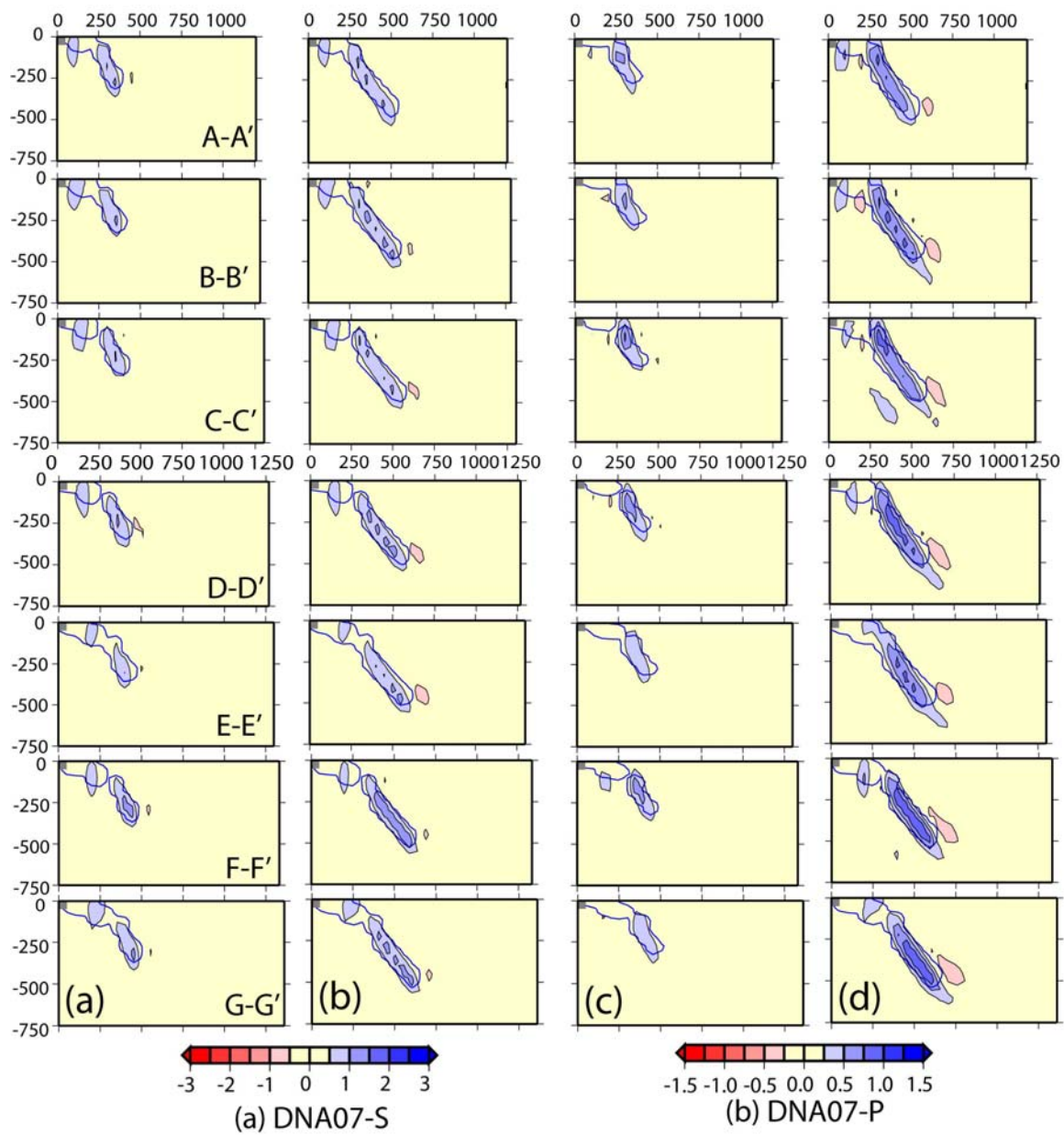


Fig. 5.12

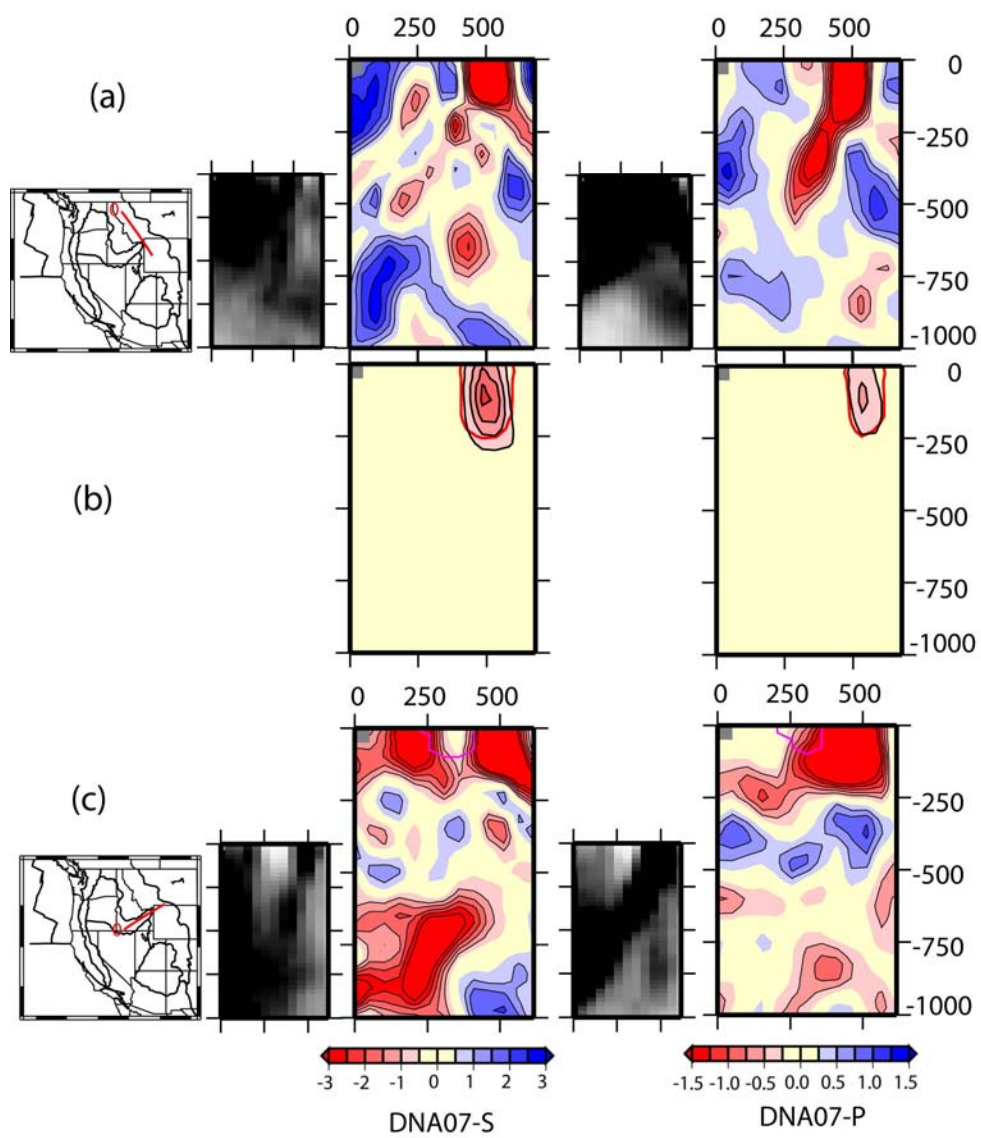


Fig. 5.13

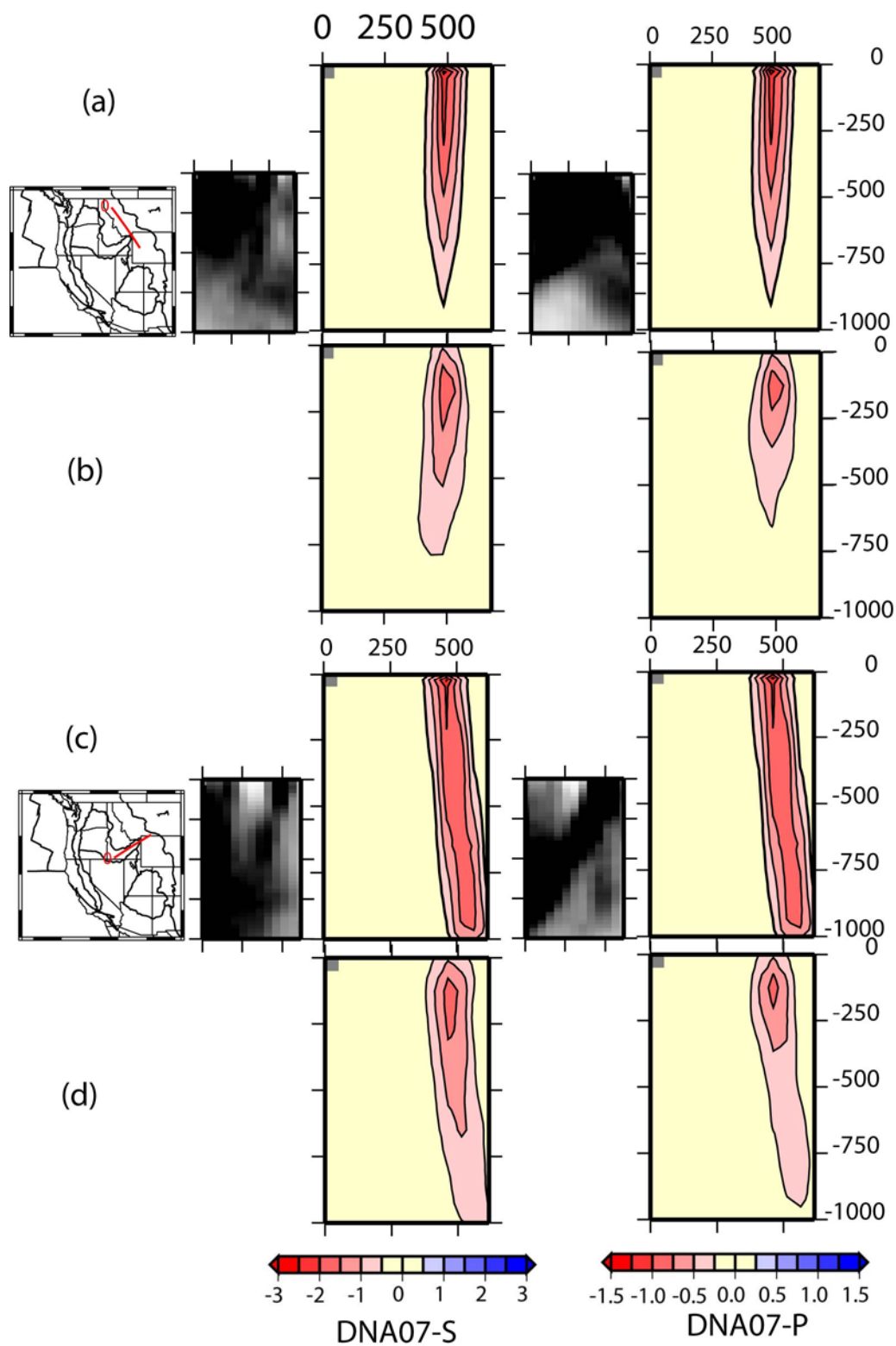


Fig. 5.14

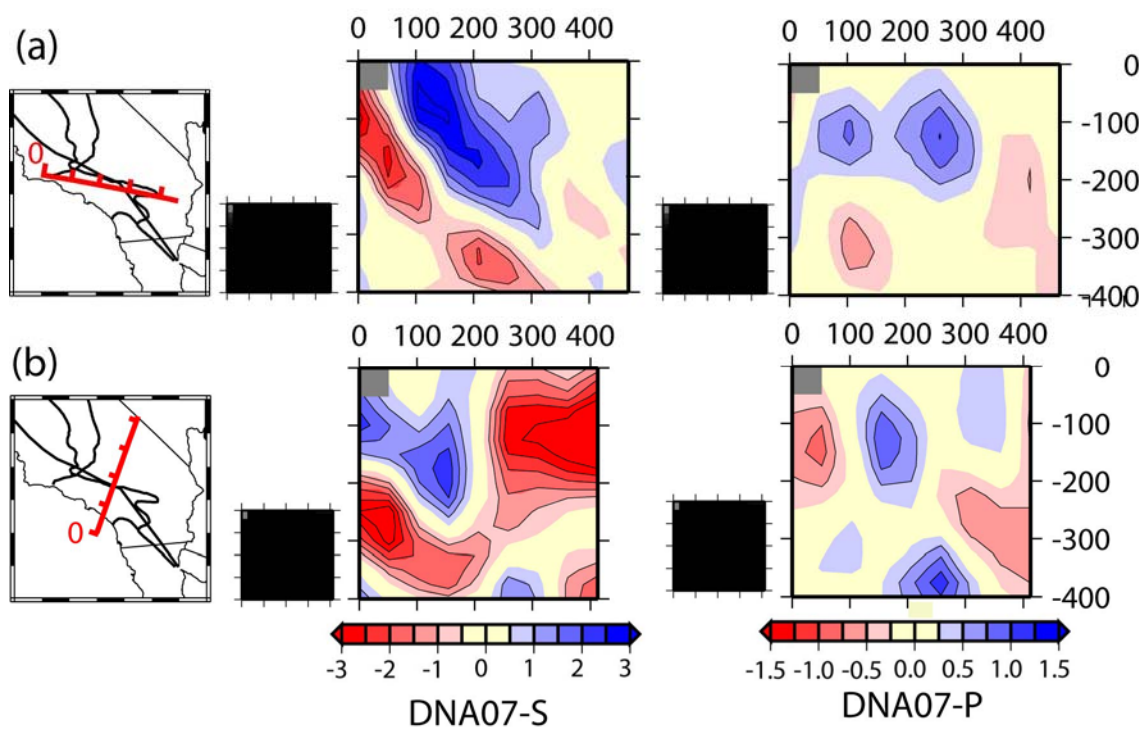


Fig. 5.15

Chapter 6

Conclusion

Seismic tomography and shear-wave splitting methods are effective tools to study mantle structures which in turn help to understand the causal mantle convection processes. Our observed anisotropy pattern beneath Iceland reveals the horizontal flow of the Icelandic upwelling material toward and then down the North Atlantic Ridge. Material initially flows from the axis of upwelling beneath southeast Iceland to the northwest in what might be considered as ridge perpendicular flow from an off-ridge hotspot toward the ridge. Material then flows to the north and southwest down the Kolbeinsey and Reykjanes ridges respectively. These observations are consistent with the observed generation of V-shaped ridges along the Reykjanes and Kolbeinsey ridges due to channeling of upwelling material down the ridges.

SKS splitting observations across Oregon suggest a simple pattern of anisotropy which varies smoothly across the region. We infer a single layer of anisotropy beneath the Newberry Hotspot Track that is most likely the asthenosphere. The fast directions are oriented ENE-WSW to the west of the Cascades which is consistent with mantle shear parallel to subduction of the Juan de Fuca Plate. To the east, fast directions are more E-W, perhaps due to shear caused by Basin and Range. Since the observed fast directions are not parallel to the Newberry track, it is unlikely that asthenospheric flow is responsible for the age-progression volcanism. Instead, we suggest the Newberry track is the product of a lithosphere-controlled process. The most likely explanation is therefore progressive

lithospheric faulting related to the extension of Basin and Range. A geological study of surface deformation in the region could confirm this conclusion but such a study is still lacking.

We image the Juan de Fuca plate as a high velocity anomaly dipping into the mantle east of the Cascades beneath Oregon that stops at ~ 400 km depth. It has a dip of $\sim 50^\circ$ to the east and a thickness of ~ 75 km. We also image a layer of low velocity immediately beneath the slab extending to a depth of at least 575 km with a similar geometry as the slab. These observations led us to propose that the absence of the slab below 400 km depth today is due to the arrival of the Yellowstone plume head around 17 Ma. On its way to the surface the plume destroyed the Juan de Fuca slab at depths greater than the thickness of the continental lithosphere. Traction with the subducting plate would then pull some plume head material down into the mantle which is now imaged as the low velocity layer beneath the slab in our V_s model. This hot remnant plume head material beneath the slab would warm the slab and may therefore reduce its strength and ability to generate earthquakes. This may be partly responsible for the absence of a Wadati-Benioff zone associated with the subduction of the Juan de Fuca plate.

We built high resolution seismic velocity models for the entire western USA (DNA07-S for S-velocity and DNA07-P for P-velocity). These models show that the mantle structure beneath the western USA is very heterogeneous. Despite this heterogeneity, there is a very strong correspondence with the complicated tectonics of the region. The image of the Juan de Fuca subduction system confirms that it stops at ~ 400

km, and is disrupted in Oregon, which we interpret as being due to interaction with the Yellowstone plume head. Beneath Yellowstone, a low velocity anomaly is observed dipping towards the northwest but stops at 500 km depth. We do not detect a low velocity conduit reaching greater depths beneath Yellowstone as would be required in a whole mantle plume is present today. This implies that either (1) any plume was short-lived; or (2) the conduit is beyond our resolution; or (3) there was no deep mantle plume. We prefer the short-lived plume model as it best explains many of the imaged features in the Pacific Northwest. The other important features in the models are: shallow low velocity anomalies (<150 km depth) along the Newberry hotspot track indicating no deep source; the high velocity region from central Washington, through northern Oregon, and into Idaho, which is likely due to a combination of a cold and thick lithosphere and melt extraction during the eruption of the Columbia River Basalts; the high velocities of the Pacific plate are imaged abutting against the low velocity North American plate in California; the “slab gap” shown as low velocity anomalies extending to 400 km depth from the southern end of the Juan de Fuca subduction system to the southern end of the Sierra Nevada; high velocity bodies beneath the southern tip of the Central Valley/Sierra Nevada and the Transverse Ranges dip to the east which may be part of a fossil Farallon subduction system; a high velocity feature extending to 300 km in the central Basin and Range which is otherwise categorized as a region of low velocities to a depth of ~300km. The deeper mantle structure (400-750km) is as complex as the shallow mantle and not easily explained in terms of either existing geologic or geodynamic models. Their further investigation is therefore warranted.

Bibliography

M. Albers and U. R. Christensen, Channeling of plume flow beneath mid-ocean ridges, *Earth and Planetary Science Letters*, 187, 207-220, 2001.

R. M. Allen, et al., The thin hot plume beneath Iceland, *Geophysical Journal International*, 137, 51-63, 1999.

R. M. Allen, et al., Imaging the mantle beneath Iceland using integrated seismological techniques, *Journal of Geophysical Research-Solid Earth*, 107, 2325, doi:2310.1029/2001JB000595, 2002a.

R. M. Allen, et al., Plume-driven plumbing and crustal formation in Iceland, *Journal of Geophysical Research-Solid Earth*, 107, 2163, doi:2110.1029/2001JB000584, 2002b.

C. Bassin, et al., The Current Limits of Resolution for Surface Wave Tomography in North America, *EOS Trans AGU*, 81, 2000.

R. E. Bell and W. R. Buck, Crustal Control of Ridge Segmentation Inferred from Observations of the Reykjanes Ridge, *Nature*, 357, 583-586, 1992.

W. Ben Ismail and D. Mainprice, An olivine fabric database: an overview of upper mantle fabrics and seismic anisotropy, *Tectonophysics*, 296, 145-157, 1998.

H. Bijwaard, et al., Closing the gap between regional and global travel time tomography, *Journal of Geophysical Research-Solid Earth*, 103, 30055-30078, 1998.

I. T. Bjarnason, et al., Shear wave splitting across the Iceland hot spot: Results from the ICEMELT experiment, *Journal of Geophysical Research-Solid Earth*, 107, 2382, doi:2310.1029/2001JB000916, 2002.

D. K. Blackman, et al., Teleseismic imaging of subaxial flow at mid-ocean ridges: Traveltime effects of anisotropic mineral texture in the mantle, *Geophysical Journal International*, 127, 415-426, 1996.

M. G. Bostock and J. F. Cassidy, Variations in SKS Splitting across Western Canada, *Geophysical Research Letters*, 22, 5-8, 1995.

M. G. Bostock, et al., An inverted continental Moho and serpentinization of the forearc mantle, *Nature*, 417, 536-538, 2002.

M. G. Bostock and J. C. VanDecar, Upper-Mantle Structure of the Northern Cascadia Subduction Zone, *Canadian Journal of Earth Sciences*, 32, 1-12, 1995.

A. D. Brandon and G. G. Goles, A Miocene Subcontinental Plume In The Pacific Northwest - Geochemical Evidence, *Earth And Planetary Science Letters*, 88, 273-283, 1988.

M. G. Braun and R. A. Sohn, Melt migration in plume-ridge systems, *Earth and Planetary Science Letters*, 213, 417-430, 2003.

C. D. Byers, et al., Volatiles in Basaltic Glasses from the East Pacific Rise at 21-Degrees-N - Implications for Morb Sources and Submarine Lava Flow Morphology, *Earth and Planetary Science Letters*, 79, 9-20, 1986.

M. Bystricky, et al., High shear strain of olivine aggregates: Rheological and seismic consequences, *Science*, 290, 1564-1567, 2000.

F. Cammarano, et al., Inferring upper-mantle temperatures from seismic velocities, *Physics of the Earth and Planetary Interiors*, 138, 197-222, 2003.

V. E. Camp and M. E. Ross, Mantle dynamics and genesis of mafic magmatism in the intermontane Pacific Northwest, *Journal of Geophysical Research-Solid Earth*, 109, 2004.

R. L. Christiansen, et al., Upper-mantle origin of the Yellowstone hotspot, *Geological Society of America Bulletin*, 114, 1245-1256, 2002.

R. L. Christiansen and E. H. McKee, Late Cenozoic volcanic and tectonic evolution of the Great Basin and the Columbia intermontane regions, in *Cenozoic tectonics and regional geophysics of the western Cordillera*, edited by R. B. Smith and G. P. Eaton, pp. 283-311, Geological Society of America Memoir, Boulder, Colorado, 1978.

R. L. Christiansen and R. S. Yeats, Post-Laramide geology of the U.S. Cordilleran region, in *The Cordilleran Orogen: Conterminous U.S.*, edited by B. C. Burchfiel, et al., pp. 261-406, Geological Society of America, Boulder, Colorado, 1992.

J. Crosswhite and E. Humphreys, Origins of the Yellowstone hotspot and implications to western U.S. tectonics, *EOS, Trans. Am. geophys. Un., Fall meet. Suppl.*, 85, Abstract S13B-1046, 2004.

C. A. Currie, et al., Shear wave anisotropy beneath the Cascadia subduction zone and western North American craton, *Geophysical Journal International*, 157, 341-353, 2004.

F. A. Darbyshire, et al., Structure of the crust and uppermost mantle of Iceland from a combined seismic and gravity study, *Earth and Planetary Science Letters*, 181, 409-428, 2000.

A. Davaille, et al., Imaging isotherms in viscous convecting fluids, submitted.

J. H. Davies and D. J. Stevenson, Physical Model of Source Region of Subduction Zone Volcanics, *Journal of Geophysical Research-Solid Earth*, 97, 2037-2070, 1992.

M. M. Deal and G. Nolet, Slab temperature and thickness from seismic tomography 2. Izu-Bonin, Japan, and Kuril subduction zones, *Journal of Geophysical Research-Solid Earth*, *104*, 28803-28812, 1999.

M. M. Deal, et al., Slab temperature and thickness from seismic tomography 1. Method and application to Tonga, *Journal of Geophysical Research-Solid Earth*, *104*, 28789-28802, 1999.

D. J. DePaolo and M. Manga, Deep origin of hotspots - The mantle plume model, *Science*, *300*, 920-921, 2003.

W. R. Dickinson and W. S. Snyder, Geometry of Triple Junctions Related to San Andreas Transform, *Journal of Geophysical Research*, *84*, 561-572, 1979.

A. Dodson, et al., Helium and neon isotopes in the Imnaha Basalt, Columbia River Basalt Group: Evidence for a Yellowstone plume source, *Earth and Planetary Science Letters*, *150*, 443-451, 1997.

D. S. Draper, Late Cenozoic Bimodal Magmatism in the Northern Basin and Range Province of Southeastern Oregon, *Journal of Volcanology and Geothermal Research*, *47*, 299-328, 1991.

M. Ducea, The California arc: Thick granitic batholiths, eclogitic residues, lithospheric-scale thrusting, and magmatic flare-ups, *GSA Today*, *11*, 4-10, 2001.

K. Dueker, et al., Thick-structured Proterozoic lithosphere of the Rocky Mountain region, *GSA Today*, *11*, 4-9, 2001.

K. G. Dueker and E. D. Humphreys, Teleseismic imaging of the western United States upper mantle structure using the Simultaneous Iterative Reconstruction Technique, in

Seismic Tomography: Theory and Practice, edited by H. M. Iyer and K. Hirahara, pp. 265-298, Blackwell, London, 1993.

W. G. Ernst, Metamorphic Terranes, Isotopic Provinces, and Implications for Crustal Growth of the Western United-States, *Journal of Geophysical Research-Solid Earth and Planets*, *93*, 7634-7642, 1988.

R. A. Fabritius, Shear-wave anisotropy across the Cascade subduction zone from a linear seismograph array, M.S. thesis, Oregon State University, Corvallis, Oregon, 1995.

N. Favier and S. Chevrot, Sensitivity kernels for shear wave splitting in transverse isotropic media, *Geophysical Journal International*, *153*, 213-228, 2003.

D. Fee and K. Dueker, Mantle transition zone topography and structure beneath the Yellowstone hotspot, *Geophysical Research Letters*, *31*, 2004.

E. R. Flueh, et al., New seismic images of the Cascadia subduction zone from cruise SO108-ORWELL, *Tectonophysics*, *293*, 69-84, 1998.

D. W. Forsyth, et al., Phase velocities of Rayleigh waves in the MELT experiment on the East Pacific Rise, *Science*, *280*, 1235-1238, 1998.

G. R. Foulger and J. H. Natland, Is "hotspot" volcanism a consequence of plate tectonics?, *Science*, *300*, 921-922, 2003.

G. R. Foulger, et al., Seismic tomography shows that upwelling beneath Iceland is confined to the upper mantle, *Geophysical Journal International*, *146*, 504-530, 2001.

J. B. Gaherty and T. H. Jordan, Lehmann Discontinuity as the Base of an Anisotropic Layer beneath Continents, *Science*, *268*, 1468-1471, 1995.

D. Geist and M. Richards, Origin of the Columbia Plateau and Snake River Plain - Deflection of the Yellowstone Plume, *Geology*, 21, 789-792, 1993.

S. Goes, et al., Shallow mantle temperatures under Europe from P and S wave tomography, *Journal of Geophysical Research-Solid Earth*, 105, 11153-11169, 2000.

S. P. Grand, Mantle shear-wave tomography and the fate of subducted slabs, *Philosophical Transactions of the Royal Society of London Series a-Mathematical Physical and Engineering Sciences*, 360, 2475-2491, 2002.

A. E. Gripp and R. G. Gordon, Current Plate Velocities Relative to the Hotspots Incorporating the Nuvel-1 Global Plate Motion Model, *Geophysical Research Letters*, 17, 1109-1112, 1990.

A. E. Gripp and R. G. Gordon, Young tracks of hotspots and current plate velocities, *Geophysical Journal International*, 150, 321-361, 2002.

T. C. Hales, et al., A lithospheric instability origin for Columbia River flood basalts and Wallowa Mountains uplift in northeast Oregon, *Nature*, 438, 842-845, 2005.

R. Hall and W. Spakman, Subducted slabs beneath the eastern Indonesia-Tonga region: insights from tomography, *Earth and Planetary Science Letters*, 201, 321-336, 2002.

D. R. Harden, *California Geology*, 479 pp., Prentice Hall, 1998.

R. A. Harris, et al., Imaging the Juan Defuca Plate beneath Southern Oregon Using Teleseismic P-Wave Residuals, *Journal of Geophysical Research-Solid Earth*, 96, 19879-19889, 1991.

R. I. Hill, et al., Mantle Plumes and Continental Tectonics, *Science*, 256, 186-193, 1992.

B. K. Holtzman, et al., Melt segregation and strain partitioning: Implications for seismic anisotropy and mantle flow, *Science*, *301*, 1227-1230, 2003.

E. Humphreys, et al., A Tomographic Image of Mantle Structure beneath Southern-California, *Geophysical Research Letters*, *11*, 625-627, 1984.

E. D. Humphreys and K. G. Dueker, Physical State of the Western United-States Upper-Mantle, *Journal of Geophysical Research-Solid Earth*, *99*, 9635-9650, 1994a.

E. D. Humphreys and K. G. Dueker, Western United-States Upper-Mantle Structure, *Journal of Geophysical Research-Solid Earth*, *99*, 9615-9634, 1994b.

E. D. Humphreys, et al., Beneath Yellowstone: Evaluating Plume and Nonplume Models Using Teleseismic Images of the Upper Mantle, *GSA Today*, *10*, 1-7, 2000.

E. D. Humphreys and B. H. Hager, A Kinematic Model for the Late Cenozoic Development of Southern California Crust and Upper Mantle, *Journal of Geophysical Research-Solid Earth and Planets*, *95*, 19747-19762, 1990.

Y. Ida, Preferred Orientation of Olivine and Anisotropy of the Oceanic Lithosphere, *Journal of Physics of the Earth*, *32*, 245-257, 1984.

G. Ito, Reykjanes 'V'-shaped ridges originating from a pulsing and dehydrating mantle plume, *Nature*, *411*, 681-684, 2001.

G. Ito, et al., Dynamics of mantle flow and melting at a ridge-centered hotspot: Iceland and the Mid-Atlantic Ridge, *Earth and Planetary Science Letters*, *144*, 53-74, 1996.

G. Ito, et al., Observational and theoretical studies of the dynamics of mantle plume-mid-ocean ridge interaction, *Reviews of Geophysics*, *41*, 2003.

G. Ito, et al., Mantle flow, melting, and dehydration of the Iceland mantle plume, *Earth and Planetary Science Letters*, 165, 81-96, 1999.

S. M. Jones, et al., V-shaped ridges around Iceland: Implications for spatial and temporal patterns of mantle convection, *Geochemistry Geophysics Geosystems*, 3, 1059, doi:10.1029/2002GC000361, 2002.

B. T. Jordan, Age-progressive volcanism of the Oregon High Lava Plains: Overview and evaluation of tectonic models, in *Plates, Plumes, and Paradigms*, edited by G. R. Foulger, et al., pp. 503-515, Geological Society of America Special Paper, 2005.

B. T. Jordan, et al., Geochronology of age-progressive volcanism of the Oregon High Lava Plains: Implications for the plume interpretation of Yellowstone, *Journal of Geophysical Research*, 109, doi:10.1029/2003JB002776, 2004.

H. Jung and S. Karato, Water-induced fabric transitions in olivine, *Science*, 293, 1460-1463, 2001.

E. Kaminski, The influence of water on the development of lattice preferred orientation in olivine aggregates, *Geophysical Research Letters*, 29, 10.1029/2002GL014710, 2002.

S. Karato, On the Lehmann Discontinuity, *Geophysical Research Letters*, 19, 2255-2258, 1992.

C. Kincaid, et al., Laboratory Investigation of the Interaction of Off-Axis Mantle Plumes and Spreading Centers, *Nature*, 376, 758-761, 1995.

C. Kincaid, et al., The dynamics of off-axis plume-ridge interaction in the uppermost mantle, *Earth and Planetary Science Letters*, 137, 29-43, 1996.

R. H. Kingsley and J. G. Schilling, Plume-ridge interaction in the Easter Salas y Gomez seamount chain Easter Microplate system: Pb isotope evidence, *Journal of Geophysical Research-Solid Earth*, 103, 24159-24177, 1998.

R. D. Lawrence, Strike-Slip Faulting Terminates Basin and Range Province in Oregon, *Geological Society of America Bulletin*, 87, 846-850, 1976.

J. J. Leveque, et al., On the Use of the Checkerboard Test to Assess the Resolution of Tomographic Inversions, *Geophysical Journal International*, 115, 313-318, 1993.

A. B. Li and R. S. Detrick, Azimuthal anisotropy and phase velocity beneath Iceland: implication for plume-ridge interaction, *Earth and Planetary Science Letters*, 214, 153-165, 2003.

A. R. Lowry and R. B. Smith, Strength and Rheology of the Western Us Cordillera, *Journal of Geophysical Research-Solid Earth*, 100, 17947-17963, 1995.

J. Maclennan, et al., Plume-driven upwelling under central Iceland, *Earth and Planetary Science Letters*, 194, 67-82, 2001.

N. S. Macleod, et al., Geothermal significance of eastward increase in age of upper Cenozoic rhyolitic domes, in *Second United Nations Symposium on the Development and use of Geothermal Resources*, edited, pp. 465-474, U.S. Government Printing Office, Washington D.C., 1976.

D. Mainprice and P. G. Silver, Interpretation of Sks-Waves Using Samples from the Subcontinental Lithosphere, *Physics of the Earth and Planetary Interiors*, 78, 257-280, 1993.

F. Marone and B. Romanowicz, Non-linear crustal corrections in high-resolution regional waveform seismic tomography, *Geophysical Journal International*, 170, 460-467, 2007.

P. A. McCrory, et al., Depth to the Juan De Fuca Slab Beneath the Cascadia Subduction Margin—A 3-D Model for Sorting Earthquakes, *U.S. Geological Survey, Data Series 91, Version 1.2.*, 2006.

D. McKenzie, Constraints on melt generation and transport from U-series activity ratios, *Chemical Geology*, 162, 81-94, 2000.

C. Megnin and B. Romanowicz, The three-dimensional shear velocity structure of the mantle from the inversion of body, surface and higher-mode waveforms, *Geophysical Journal International*, 143, 709-728, 2000.

W. Menke, et al., Seismic Anisotropy in the Crust at the Mid-Atlantic Plate Boundary in South-West Iceland, *Geophysical Journal International*, 119, 783-790, 1994.

J.-C. C. Mercier, Magnitude of the Continental Lithospheric Stresses Inferred From Rheomorphic Petrology, *Journal of Geophysical Research*, 85, 6293-6303, 1980.

N. Metrich, et al., The 1783 Lakagigar Eruption in Iceland - Geochemistry, Co₂ and Sulfur Degassing, *Contributions to Mineralogy and Petrology*, 107, 435-447, 1991.

C. A. Michaelson and C. S. Weaver, Upper Mantle Structure from Teleseismic P-Wave Arrivals in Washington and Northern Oregon, *Journal of Geophysical Research-Solid Earth and Planets*, 91, 2077-2094, 1986.

R. Montelli, et al., Finite-frequency tomography reveals a variety of plumes in the mantle, *Science*, 303, 338-343, 2004.

A. R. L. Nichols, et al., Is the Iceland hot spot also wet? Evidence from the water contents of undegassed submarine and subglacial pillow basalts, *Earth and Planetary Science Letters*, 202, 77-87, 2002.

H. Nicholson and D. Latin, Olivine Tholeiites from Krafla, Iceland - Evidence for Variations in Melt Fraction within a Plume, *Journal of Petrology*, 33, 1105-1124, 1992.

A. Nicolas, et al., Mechanisms of Flow in Naturally and Experimentally Deformed Peridotites, *American Journal of Science*, 273, 853-876, 1973.

D. M. Parks and S. Ahzi, Polycrystalline Plastic-Deformation and Texture Evolution for Crystals Lacking 5 Independent Slip Systems, *Journal of the Mechanics and Physics of Solids*, 38, 701-724, 1990.

T. Parsons, et al., Mantle Plume Influence on the Neogene Uplift and Extension of the United-States Western Cordillera, *Geology*, 22, 83-86, 1994.

X. H. Peng and E. D. Humphreys, Crustal velocity structure across the eastern Snake River Plain and the Yellowstone swell, *Journal of Geophysical Research-Solid Earth*, 103, 7171-7186, 1998.

S. K. Pezzopane and R. J. Weldon, Tectonic Role of Active Faulting in Central Oregon, *Tectonics*, 12, 1140-1169, 1993.

K. L. Pierce, et al., *Yellowstone plume head: Postulated tectonic relations to the Vancouver slab, continental boundaries and climate*, 39 pp., 2000.

K. L. Pierce and W. J. Morgan, The track of the Yellowstone hotspot: Volcanism, faulting, and uplift, in *Regional geology of eastern Idaho and western Wyoming*, edited by P. K. Link, et al., pp. 1-53, Geological Society of America Memoir, 1992.

S. Pilidou, et al., Rayleigh wave tomography in the North Atlantic: high resolution images of the Iceland, Azores and Eifel mantle plumes, *Lithos*, 79, 453-474, 2005.

F. F. Pollitz, Seismic surface waves and mantle structure imaged by the Transportable Array, *Nature*, submitted.

R. Poreda, et al., Helium and Hydrogen Isotopes in Ocean-Ridge Basalts North and South of Iceland, *Earth and Planetary Science Letters*, 78, 1-17, 1986.

J. Rasmussen and E. Humphreys, Tomographic Image of the Juan-Defuca-Plate beneath Washington and Western Oregon Using Teleseismic P-Wave Travel-Times, *Geophysical Research Letters*, 15, 1417-1420, 1988.

N. M. Ribe and Y. Yu, A Theory for Plastic-Deformation and Textural Evolution of Olivine Polycrystals, *Journal of Geophysical Research-Solid Earth and Planets*, 96, 8325-8335, 1991.

J. Ritsema and R. M. Allen, The elusive mantle plume, *Earth and Planetary Science Letters*, 207, 1-12, 2003.

S. Rocchi, et al., Intraplate strike-slip tectonics as an alternative to mantle plume activity, in *Intraplate Strike-slip Deformation Belts*, edited by F. Salvini, Geological Society of London, London, United Kingdom, 2003.

G. Rumpker and P. G. Silver, Apparent shear-wave splitting parameters in the presence of vertically varying anisotropy, *Geophysical Journal International*, 135, 790-800, 1998.

R. L. Saltzer, et al., How are vertical shear wave splitting measurements affected by variations in the orientation of azimuthal anisotropy with depth?, *Geophysical Journal International*, 141, 374-390, 2000.

M. K. Savage, Seismic anisotropy and mantle deformation: What have we learned from shear wave splitting?, *Reviews of Geophysics*, 37, 65-106, 1999.

M. K. Savage, Seismic anisotropy and mantle deformation in the western United States and southwestern Canada, *International Geology Review*, 44, 913-937, 2002.

M. K. Savage and A. F. Sheehan, Seismic anisotropy and mantle flow from the Great Basin to the Great Plains, western United States, *Journal of Geophysical Research-Solid Earth*, 105, 13715-13734, 2000.

J.-G. Schilling, Iceland Mantle Plume: Geochemical Study of Reykjanes Ridge, *Nature*, 242, 565-571, 1973.

J. G. Schilling, Upper Mantle Heterogeneities and Dynamics, *Nature*, 314, 62-67, 1985.

J. G. Schilling, et al., Dispersion of the Jan Mayen and Iceland mantle plumes in the Arctic: A He-Pb-Nd-Sr isotope tracer study of basalts from the Kolbeinsey, Mohns, and Knipovich Ridges, *Journal of Geophysical Research-Solid Earth*, 104, 10543-10569, 1999.

J. G. Schilling, et al., Petrologic and Geochemical Variations Along the Mid-Atlantic Ridge from 29-Degrees-N to 73-Degrees-N, *American Journal of Science*, 283, 510-586, 1983.

D. Schutt, et al., Anisotropy of the Yellowstone hot spot wake, eastern Snake River Plain, Idaho, *Pure and Applied Geophysics*, 151, 443-462, 1998.

D. L. Schutt and E. D. Humphreys, Evidence for a deep asthenosphere beneath North America from western united states SKS splits, *Geology*, 29, 291-294, 2001.

R. C. Searle, et al., The Reykjanes Ridge: structure and tectonics of a hot-spot-influenced, slow-spreading ridge, from multibeam bathymetry, gravity and magnetic investigations, *Earth and Planetary Science Letters*, 160, 463-478, 1998.

J. Severinghaus and T. Atwater, Cenozoic geometry and thermal state of the subducting slabs beneath western North America, in *Basin and Range extensional tectonics near the latitude of Las Vegas, Nevada*, edited by B. P. Wernicke, Boulder, Colorado, 1990.

D. R. Shelly, et al., High-resolution subduction zone seismicity and velocity structure beneath Ibaraki Prefecture, Japan, *Journal of Geophysical Research-Solid Earth*, 111, 2006.

P. G. Silver, Seismic anisotropy beneath the continents: Probing the depths of geology, *Annual Review of Earth and Planetary Sciences*, 24, 385-432, 1996.

P. G. Silver and W. W. Chan, Implications for Continental Structure and Evolution from Seismic Anisotropy, *Nature*, 335, 34-39, 1988.

P. G. Silver and W. W. Chan, Shear-Wave Splitting and Subcontinental Mantle Deformation, *Journal of Geophysical Research-Solid Earth*, 96, 16429-16454, 1991.

P. G. Silver and W. E. Holt, The mantle flow field beneath western North America, *Science*, 295, 1054-1057, 2002.

P. G. Silver and M. K. Savage, The Interpretation of Shear-Wave Splitting Parameters in the Presence of 2 Anisotropic Layers, *Geophysical Journal International*, 119, 949-963, 1994.

L. Slater, et al., Melt generation and movement beneath Theistareykir, NE Iceland, *Journal of Petrology*, 42, 321-354, 2001.

C. Small, Observations of Ridge-Hotspot Interactions in the Southern-Ocean, *Journal of Geophysical Research-Solid Earth*, 100, 17931-17946, 1995.

R. B. Smith, Intraplate Tectonics Of Western North-American Plate, *Tectonophysics*, 37, 323-336, 1977.

R. B. Smith and L. W. Braile, The Yellowstone Hotspot, *Journal of Volcanology and Geothermal Research*, 61, 121-187, 1994.

R. K. Staples, et al., Faroe-Iceland Ridge Experiment .1. Crustal structure of northeastern Iceland, *Journal of Geophysical Research-Solid Earth*, 102, 7849-7866, 1997.

R. Stefansson, et al., Earthquake Prediction Research in the South Iceland Seismic Zone and the Sil Project, *Bulletin of the Seismological Society of America*, 83, 696-716, 1993.

J. H. Stewart, Basin-range structure in western North America: a review, in *Cenozoic tectonics and regional geophysics of the western Cordillera*, edited by R. B. Smith and G. P. Eaton, pp. 1-31, Geological Society of America Memoir, Boulder, Colorado, 1978.

E. Takahashi, et al., Origin of the Columbia River basalts: melting model of a heterogeneous plume head, *Earth and Planetary Science Letters*, 162, 63-80, 1998.

M. Talwani, et al., Rekjanes Ridge Crest: A Detailed Geophysical Study, *Journal of Geophysical Research*, 76, 473-517, 1971.

R. N. Taylor, et al., Isotopic constraints on the influence of the Icelandic plume, *Earth and Planetary Science Letters*, 148, E1-E8, 1997.

A. M. Trehu, et al., A Seismic-Reflection Profile across the Cascadia Subduction Zone Offshore Central Oregon - New Constraints on Methane Distribution and Crustal Structure, *Journal of Geophysical Research-Solid Earth*, 100, 15101-15116, 1995.

S. van der Lee and G. Nolet, Upper mantle S velocity structure of North America, *Journal of Geophysical Research-Solid Earth*, 102, 22815-22838, 1997.

J. C. Vandecar and R. S. Crosson, Determination of Teleseismic Relative Phase Arrival Times Using Multi-Channel Cross-Correlation and Least-Squares, *Bulletin of the Seismological Society of America*, 80, 150-169, 1990.

S. vanderLee and G. Nolet, Seismic image of the subducted trailing fragments of the Farallon plate, *Nature*, 386, 266-269, 1997.

P. Vogt, Asthenosphere motion recorded by the ocean floor south of Iceland, *Earth and Planetary Science Letters*, 13, 153-160, 1971.

P. R. Vogt, Plume, subaxial pipe flow, and topography along the mid-ocean ridges, *Earth and Planetary Science Letters*, 29, 309-325, 1976.

G. P. Waite, et al., Models of lithosphere and asthenosphere anisotropic structure of the Yellowstone hot spot from shear wave splitting, *Journal of Geophysical Research-Solid Earth*, 110, 2005.

G. P. Waite, et al., V-P and V-S structure of the Yellowstone hot spot from teleseismic tomography: Evidence for an upper mantle plume, *Journal of Geophysical Research-Solid Earth*, 111, 2006.

K. T. Walker, et al., Shear-wave splitting beneath the Snake River Plain suggests a mantle upwelling beneath eastern Nevada, USA, *Earth And Planetary Science Letters*, 222, 529-542, 2004.

N. D. Watkins and A. K. Baksi, Magnetostratigraphy and Oroclinal Folding of Columbia-River, Steens, and Owyhee Basalts in Oregon, Washington, and Idaho, *American Journal of Science*, 274, 148-189, 1974.

H. R. Wenk, et al., Modeling Plastic-Deformation of Peridotite with the Self-Consistent Theory, *Journal of Geophysical Research-Solid Earth and Planets*, 96, 8337-8349, 1991.

N. White and B. Lovell, Measuring the pulse of a plume with the sedimentary record, *Nature*, 387, 888-891, 1997.

R. S. White, et al., The Temperature of the Iceland Plume and Origin of Outward-Propagating V-Shaped Ridges, *Journal of the Geological Society*, 152, 1039-1045, 1995.

R. S. White and D. McKenzie, Mantle Plumes and Flood Basalts, *Journal of Geophysical Research-Solid Earth*, 100, 17543-17585, 1995.

D. S. Wilson, Tectonic History of the Juan-De-Fuca-Ridge over the Last 40 Million Years, *Journal of Geophysical Research-Solid Earth and Planets*, 93, 11863-11876, 1988.

C. J. Wolfe, et al., Seismic structure of the Iceland mantle plume, *Nature*, 385, 245-247, 1997.

C. J. Wolfe and P. G. Silver, Seismic anisotropy of oceanic upper mantle: Shear wave splitting methodologies and observations, *Journal of Geophysical Research-Solid Earth*, 103, 2791-2791, 1998.

C. J. Wolfe and S. C. Solomon, Shear-wave splitting and implications for mantle flow beneath the MELT region of the East Pacific Rise, *Science*, 280, 1230-1232, 1998.

M. Xue and R. M. Allen, Asthenospheric channeling of the Icelandic upwelling: Evidence from seismic anisotropy, *Earth and Planetary Science Letters*, 235, 167-182, 2005.

M. Xue and R. M. Allen, Origin of the Newberry Hotspot Track: Evidence from shear-wave splitting, *Earth and Planetary Science Letters*, 244, 315-322, 2006.

M. Xue and R. M. Allen, The Fate of the Juan de Fuca Plate: Implications for a Yellowstone Plume Head, *Earth Planet. Sci. Lett.*, 264, 266-276, 2007.

M. M. Yale and J. P. Morgan, Asthenosphere flow model of hotspot-ridge interactions: A comparison of Iceland and Kerguelen, *Earth and Planetary Science Letters*, 161, 45-56, 1998.

Y. Yang and M. H. Ritzwoller, Teleseismic surface wave tomography in the western US using the Transportable Array Component of USArray, *Geophysical Research Letters*, submitted.

H. Y. Yuan and K. Dueker, Teleseismic P-wave tomogram of the Yellowstone plume, *Geophysical Research Letters*, 32, 2005.

S. Q. Zhang and S. Karato, Lattice Preferred Orientation of Olivine Aggregates Deformed in Simple Shear, *Nature*, 375, 774-777, 1995.

D. P. Zhao, et al., Tomographic Imaging of the Alaska Subduction Zone, *Journal of Geophysical Research-Solid Earth*, 100, 6487-6504, 1995.

D. P. Zhao, et al., Depth extent of the Lau back-arc spreading center and its relation to subduction processes, *Science*, 278, 254-257, 1997.